Universität Stuttgart

Institut für Wasser- und Umweltsystemmodellierung

Mitteilungen

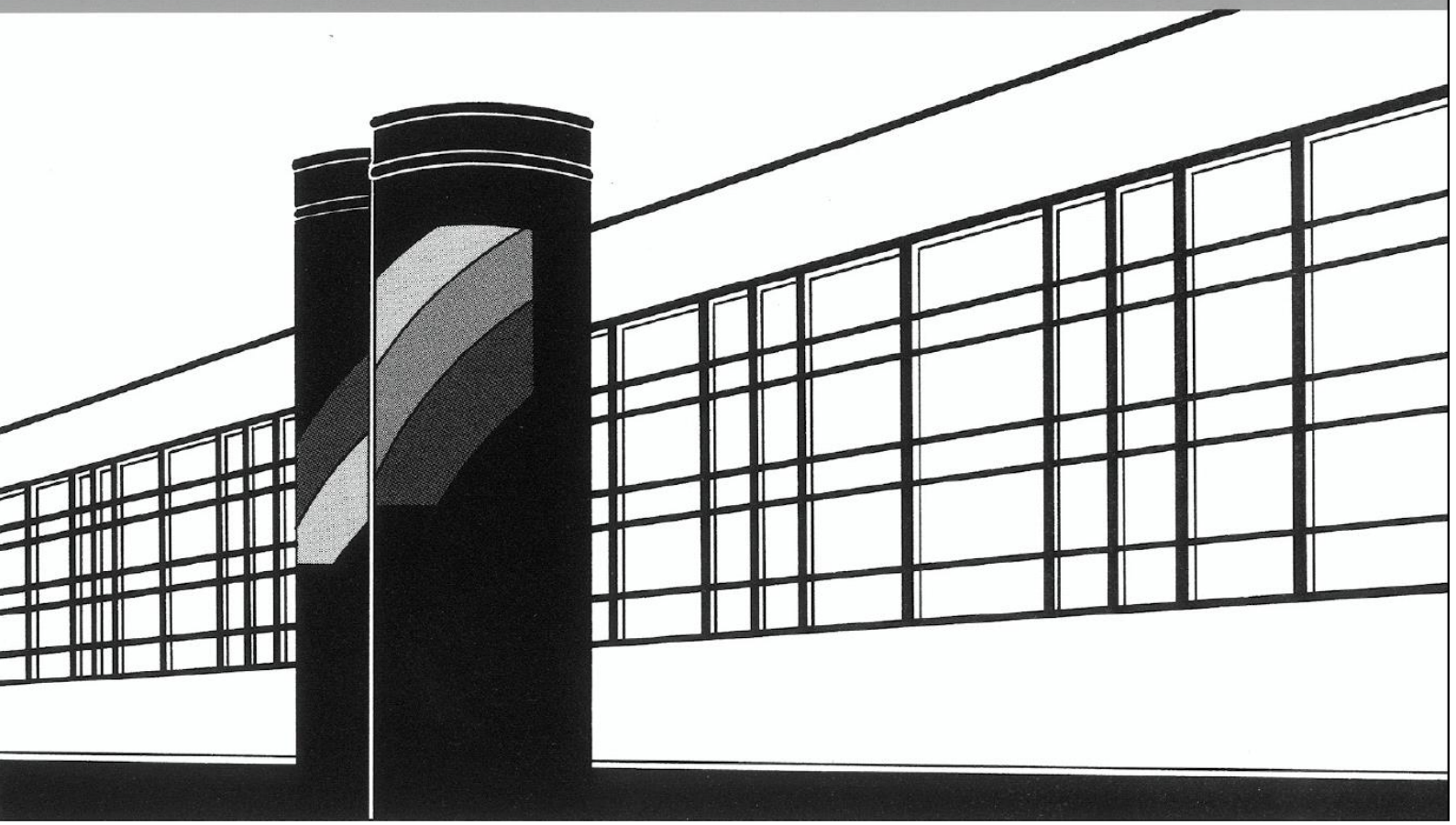

Heft 303 Maziar Veyskarami

Coupled free-flow–porous media flow processes including drop formation

Coupled free-flow–porous media flow processes including drop formation

Von der Fakultät Bau- und Umweltingenieurwissenschaften
der Universität Stuttgart und dem Stuttgart Center for Simulation Science
zur Erlangung der Würde eines
Doktor-Ingenieurs (Dr.-Ing.) genehmigte Abhandlung

vorgelegt von
Maziar Veyskarami
aus Khorram Abad, Iran

Hauptberichter:	Prof. Dr.-Ing. Rainer Helmig
Mitberichter:	Assoc. Prof. Dr. Carina Bringedal
	Prof. Dr.-Ing. Maurizio Santini

Tag der mündlichen Prüfung: 12. Juli 2023

Institut für Wasser- und Umweltsystemmodellierung
der Universität Stuttgart
2023

Heft 303

Coupled free-flow–porous media flow processes including drop formation

von
Dr.-Ing.
Maziar Veyskarami

Eigenverlag des Instituts für Wasser- und Umweltsystemmodellierung
der Universität Stuttgart

D93 Coupled free-flow–porous media flow processes including drop formation

Bibliografische Information der Deutschen Nationalbibliothek
Die Deutsche Nationalbibliothek verzeichnet diese Publikation in der Deutschen Nationalbibliografie; detaillierte bibliografische Daten sind im Internet über http://www.d-nb.de abrufbar

Veyskarami, Maziar:
Coupled free-flow–porous media flow processes including drop formation, Universität Stuttgart. - Stuttgart: Institut für Wasser- und Umweltsystemmodellierung, 2023

(Mitteilungen Institut für Wasser- und Umweltsystemmodellierung, Universität Stuttgart: H. 303)
Zugl.: Stuttgart, Univ., Diss., 2023
ISBN 978-3-910293-07-6
NE: Institut für Wasser- und Umweltsystemmodellierung <Stuttgart>: Mitteilungen

Herausgegeben 2023 vom Eigenverlag des Instituts für Wasser- und Umweltsystem-modellierung

Druck: P+K Solutions GmbH & Co. KG, Stuttgart

Acknowledgments

Above all, I would like to thank my supervisor and friend, Rainer Helmig, who has always been generously offering his support in scientific and everyday life challenges. Rainer's expertise, constructive insights and encouragements have been invaluable in shaping the present work. Thank you, Rainer, for fostering such a warm atmosphere in LH^2, based on trust and respect.

I would like to extend my appreciations to Cynthia Micahlkowski and Carina Bringedal, who provided me with their valuable insights during our weekly droplet meetings.

I am deeply grateful to Stefanie Siegert and Beate Spinner for their support and their patience in dealing with my administrative issues. My appreciations also go to David Werner for his helps as the IT administrator. I would also like to thank my colleagues in LH^2 for creating a positive and collaborative environment. You have been always there, offering your help and open to discussion.

I would appreciate the financial support of the Deutsche Forschungsgemeinschaft (DFG) for this project within the framework of the International Research Training Group "Droplet Interaction Technologies (DROPIT)".

My thanks also go to DROPIT members, especially Prof. Bernhard Weigand, for making such a friendly and interactive team. I am grateful for the opportunity that I had to carry out my research as a member of this team.

I am profoundly indebted to my parents in Iran for their unwavering love and encouragements throughout my whole life. Lastly, my heartfelt thanks to my friend, my love, and my wife, Rana. Thank you for your unconditional love and support with your kind heart and beautiful spirit. Thank you for bearing with me throughout the tough times in my academic journey. Without having you by my side, meeting the life's challenges would never be possible for me.

Contents

List of Figures

List of Tables

Nomenclature

Selected Acronyms

REV	representative elementary volume

Greek Letters

α	fluid phase	
γ	interfacial tension	[N/m]
κ	component	
λ	Thermal conductivity	[W/(m · K)]
$\Gamma_{\text{drop}}^{\text{ff}}$	interface between droplet and free flow (droplet surface)	
$\Gamma_{\text{pore}}^{\text{drop}}$	interface between pore and droplet	
$\Gamma_{\text{pore}}^{\text{ff}}$	interface between a pore and free flow	
$\Gamma_{\text{pore}}^{\text{ff}}$	interface between pore and free flow	
Ω_{drop}	droplet domain	
Ω_{ff}	free-flow domain	
Ω_{pore}	pore (porous medium) domain	
μ	chemical potential	[J/mol]

μ	dynamic viscosity	$[\mathrm{Pa} \cdot \mathrm{s}]$
ρ	mass density	$[\mathrm{kg/m^3}]$
ρ_{mol}	molar density	$[\mathrm{mol/m^3}]$
$\boldsymbol{\tau}$	shear stress tensor	
θ	contact angle	$[^\circ]$

Roman Letters

$\Delta\theta^{\mathrm{max}}$	maximum contact angle hysteresis	$[^\circ]$
$\dot{e}^{\mathrm{ff}}_{\mathrm{drop}}$	energy flux between droplet and free flow	[J/s]
$\dot{e}^{\mathrm{drop}}_{\mathrm{pore}}$	energy flux between droplet and pore	[J/s]
$\dot{m}^{\mathrm{ff}}_{\mathrm{drop}}$	mass flux between droplet and free flow	[kg/s]
$\dot{m}^{\mathrm{pore}}_{\mathrm{drop}}$	mass flux between droplet and pore	[kg/s]
$\dot{m}_{\mathrm{evap}}$	evaporative mass flux	[kg/s]
$\boldsymbol{I}$	identity matrix	[-]
$\boldsymbol{F}_{\mathrm{adh}}$	adhesion force	[N]
$\boldsymbol{F}_{\mathrm{drag}}$	drag force	[N]
$\boldsymbol{F}_{\mathrm{drop}}$	droplet force	[N]
$\boldsymbol{f}_{\mathrm{evap}}$	evaporative flux vector	$[\mathrm{kg/(m^2 \cdot s)}]$
$\boldsymbol{F}_{\mathrm{ff}}$	free-flow force	[N]
$\boldsymbol{F}_{\mathrm{hyst}}$	hysteresis force	[N]
$\boldsymbol{F}_{\mathrm{lift}}$	lift force	[N]

$\boldsymbol{F}_{\text{pore}}$	pore force	[N]
$\boldsymbol{F}_{\text{w}}$	weight force	[N]
$\boldsymbol{F}_{p}$	pressure force	[N]
$\boldsymbol{F}_{\rho v^2}$	inertial force	[N]
$\boldsymbol{F}_{\tau_{\text{ff}}}$	shear force	[N]
$\boldsymbol{F}_{p_c}$	capillary force	[N]
$\boldsymbol{g}$	gravity vector	[m/s^2]
$\boldsymbol{j}^{\kappa}_{\text{diff, mol}}$	diffusive flux of component κ	[mol/s]
$\boldsymbol{n}$	unit normal vector	[-]
$\boldsymbol{v}$	velocity vector	[m/s]
A_{ij}	pore throat cross-sectional area	[m^2]
D	Diffusion coefficient	[m^2/s]
g_{ij}	pore throat conductance	[m^2/(Pa $\cdot$ s)]
H	Henry's constant	[Pa]
h	droplet height	[m]
h	specific enthalpy	[J/kg]
l_{ij}	pore throat length	[m]
M	molecular mass	[kg/mol]
m	mass	[kg]
p	pressure	[Pa]

p_g^κ	partial pressure of componet κ	[Pa]
p_{sat}^κ	saturation vapor pressure	[Pa]
p_c	capillary pressure	[Pa]
Q	volumetric flow rate	[m^3/s]
q	mass sink/source term	[kg/(m^3·s)]
q^κ	molar sink/source term	[mol/(m^3·s)]
q^e	energy sink/source term	[J/(m^3·s)]
R	dropelt radius of curvature	[m]
R	universal gas constant	[J/(mol · K)]
r_{CA}	dropelt contact radius	[m]
r_{ij}	pore throat radius	[m]
S_α	saturation of phase α	[-]
T	temperature	[K]
t	time	[s]
u	specific internal energy	[J/kg]
V_{drop}	droplet volume	[m^3]
V_i	pore body volume	[m^3]
X_α^κ	mass fraction of component κ in phase α	[-]
x_α^κ	mole fraction of component κ in phase α	[-]

Subscripts and Superscripts

g	gas phase
i	related to i-direction
i	related to pore body i
j	related to j-direction
j	related to pore body j
l	liquid phase
N	quantitny related to free-flow cell neighbouring to droplet–free-flow interface
s	solid phase
adv	advancing
ff	quantitiy related to free flow
int	quantitiy related to free-flow face at dropelt–free-flow interface
rec	receding

Abstract

Behavior of a coupled free-flow–porous medium system is determined by the interface between the two domains. Formation of droplets at the interface governs transport processes in the whole system by enormously affecting the exchange of mass, momentum, and energy between the free flow and the porous medium. A droplet that forms at the interface might grow or shrink due to the flow from the porous medium and evaporation from its surface into the free flow. It also might be detached from the interface by the free flow. An example of such phenomena in nature is formation of sweat droplets on the skin by perspiration and the resulted cooling effect through their evaporation into the surrounding air. Water management in fuel cells, cooling systems, and inkjet printing are just a few technical applications in which droplet formation at the interface between a free flow and a porous medium appears.

In this work, pore-network modeling is used to describe the fluid flow in porous medium. Using a pore-network model enables us to resolve the pore-scale phenomena in more detail and locate the droplet emerging at the interface precisely, which are crucial for developing the coupling concepts between the domains.

All the models developed in this work are implemented in DuMu^{x}, an open-source simulator for flow and transport in porous media.

Coupling concept for free flow and porous medium with droplets at the interface
We developed a coupling concept describing the exchange between a free flow and a porous medium including droplet impact at the interface by taking the droplet–porous medium and droplet–free-flow interactions into account.

Writing the mass, momentum, and energy balances at the droplet–porous medium and droplet–free-flow interfaces, we describe the interaction between the droplet and the flow domains. In our concept, at the droplet–porous medium interface, a droplet and

the connected pore exchange mass, while their pressure and temperature are equal. At the droplet–free-flow interface, droplet molecules could leave the droplet due to evaporation into the free flow, free-flow forces and capillary force act on the droplet surface and energy is exchanged between the droplet and the free flow.

We present an approach to describe the droplet impact on the free-flow field. In this approach, proper droplet related properties are assigned to the part of the free-flow domain occupied by the droplet. Using this approach enables us to describe the impact of multiple droplets at the interface into account, while treating the free flow as a single-phase gas flow.

Model for droplet dynamics (droplet formation, growth, and detachment) In this work, a droplet forms at the interface as a result of liquid phase breakthrough from the porous medium to the interface. We describe the growth and shrinkage of the droplet by computing the mass exchanged between the droplet and the connected pore and between the droplet and the free flow. A droplet might grow or shrink with a constant contact angle or a constant contact radius mode, depending on the droplet contact radius and the connected pore radius at the interface.

In our concept to predict the droplet detachment, we identify and compare the forces acting on the droplet as a whole, i.e., free-flow forces and triple contact line (adhesion) forces. While free-flow forces act on the droplet to detach it from the interface, the adhesion forces, acting on the triple contact line, work to keep the droplet at the interface.

Model for droplet evaporation We describe the droplet evaporation as a diffusion-driven process in which the vapor from the droplet surface diffuses into the surrounding free flow due to the concentration gradient. Having local thermodynamic equilibrium at the droplet surface and assuming the fluid phases are ideal solutions, we compute the vapor concentration at the droplet surface and the concentration gradient between the droplet surface and the surrounding free flow. In the developed concept, we obtain the total mass exchange between the droplet and the free flow by integrating the mass flux over the droplet surface.

Results for droplet dynamics We present an experimental verification for a droplet formation and growth at the interface. The experimental setup consists of a cylindrical block made of Polytetrafluoroethylene (hydrophobic material) with a pore drilled at its center. Water is injected to the pore inlet at the bottom and a droplet forms and grows at the surface of the block. We simulated the droplet formation and growth process and compared the results with the experimental data, which showed that our model is able to predict the droplet formation and growth accurately.

In a comparison with experimental data for droplet detachment, a good agreement between the predicted droplet detachment volume by our model and experiment has been shown. We also compare the detachment predictions made using our model and using ANSYS Fluent and analyze the impact of contact angle hysteresis and the influence of using different descriptions of triple contact line on droplet detachment.

How neighboring droplets at the interface influence detachment of the other droplet is analyzed and discussed. Our analysis revealed that presence of an upstream droplet might advance or delay the droplet detachment, depending on the free-flow velocity and the distance between the two droplets.

Results for droplet evaporation We compare the simulation results of the developed model for evaporation of a single droplet at the interface with experimental data. Then, we examine the impact of free-flow and porous medium properties on the droplet evaporation. It is shown that velocity and relative humidity in the free-flow domain and pore temperature in the porous medium play key roles in droplet evaporation process.

We analyze and discuss the impact of the droplet evaporation on the droplet detachment. Our analyses showed that when the evaporation rate is comparable to the fluid flow rate coming from the connected pore to the droplet, it causes a significant delay in the droplet detachment or even prevent the detachment completely.

Zusammenfassung

Das Verhalten eines gekoppelten Systems, das aus einer freien Strömung und einem porösen Medium besteht, wird durch die Grenzfläche zwischen den beiden Bereichen bestimmt. Die Bildung von Tropfen an der Grenzfläche beeinflusst den Austausch von Masse, Impuls und Energie zwischen der freien Strömung und dem porösen Medium erheblich und wirkt sich somit auf die Transportprozesse im gesamten System aus. Ein Tropfen, der sich an der Grenzfläche bildet, kann durch die Strömung aus dem porösen Medium und die Verdunstung an seiner Oberfläche wachsen oder schrumpfen bzw. von der Grenzfläche durch die freie Strömung abgelöst werden. Ein gutes Beispiel hierfür ist der natürliche Prozess der Schweißbildung, bei dem Tropfen auf der Haut zu einem Kühleffekt durch Verdunstung in die Umgebungsluft führen. Das Wassermanagement in Brennstoffzellen, Kühlsystemen und Tintenstrahldruck sind nur einige technische Anwendungen, bei denen das Phänomen der Tropfenbildung an der Grenzfläche zwischen einer freien Strömung und einem porösen Medium auftritt.

In dieser Arbeit wird die Fluidströmung in einem porösen Medium mittels des „Pore-Network Modelling“ untersucht. Die Anwendung dieses speziellen Modells ermöglicht-die Phänomene auf der Porenskala detaillierter aufzulösen und die an der Grenzfläche entstehenden Tropfen genauer zu lokalisieren. Dies ist für die Entwicklung von Kopplungskonzepten zwischen den beiden Bereichen von entscheidender Bedeutung.

Die Modelle, die der vorliegenden Arbeit zugrunde liegen, wurden in DuMu^{x}, einem innovativen und quelloffenen Simulationstool für Strömung und Transport in porösen Medien, integriert.

Kopplungskonzept für freie Strömung und poröses Medium mit Tropfen an der Grenzfläche Ein Kopplungskonzept wurde von uns entwickelt, das den Austausch zwischen einer freien Strömung und einem porösen Medium unter Berücksichtigung

von Tropfen an der Grenzfläche beschreibt. Dabei wurden die Wechselwirkungen sowohl zwischen dem Tropfen und dem porösen Medium als auch zwischen dem Tropfen und der freien Strömung untersucht.

Durch die Aufstellung von Massen-, Impuls- und Energiebilanzen an den Grenzflächen zwischen Tropfen und porösem Medium sowie zwischen Tropfen und freier Strömung charakterisieren wir die Interaktionen zwischen dem Tropfen und den jeweiligen Strömungsdomänen ausführlich. In unserem dargelegten Konzept erfolgt ein Massenaustausch zwischen einem Tropfen und der dazugehörigen Pore an der Schnittstelle zum porösen Medium, wobei Druck und Temperatur der beiden an der Grenzfläche gleich sind. An der Kontaktfläche zwischen dem Tropfen und der freien Strömung verlassen Moleküle des Fluids den Tropfen durch Verdunstung in der freien Strömung. Zugleich beeinflussen Kräfte der freien Strömung und Kapillarkräfte die Tropfenoberfläche und es kommt des Weiteren zum Energieaustausch zwischen Tropfen und der freier Strömung.

Ein Ansatz zur Beschreibung des Einflusses eines Tropfens auf das Gebiet der freien Strömung wird in dieser Arbeit vorgestellt. Hierzu werden dem vom Tropfen eingenommenen Teil innerhalb der freien Strömung charakteristische Eigenschaften des Tropfens zugeordnet. Durch diese Methodik können Effekte mehrerer Tropfen an der Grenzfläche berücksichtigt werden, während die freie Strömung konsequent als einphasige Gasströmung behandelt wird.

Modell für die Tropfendynamik (Tropfenbildung, -wachstum und -ablösung) In dieser Arbeit resultiert die Bildung eines Tropfens an der Grenzfläche infolge des Eindringens der flüssigen Phase vom porösen Medium in die freie Strömung. Das Wachstum oder Schrumpfen des Tropfens wird durch die Berechnung des Massenaustauschs, sowohl zwischen dem Tropfen und der ihm verbundenen Pore als auch zwischen dem Tropfen und der freien Strömung, beschrieben. Abhängig von dem Kontaktradius des Tropfens und dem Radius der damit verbundenen Pore an der Grenzfläche kann ein Tropfen entweder mit einem konstanten Kontaktwinkel oder einem konstanten Kontaktradius wachsen oder schrumpfen.

In unserem Konzept zur Vorhersage der Tropfenablösung identifizieren und vergleichen wir die Kräfte, die auf den Tropfen als Ganzes wirken, d. h. die Kräfte der freien Strömung und die Kräfte der dreifachen Kontaktlinie (Adhäsion). Während die Kräfte

der freien Strömung dazu tendieren, den Tropfen von der Grenzfläche abzulösen, wirken die Adhäsionskräfte an der Dreifach-Kontaktlinie diesen entgegen, um den Tropfen an der Grenzfläche zu halten.

Modell für die Tropfenverdunstung Die Verdunstung von Tropfen wird als ein diffusionsgetriebener Prozess beschrieben, bei dem aufgrundvon Konzentrationsgradienten der Wasserdampf von der Tropfenoberfläche in die umgebende freie Strömung diffundiert. Bei lokalem thermodynamischem Gleichgewicht an der Tropfenoberfläche und unter der Annahme, dass die flüssigen Phasen ideale Lösungen darstellen, wird die Dampfkonzentration an der Tropfenoberfläche, sowie der Konzentrationsgradient zwischen der Tropfenoberfläche und der umgebenden freien Strömung, berechnet. Im vorgestellten Konzept wird der gesamte Massenaustausch zwischen dem Tropfen und der freien Strömung durch Integration des Massenflusses über die Tropfenoberfläche ermittelt.

Ergebnisse für die Tropfendynamik Ein experimenteller Nachweis für die Bildung und das Wachstum eines Tropfens an der Grenzfläche wurde präsentiert. Der verwendete Versuchsaufbau umfasst einen zylindrischen Block aus Polytetrafluorethylen (einem hydrophoben Material), in dessen Zentrum eine Pore gebohrt wurde, durch diese von unten Wasser injiziert wird. Der Prozess der Tropfenbildung und des Tropfenwachstums wurde simuliert und die Ergebnisse mit den experimentellen Daten verglichen. Diese Daten zeigen, dass unser Modell in der Lage ist, die Tropfenbildung und das Wachstum präzise vorherzusagen.

Ein Vergleich unserer Modellprognosen mit experimentellen Daten zur Tropfenablösung zeigt eine gute Übereinstimmung zwischen dem von uns vorhergesagten Ablösevolumen des Tropfens und den experimentellen Ergebnissen. Zudem setzen wir die Ablösungsvorhersagen unseres Modells in Bezug zu denjenigen, die mit ANSYS Fluent berechnet wurden. In diesem Zusammenhang wird auch die Relevanz der Kontaktwinkelhysterese betrachtet, sowie der Einfluss unterschiedlicher Beschreibungen der Dreifachkontaktlinie auf die Tropfenablösung analysiert.

Es wird analysiert und diskutiert, wie benachbarte Tropfen an der Grenzfläche die Ablösung des jeweils anderen Tropfens beeinflussen. Unsere Analyse hat gezeigt, dass die Anwesenheit eines stromaufwärts gelegenen Tropfens die Tropfenablösung des weiter

stromabwärts gelegenen Tropfens beschleunigen oder verzögern kann. Dies hängt maßgeblich von der Geschwindigkeit des Fluids in der freien Strömung und dem Abstand zwischen den beiden Tropfen ab.

Ergebnisse für die Tropfenverdunstung Die Simulationsergebnisse für die Verdunstung eines einzelnen Tropfens an der Grenzfläche werden mit experimentellen Daten verglichen. Anschließend wird der Einfluss von Eigenschaften der freien Strömung und des porösen Mediums auf die Tropfenverdunstung untersucht. Es lässt sich feststellen, dass die Geschwindigkeit und die relative Luftfeuchtigkeit der freien Strömung sowie die Temperatur der Poren im porösen Medium eine entscheidende Rolle bei der Tropfenverdunstung einnehmen.

Die Auswirkungen der Tropfenverdunstung auf die Tropfenablösung werden analysiert und diskutiert. Es wurde festgestellt, dass die Verdunstungsrate, sofern sie mit der Rate der Fluidströmung aus der mit dem Tropfen verbundenen Pore vergleichbar ist, die Tropfenablösung erheblich verzögern oder sogar gänzlich verhindern kann.

1 Introduction

1.1 Motivation

In a coupled free-flow–porous medium system, the interface plays a crucial role. Phenomena occurring at the interface determine the interaction between the free flow and the porous medium. Formation of droplets at the interface of a coupled free-flow-porous medium system occurs in many natural processes (e.g., human perspiration, in which droplets form at the skin to control the body temperature) and technical applications (e.g., fuel cells, cooling systems, membrane emulsification and filtration, thermal insulation and air conditioning of buildings)[Zhu et al., 2007, Arai and Suidzu, 2013, Glass et al., 2001, Charcosset, 2009, Rashidi et al., 2018]. Figure 1.1 illustrates a few examples of systems in which droplets form at the free-flow–porous medium interface. Droplet formation at the interface influences the interactions between the free flow and the porous medium significantly, in particular, the exchange of mass, momentum, and energy between the two domains. When a droplet covers a part of the interface, the exchange between the two domains occurs through the droplet. Thus, at the part covered with a droplet, droplet–porous medium and droplet–free-flow interactions govern the coupling between the free flow and the porous medium. Droplet formation tends to increase the complexity of the system through turning a simple interface to a complex interface, which not only handles the exchange between the free flow and the porous medium, but also stores mass and energy.

Droplets at the interface might grow or shrink, depending on the rate of fluid flow into the droplet from the porous medium and the evaporation rate from the surface of the droplet to the free flow. They also might spread and merge with other droplets at the interface, or be detached by the free flow [Baber, 2014, Ackermann et al., 2021]. In

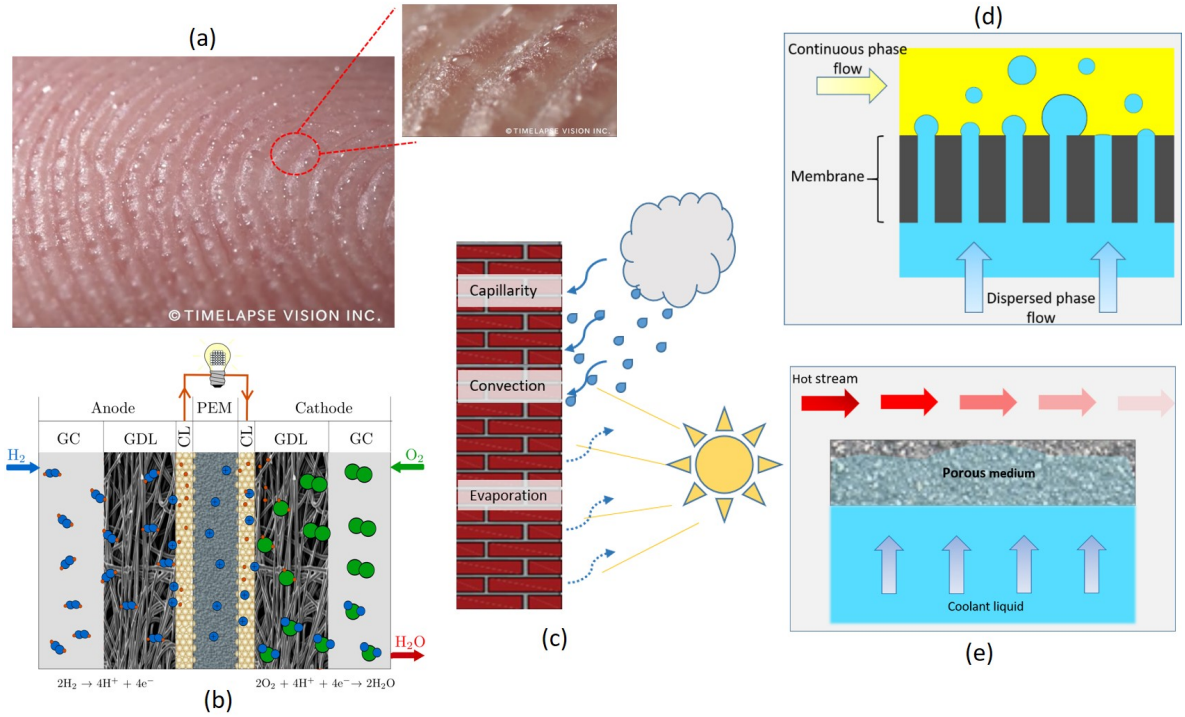

Figure 1.1: Examples of droplet formation at the interface between a free flow and a porous medium: a) perspiration on a fingertip (©TIMELAPSE VISION INC.)[TIMELAPSE VISION, 2017], b) water management in polymer electrolyte membrane fuel cells [Baber, 2014], c) thermal insulation and air conditioning of buildings, d) membrane emulsification, e) cooling systems.

modelling of a free-flow–porous medium system, taking the impacts of such phenomena occurring at the interface into account is of great importance.

1.2 State of the art

We review the previous findings in the research fields related to coupled free-flow–porous medium systems, droplet dynamics at the interface, and droplet evaporation.

Porous medium

Having a clear description of the porous medium is a crucial requirement in modeling of a coupled free-flow–porous medium system. In macro-scale modelling of the fluid flow

in a porous medium, the fluid and porous medium properties are defined by averaging the microscopic properties over a representative elementary volume (REV) and Darcy's law describes the fluid flow [e.g., Zhang et al., 2000].

Pore-scale models, on the other hand, provide more details of the transport phenomena occurring in a porous medium. These models, as their name implies, give an understanding of the fluid movement in a pore using a detailed description of the fluid configurations as well as fluid-fluid and fluid-solid interactions in the pore space [Blunt, 2017]. Direct numerical simulations, Lattice Boltzmann method and pore-network models are examples of methods, which can be used in pore-scale modelling. In comparison with other methods of modeling of pore-scale phenomena, pore-network models offer a low computational cost by eliminating the need for tracking the interfaces between the fluids and solid, while preserve a high level of accuracy [Joekar-Niasar and Hassanizadeh, 2011].

Coupled free-flow–porous medium systems without droplet impact

To investigate the systems of coupled free-flow–porous medium, two approaches have been developed: single-domain approach and two-domains approach [Jamet et al., 2009].

In the single-domain approach, it is assumed that one set of equations is sufficient to describe the entire domain, which consists of a free-flow and a porous medium. The Brinkman equation [Brinkman, 1949] is valid as the momentum balance equation in the whole domain. Assigning proper values to permeability and porosity, the free-flow domain and the porous medium can be distinguished and the transition between them is described by a thin transition zone or a lower-dimensional interface. Using the same set of equations in both subdomains eliminates the need for a special coupling concept at the interface [Jamet et al., 2009, Mosthaf et al., 2011].

However, difficulties in determining the thickness of the transition zone and choosing appropriate values for fluid and flow properties in this zone, as well as poor applicability of the Brinkman equation to porous media with low porosity, made using the single-domain approach quite challenging [Mosthaf et al., 2011].

The two-domain approach, as the name suggests, applies two different sets of equations to the flow domains. An interface separates the free flow and the porous medium and proper coupling conditions need to be developed to describe the interaction between the domains through the interface. Figure 1.2 shows single- and two-domain approach schematically.

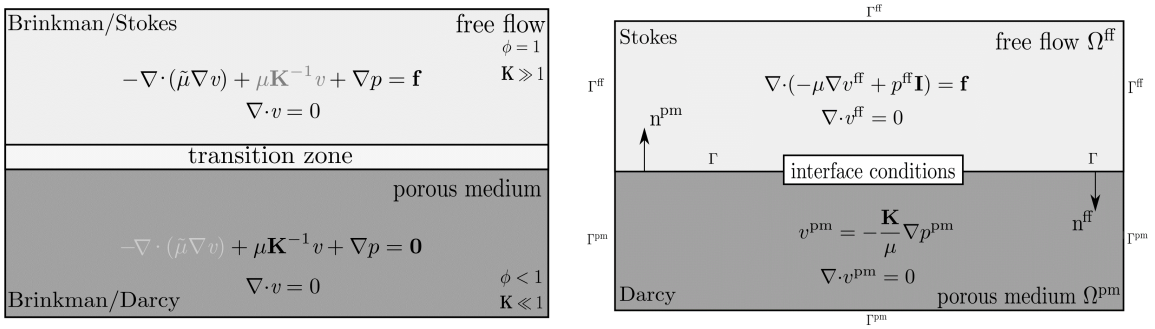

Figure 1.2: Coupling concepts: a) single-domain approach and b) two-domain approach [Mosthaf et al., 2011].

Mosthaf et al. [2011] proposed a coupling concept for a compositional system of single-phase free flow and two-phase porous medium on REV-scale. They used a two-domain approach, such that the Navier-Stokes equations and Darcy's law are employed to respectively describe fluid flow in the free-flow domain and the porous medium. The domains are coupled through a simple interface which transfers mass, energy, and momentum. The numerical implementation and performance of such a coupling concept for evaporation process from porous media is presented in Baber et al. [2012].

Due to the importance of pore-scale effects in porous media for interface-driven coupled systems, Weishaupt et al. [2019a] used pore-network modeling to describe the porous medium and the Navier-Stokes equations for the free-flow domain. They employed a fully monolithic coupling approach for the two subdomains and showed the high efficiency of the coupled model in terms of computational cost and accuracy in comparison with a reference case, which used Navier-Stokes equations to describe both subdomains in a direct numerical simulation. Figure 1.3 depicts a coupled free-flow–pore-network system used by Weishaupt et al. [2019a].

In Weishaupt et al. [2019b], the coupling conditions between the pore network and

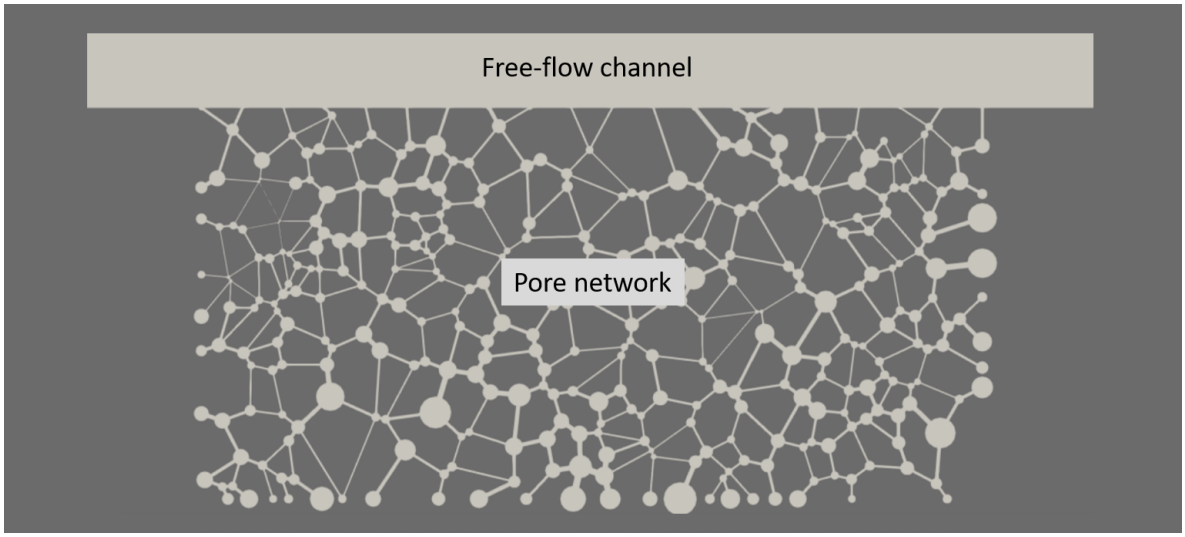

Figure 1.3: A schematic of a coupled free-flow–pore-network system [Weishaupt et al., 2019a].

the free flow are improved and a model reduction concept in the free-flow domain is developed.

Weishaupt [2020] also analyzed the impact of pore geometry and pore-network heterogeneity on the numerical behavior of a non-isothermal compositional coupled system, consisting of a single-phase free flow and a two-phase pore network, for modeling of evaporation from porous media.

To benefit from local accuracy of a pore-network model in modelling of large porous domains, a multi-scale approach could be employed. In such an approach, a porous medium could be divided into sub-domains according to the transport process intensity. Then, a pore-network model could be used to describe the parts of the porous medium, which have major impacts on the system (e.g., near-interface regions), coupled with the remaining parts of the porous medium modeled using an REV-scale approach [see e.g., Balhoff et al., 2007, Weishaupt, 2020].

Coupled free-flow–porous medium systems including droplet impact

To capture the impacts of droplet dynamics at the interface between a free flow and a porous medium on REV-scale, Baber et al. [2016] extended the coupling concept for a simple interface to include the mass and momentum of the droplet by developing a

REV-drop concept based on the concept presented by Mosthaf et al. [2011] and Baber et al. [2012].

Baber et al. [2016] used an area weighted averaging of the coupling conditions. In this approach, the free flow and the porous medium interact directly at the uncovered part, while the interaction between the two domains occurs through the droplet at the parts of the interface which are covered by droplets. They described the droplet dynamics in an averaged manner and did not resolve the droplet. The droplet volume is computed by introducing an additional degree of freedom at the interface using the mortar method. However, their concept requires prior knowledge about the number and location of the droplets forming at the interface and is not able to capture the impact of the droplets on the free flow.

Qin et al. [2012] investigated water flooding in gas channels of polymer electrolyte fuel cells by applying Darcy's law in the porous medium (i.e., gas diffusion layer) and the free-flow domain (i.e., gas channel). In their approach, it is assumed that the gas channel behaves as a porous medium with porosity of one, hence Darcy's law is applicable to describe the two-phase flow therein.

Ackermann et al. [2021] developed a three-domain approach which sees the interface as a lower-dimensional domain to include the droplet influence on a coupled free-flow-porous medium system. In this approach, the interface is physically a thin layer of the free-flow domain, which is in contact with the upper layer of the porous medium. The impacts of the droplet behavior are included in the interface description on the REV-scale. To account for film flow on the surface of the porous medium, they employed a similar approach as in Qin et al. [2012], which used Darcy's law in the free-flow channel. Accordingly, Ackermann et al. [2021] developed a liquid saturation–relative permeability relationship for the free-flow channel based on the amount of liquid in the channel. Although their approach can describe the droplet formation and growth in the interface domain, they use averaging to develop the coupling conditions between the domains. This approach can not capture the impact of the droplets on the free-flow field.

Using the volume of fluid method, Niblett et al. [2020] analyzed the impact of pore morphology in porous media on free-flow–porous media interactions and the performance of fuel cells. Their results stressed the importance of the interface conditions in optimization of fuel cell efficiency. They also found that the location of the droplets

forming on the surface of the porous medium plays a crucial role in water management process.

Michalkowski et al. [2022] investigated the droplet formation, growth, and detachment at the interface between the gas diffusion layer and the gas distributor channel in a polymer electrolyte membrane fuel cell. They used a dynamic pore-network model to describe the gas diffusion layer. They employed the developed model to describe the interactive behavior of multiple droplets forming at the interface. The results were compared with the so-called "bulging menisci model" introduce by Quesnel et al. [2015], which describes the interactive behavior of the droplets at the interface. The comparison showed the ability of their model to capture the multiple droplets interactions.

Droplet dynamics at the interface

Investigation of the droplet dynamics on a solid surface under the influence of a free flow has gained a lot of interests [Basu et al., 1997, Amara and Nasrallah, 2015, Chen et al., 2005, Kumbur et al., 2006, Xie et al., 2018]. A droplet at the interface could be deformed, slides/rolls or be detached due to the forces acting on the droplet by the surrounding free flow [Basu et al., 1997, Xie et al., 2018]. Various parameters affect the dynamics of droplets emerging at the interface of a coupled free-flow–porous medium system. The main effective parameters could be classified under three groups: fluid properties, domain properties and process properties. Interfacial tension between the gas and liquid phases and viscosity of the phases (fluid properties), pore morphology and wettability of the porous medium (domain properties), as well as free-flow velocity, temperature, and the rate of droplet growth (process properties) are only a few examples of parameters which influence the droplet dynamics at the interface [Charcosset, 2009].

The total free-flow force acting on a sessile droplet can be decomposed into two components: the lift force and the drag force. The lift force acts perpendicular to the overall flow direction, and the drag force acts in the overall flow direction [Basu et al., 1997].

A force that keeps the droplet attached to the surface against the external forces acts on the triple contact line. Decomposing this force, one component acts in the opposite direction of the free-flow drag force, which stems from the deformation of the droplet and distortion of the triple contact line [Antonini et al., 2009]. This force has been

referred to using different names in the literature, among them adhesion force, hysteresis force and retention force. Another force component acts perpendicular to the solid surface.

The competition between the free-flow forces and the triple contact line forces determines the onset of the droplet detachment. It has been shown that overcoming the hysteresis force by the free-flow drag force determines the instability of the triple contact line, followed by the droplet detachment [Basu et al., 1997].

Many attempts have been made to understand and describe the hysteresis force [Chen et al., 2005, Kumbur et al., 2006, Cho et al., 2012, Antonini et al., 2009]. The hysteresis force is a result of the interfacial tension acting on the triple contact line [Wang et al., 2020]. Having a clear description of the shape of the triple contact line and the contact angle distribution is of great importance in estimation of the hysteresis force.

Chen et al. [2005] developed a simplified model based on a two-dimensional notion to predict the onset of the droplet motion on a solid surface. The model was used to compute a droplet-instability diagram. Using a linear description of the contact angle distribution along the triple contact line, Kumbur et al. [2006] derived an equation to calculate the hysteresis force. Antonini et al. [2009] employed multiple profile images of a droplet under influence of an external force to reconstruct the triple contact line and contact angle distribution. They used the reconstructed contact line to evaluate the hysteresis force. Cho et al. [2012] developed a relation between the Weber number and the Reynolds number to predict the detachment of a droplet by a free flow.

To estimate the free-flow drag force, Kumbur et al. [2006] used a simplified approach by using a control volume around the droplet in a free-flow channel. They estimated the drag force by summing up the forces acting on this control volume due to the free-flow pressure along the channel and the shear force acting on the top of the control volume. Their approach was extended by Michalkowski et al. [2022] to include also the shear forces acting on the sides of the control volume.

Basu et al. [1997] introduced a model to predict the onset of the movement of a droplet on a solid surface. According to their analysis, a droplet on a super hydrophobic surface detaches by the free-flow drag force once the free-flow drag force overcomes the retention force. However, on a solid surface of less hydrophobicity, the droplet starts sliding on the surface at the onset of the droplet motion.

Hao and Cheng [2010] analyzed the dynamic contact angle of a droplet sliding on the wall of a channel driven by a shear flow. They conducted a force balance analysis and derived an analytical solution to predict the velocity of the droplet in terms of contact angle hysteresis.

Droplet evaporation at the interface

Various parameters affect the evaporation of droplets at the interface of a coupled free-flow–porous medium system. Droplet–free-flow interactions, droplet–pore interactions and droplet–solid surface interactions control the evaporation of a sessile droplet at the interface [Fuchs, 2013, Kulinich and Farzaneh, 2009, Song et al., 2011, Erbil, 2012, Picknett and Bexon, 1977]. The droplet–free-flow interactions occur through the droplet surface and affect, for instance, the diffusion of vapor from the surface of the droplet into the free flow [Fang et al., 2005]. The droplet–pore interactions determine energy and mass exchange between the droplet and the connected pore. The mode of droplet evaporation, triple contact line dynamics and contact angle changes are dependent on the droplet–solid surface interactions. In comparison with a droplet floating in a gas phase, the evaporation of a sessile droplet is slower due to the presence of the solid substrate, which hinders the evaporation [Picknett and Bexon, 1977].

Considering the evaporation of a spherical droplet as a stationary process, Maxwell [1890] characterized the evaporation as a diffusion-driven process. Due to variation of the droplet properties, e.g., droplet radius and temperature, referring to the droplet evaporation as a quasi-stationary process is more accurate [Fuchs, 2013]. Fang et al. [2005] described the droplet evaporation into free flow (air) as it consists of two parts: the diffusion part, which is diffusion of the vapor into the air and is controlled by the diffusion coefficient, and the evaporation part, which is flowing of the liquid molecules inside the droplet to the droplet surface and is regulated by the latent heat of vaporization.

Two pure modes of droplet evaporation on solid surfaces are distinguished: constant contact angle mode and constant contact radius mode [Picknett and Bexon, 1977]. The evaporation could occur following a combination of these two modes, depending on the surface properties and free-flow conditions [Bourges-Monnier and Shanahan, 1995]. Stick-slip motion of the evaporating droplet is observed on surfaces with low pinning

ability, whereas on those with high pinning ability, a high contact angle hysteresis is observed [Bormashenko et al., 2011]. It is also shown experimentally that on surfaces with more hydrophobicity, the contact line depins more easily during the evaporation [Orejon et al., 2011, Shin et al., 2009].

Kulinich and Farzaneh [2009] showed that the pinning ability of the surface determines the evaporation mode of a droplet on a super-hydrophobic surface. They observed that on a surface with a high pinning ability, i.e., high contact angle hysteresis of the droplet on the surface, the contact area of the droplet remains almost constant during the evaporation while the contact angle decreases constantly. However, a droplet on a surface with low pinning ability, i.e., low contact angle hysteresis of the droplet on the surface, follows mostly a constant contact angle and a decreasing contact area mode. According to their results, evaporation of a droplet on a surface with a high pinning ability occurs faster.

Sobac and Brutin [2011] carried out experiments to investigate the impact of surface properties on the evaporation of sessile droplets. They used nano- and micro-coatings to vary the surface roughness and wettability. They found that the impact of contact angle on the evaporation is more significant when the contact angle is greater.

Dash and Garimella [2013] investigated droplet evaporation on hydrophobic surfaces with small contact angle hysteresis. Comparing the experimental data with the diffusion-only model, Dash and Garimella [2013] found a good agreement between the results for a case of smooth hydrophobic surface. However, when a solid surface is superhydrophobic and shows a low contact angle hysteresis, the model overpredict the evaporation rate.

The impact of confinement on the droplet evaporation, i.e., droplet evaporation in a channel, is analyzed by Bansal et al. [2017]. In comparison with an unconfined droplet, their results show an increase in the total evaporation time of the droplet due to the accumulation of the water vapor in the channel.

Shaikeea and Basu [2016] analyzed the droplet evaporation in the presence of another evaporating droplet on a hydrophobic surface. They found that depending on the distance between the droplets, the evaporation rate of a pair of droplets could be less or equal to that of a single droplet. They also observed an asymmetric shrinkage of the droplets due to the evaporation as a result of the presence of the other droplet.

Interaction between multiple evaporating droplets is investigated by Hatte et al. [2019]. They analyzed the influence of the contact angle, the distance between the droplets, and the position of the droplets, i.e., if a droplet is between the other droplets or is a neighbor of just one droplet, on the evaporation process. They present a theoretical model to predict the evaporation of multiple droplets. According to their study, accumulation of vapor around the droplets leads to an asymmetric evaporation flux from the droplet surface and also increases the droplet evaporation time.

1.3 Contribution of the present work

The aim of the present work is to develop a model being able to describe multiple droplets at the interface of a coupled free-flow–porous medium system (see Fig. 1.4). In this work, we focus on the impact of droplet dynamics at the interface, such as formation, growth, and detachment of the droplet, as well as droplet evaporation, on the coupled system.

To do so, we develop new sets of coupling conditions describing mass, momentum, and energy transport at the interface based on the droplet–free-flow and droplet–porous medium interactions. Considering the huge impact of the phenomena occurring in the porous medium on the interface processes, the pore-network model is used to describe the fluid flow in the porous medium and take the pore-scale processes in more details into account.

We develop a concept to describe the droplet formation and growth at the interface due to the liquid breakthrough from the porous medium. In this concept, we include the droplet growth mode, i.e., constant contact angle and constant contact radius mode. For the sake of verification, we compare the results for formation and growth of a single droplet with experimental data. A concept is also developed to predict the onset of the detachment of a growing droplet from the interface due to the surrounding free flow. In this concept, we identify the forces in favor of the detachment, such as free-flow drag and lift forces, and forces against the detachment (i.e., forces acting on the triple contact line) to predict the droplet detachment. We compare the prediction results with experimental data and numerical results obtaining from other models to verify our developed concept. Then, we analyze the impacts of free-flow and porous medium

properties on the droplet detachment. In addition, We examine the impact of the neighboring droplet at the interface on the formation and growth of a droplet.

In the developed concept for the evaporation, we describe the droplet evaporation as a diffusion-driven process. We simulate evaporation of a sessile droplet in a channel and compare the simulation results with experimental data. We use the developed model to analyze how free-flow conditions (e.g., free-flow velocity and relative humidity), and porous medium conditions (e.g., contact angle and pore temperature) affect the droplet evaporation. We also investigate the influence of the droplet evaporation on the droplet growth and detachment.

We employ the developed model to simulate test cases composed of a free-flow channel coupled with a pore network, including formation of multiple droplets at the interface.

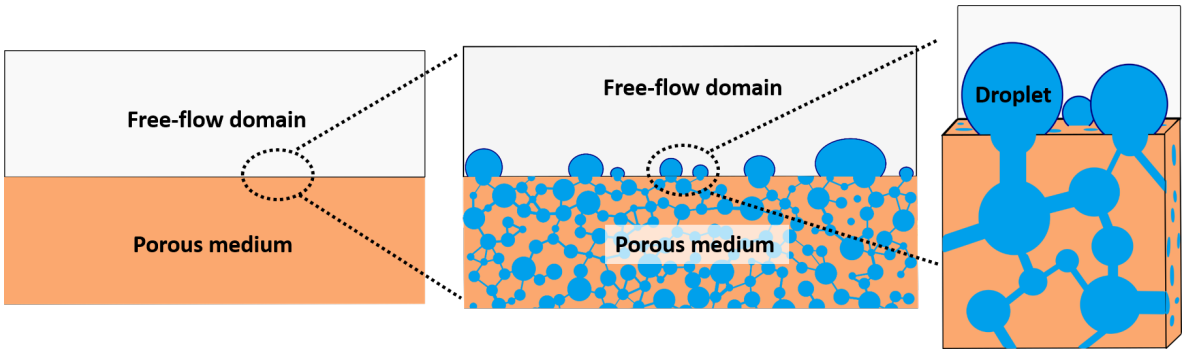

Figure 1.4: A coupled free-flow–porous medium (pore-network) system including droplets at the interface.

1.4 Outline

The structure of the thesis is as follows: in the next chapter (Chapter 2), we discuss some fundamental concepts. We explain the conceptual and numerical models used for the free-flow domain and the porous medium in Chapter 3. Then, we focus on the interface between a free-flow and a porous medium and introduce the coupling concepts for free-flow and porous medium with and without droplet in Chapter 4. In this chapter, we also present the conceptual and numerical models developed for droplet dynamics and droplet evaporation at the interface. After that, we present the results of

simulations using the developed models in Chapters 5 and 6. In Chapter 5, we conduct analysis and compare the simulation results for droplet dynamics with experimental data. Simulation results for droplet evaporation are presented in Chapter 6, where we also perform analysis and conduct a comparison with experimental data. We provide a summary in Chapter 7 and conclude with some perspectives for future developments.

2 Fundamentals

2.1 Fluid properties*

Scales Transport processes in a system of coupled free flow–porous medium can be considered on different scales. The intermolecular processes such as the movement and collisions of molecules are described in the *molecular scale*. Averaging over a volume yields *continuum scale*. On the continuum scale, parameters such as density and viscosity are defined and used to describe the fluid behavior. The Navier-Stokes equations describe the conservation of mass and momentum in the fluid transport on the continuum scale. The *pore scale* is defined by a detailed geometrical description of the solid and void space in the porous medium. Averaging of the porous medium properties over a sufficiently large volume, the representative elementary control volume (REV), gives quantities such as porosity and permeability, which describe the porous medium on the REV-scale.

Phases A phase α is a continuum in a certain physical state (solid, liquid or gaseous) with homogenous physical properties, which is characterized by its thermodynamic state variables such as pressure and temperature on the continuum scale. Sharp interfaces separate multiple phases, over which discontinuity of the physical properties occurs. Due to inherent miscibility of gases, only one gaseous phase can exist in a system, while more than one liquid and solid phases can be simultaneously present. The change in the phase density due to the pressure and temperature variations during a process determines whether a phase is incompressible or compressible. In this thesis, liquid and gaseous phases are the mobile phases, which we describe the former one

*Portions of this section were previously published by Transport in Porous Media (Springer) [Veyskarami et al., 2023].

as an incompressible fluid and the latter as a compressible fluid. The solid phase is assumed to be immobile and not deformable.

Components Each phase consists of one or more components. A component κ is composed of either pure chemical species (e.g., water) or a mixture of species (e.g, air), also called pseudo component. Components can be present in several phases in a system, and phases might exchange components in processes such as evaporation. Mass fraction X_α^κ or mole fraction x_α^κ is used to quantify each component κ in each phase α:

$$\begin{aligned} X_\alpha^\kappa &= \frac{m_\alpha^\kappa}{m_\alpha}\,, \\ x_\alpha^\kappa &= \frac{n_\alpha^\kappa}{n_\alpha}\,, \end{aligned} \tag{2.1}$$

where m stands for mass, and n shows the number of moles. The mole fraction of the component κ in the phase α can be converted to the mass fraction using the molecular mass of the component, M^κ and the averaged molecular mass of the phase, M_α, as follows:

$$X_\alpha^\kappa = \frac{x_\alpha^\kappa M^\kappa}{M_\alpha}\,. \tag{2.2}$$

The sum of mass/mole fractions within a phase is equal to one:

$$\sum_\kappa X_\alpha^\kappa = \sum_\kappa x_\alpha^\kappa = 1\,. \tag{2.3}$$

Density and viscosity The density, ρ, of a phase α is the mass per unit volume of the phase:

$$\rho_\alpha = \frac{m_\alpha}{V_\alpha}\,. \tag{2.4}$$

The molar density ρ_{mole} of a phase is defined as the number of moles per unit volume of that phase. The mass density and molar density can be converted to each other using the following relation:

$$\rho_\alpha = \rho_{\text{mole},\alpha} \sum_\kappa x_\alpha^\kappa M^\kappa\,. \tag{2.5}$$

The dynamic viscosity μ of a fluid phase defines the fluid resistance to flow and deformation. Both phase density and viscosity are functions of the phase pressure and

temperature.

Interfacial tension, contact angle and wettability In a system composed of two or more phases, an interface separates two immiscible fluids (e.g., liquid and gas) or a fluid and a solid. Formation of an interface between two phases is a result of the difference between the inter-molecular forces and the physical properties in the phases. As an example, if we have a water droplet surrounded by air, the net inter-molecular force acting on a water molecule due to its neighboring molecules is zero. Surrounded partially by other water molecules, a water molecule at the interface between the phases, however, experiences inter-molecular forces different from a water molecule inside the droplet. At the interface, the net inter-molecular force on the water molecule points inwards of the droplet. The combined effect of the radial components of inter-molecular forces across the entire interface surface is to make the surface contract, thereby increasing the pressure on the concave side of the surface. The difference between the inter-molecular forces of the phases can be reflected by surface or inter-facial tension, which is a universal property of the interface [Brutin, 2015]. The surface tension acts along the interface to minimize the free energy by decreasing the interface area between the phases. For instance, a similar strength of inter-molecular forces in adjacent phases results in a smaller interfacial tension between them. This might cause a weaker interface and ultimately partial or complete miscibility of the fluids.

In a system consisting of a sessile drop of liquid, l, on a solid surface, s, surrounded by a gas, g, three phases exist. The surface tension works between each pair of phases. In such a system, a three-phase contact line forms on which, in equilibrium state, a balance between the three surface tensions, γ, needs to be fulfilled. This is described by Young's equation [Young, 1832]:

$$\gamma_{lg} \cos\theta = \gamma_{gs} - \gamma_{ls} \,. \tag{2.6}$$

In the above equation, θ denotes the equilibrium (static) contact angle of the liquid phase with the solid surface. The contact angle indicates the degree of wettability between a fluid and a solid. Considering liquid water, a surface is called hydrophilic when $\theta < 90°$ and hydrophobic when $\theta > 90°$. Figure 2.1a illustrates a droplet on a hydrophobic surface in static condition and the surface tensions acting on the triple contact line.

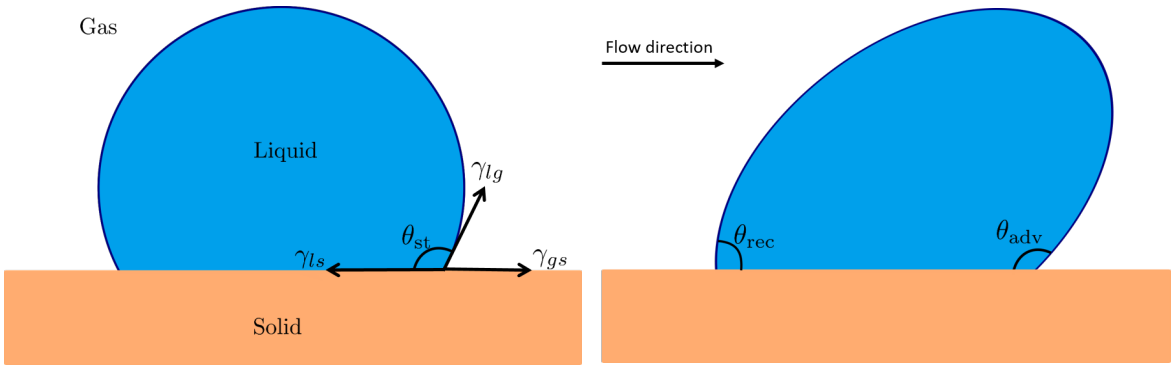

Figure 2.1: a) A static sessile droplet: the surface tensions acting on the three-phase contact line on a hydrophobic surface in equilibrium (static) condition and b) the advancing and receding contact angles of a sessile droplet surrounded by a fluid flowing from left to right.

The contact angle used in Eq. (2.6) is the equilibrium (static) contact angle. The equilibrium (static) contact angle is observed all along the triple contact line if the solid surface is homogeneous and no external forces act on the droplet. In real applications, however, various elements perturb the equilibrium assumption in the system, which leads to variation of the contact angle along the contact line. This variation is called hysteresis. The main origins of contact angle hysteresis are surface roughness, heterogeneity of the solid surface and chemical interaction between fluids and the solid surface. In a case where external forces are present, when contact angle hysteresis is very little (e.g., an ultra hydrophobic surface), the droplet starts moving easily [Li et al., 2007]. Having contact angle hysteresis, a droplet deforms before it starts moving due to the external forces.

Figure 2.1b shows advancing contact angle, θ_{adv}, and receding contact angle, θ_{rec}, which determine the contact angle hysteresis in a system. The maximum advancing contact angle is reached once the contact line is about to start moving in favor of the advancing of the contact area. On the other hand, the minimum receding contact angle is the contact angle right before the contact line moves toward the decreasing of the contact area. The ultimate contact angle hysteresis is the difference between the maximum advancing and minimum receding contact angles. For instance, a sessile droplet on a solid surface in a field of gas flow can experience several contact angles along its contact line, with values between the advancing contact angle and the receding contact angle.

Capillary pressure The capillary pressure p_c describes the pressure jump across the interface of two fluid phases due to the interfacial tension and the consequent curvature of the interface. The Young-Laplace equation describes such a relation as [e.g., Blunt, 2017]:

$$p_c = \gamma(\frac{1}{r_1} + \frac{1}{r_2})\,, \tag{2.7}$$

where r_1 and r_2 are the principal radii of curvature, which are equal for spherical geometries. Under equilibrium conditions, capillary pressure is the difference between the non-wetting phase pressure, p_n, and the wetting phase pressure, p_w [Hassanizadeh and Gray, 1993]:

$$p_c = p_n - p_w\,. \tag{2.8}$$

Partial pressure and saturation vapor pressure The partial pressure of a component κ, p_g^κ, which is also referred to as the vapor pressure, is the pressure that the vapor of κ would exert if it were the only component existed in the gaseous phase at a given temperature and volume.

The saturation vapor pressure of a component κ is the partial pressure of that component in the gaseous phase when it is in thermodynamic equilibrium with its pure liquid phase at a given temperature. Surface curvature of the liquid surface affects the saturation vapor pressure. Using Kelvin's law, the impact of liquid surface curvature can be taken into account [Thomson, 1872, Lamanna et al., 2020]. According to Kelvin's law, the saturation vapor pressure reduces on the concave surfaces and increases on the convex surfaces in comparison to a flat surface. Depending on the degree of surface curvature, such an impact might be important, e.g., in porous media or at a droplet surface. Equation (2.9) shows the correction made to the saturation vapor pressure for a convex surface, e.g., a droplet surface:

$$p^\kappa_{\mathrm{sat,Kelvin}} = p^\kappa_{\mathrm{sat},\infty} \exp\,(\frac{p_c M^\kappa}{\rho_l R T})\,, \tag{2.9}$$

where $p^\kappa_{\mathrm{sat},\infty}$ is the saturation vapor pressure on a flat liquid surface, which is a function of temperature. $p^\kappa_{\mathrm{sat,Kelvin}}$ refers to the modified saturation vapor pressure, which includes the impact of liquid surface curvature. M^κ is the molecular mass of the component κ, R is the universal gas constant, and T is the temperature. In Eq. (2.9), the capillary pressure, p_c, reflects the impact of surface curvature. In this work, we

always use Kelvin's law to include the surface curvature in saturation vapor pressure calculations.

Interface Dependent on the scale and application, the word "interface" might have different meanings. In this work, we distinguish between two kinds of interfaces: interfaces between the phases and interfaces between the domains. Fluid–fluid and fluid–solid interfaces are interfaces, which separate two different phases. The interface between a free-flow domain and a porous medium, however, separates two different flow domains.

2.2 Thermodynamic basics

2.2.1 Local thermodynamic equilibrium

In a system consists of several phases, local thermodynamic equilibrium between the phases is reached when mechanical, thermal, and chemical equilibrium hold locally and at the same time [Helmig et al., 1997, Cengel et al., 2011]. At the interface between the phases, mechanical equilibrium means that no net force acts on the interface. Thermal equilibrium describes a condition in which the temperature of the phases at the interface are equal. The chemical equilibrium implies that the chemical potential of each component at the interface is the same in different phases. Local thermodynamic equilibrium is assumed to be satisfied when the flow processes occur slowly and in a sufficiently large timescale.

2.2.2 Phase compositions and phase change

Assuming local thermodynamic equilibrium, the phase compositions can be obtained using the thermodynamic state variables.

Ideal solution (mixture) When dissimilar molecules in a solution have negligible impact on each other, the solution is said to be an ideal solution. In such a solution, the interactions between all molecules, whether from the same component or different components, are the same. Such behavior can be observed in ideal gases as well as in many diluted liquid solutions [Cengel et al., 2011]. In this work, we assume that both liquid and gaseous phases can be considered as ideal solutions.

Gas phase composition The relation between the density of an ideal gas ρ_g with its pressure p_g and temperature T_g can be described by the ideal gas law:

$$\rho_g = \frac{p_g M_g}{R T_g} \,, \tag{2.10}$$

where M_g and R are molecular mass and the universal gas constant, respectively. Dalton's law of additive pressures states that the total pressure of a gas mixture is equal to the sum of all component (partial) pressures:

$$p_g = \sum_{\kappa} p_g^{\kappa} \,. \tag{2.11}$$

For an ideal gas, the pressure fraction and the mole fraction of a component are equal:

$$x_g^{\kappa} = \frac{p_g^{\kappa}}{p_g} \,. \tag{2.12}$$

Liquid phase composition In ideal mixtures, the relation between the mole fraction of the main component on the liquid side, x_l^{κ}, and the partial pressure of the component on the gas side can be described using Raoult's law:

$$p_g^{\kappa} = x_l^{\kappa} p_{\text{sat}}^{\kappa} \,, \tag{2.13}$$

where p_{sat}^{κ} is the saturated vapor pressure. Substitution of Eq. (2.13) in Eq. (2.12) and rearrangement gives the following relation between the mole fractions of the main component of the liquid phase on the liquid and gas sides:

$$x_g^{\kappa} = x_l^{\kappa} \frac{p_{\text{sat}}^{\kappa}}{p_g} \,. \tag{2.14}$$

For a liquid solution with a small amount of dissolved gas, Henry's law describes the relation between the mole fraction of the solute in the liquid phase and its partial pressure in the gas phase:

$$x_l^\kappa = \frac{p_g^\kappa}{H}\,, \tag{2.15}$$

where H is the Henry's constant, which is a function of temperature only and independent of pressure [Cengel et al., 2011].

2.3 Pore-network modelling

Pore-network model A pore-network model is an approximate topological and geometrical representation of a porous medium, which describes the void space as a network composed of pore bodies connected with pore throats. Pore bodies represent the larger voids, which determine the porous medium capacity to store fluids, i.e., porosity. Pore throats are the narrower void spaces, which connect the pore bodies and control the fluid flow between them [Blunt, 2017]. Topology and geometry of a pore network are the main factors determining its behavior. Two pore networks with the same topology (backbone) show different behaviors if the geometries used in those networks to describe pore bodies and throats are different [Joekar-Niasar and Hassanizadeh, 2012, Vogel and Roth, 2001].

Coordination number The coordination number of a pore body specifies the number of pore throats connected to that pore body. The average coordination number of a network indicates the degree of the network connectivity. In fact, coordination number and the location of pore bodies characterize the network topology.

Idealized geometries for pore body and pore throat Idealized shapes are used to represent pore bodies and throats in a pore network model. To represent pore bodies, three-dimensional idealized objects, e.g., sphere and cube, are necessary. Choosing a proper object to describe the pore body is crucial, in particular, in two-phase flow modelling, where the description of pore body filling is of great importance [Joekar-Niasar and Hassanizadeh, 2012]. For a pore throat, however, a two-dimensional figure, e.g., circle, square and triangles, is required to describe the cross-section of the throat.

Using angular cross-sections enables the model to account for the corner flow of the wetting phase [Joekar-Niasar and Hassanizadeh, 2012].

Pore throat invasion and entry capillary pressure Considering a system of two pore bodies connected with a pore throat, which is initially filled with the wetting phase, increasing the saturation of the non-wetting phase in one of the two pore bodies leads to increase in the capillary pressure in that pore body. As long as the threshold capillary pressure of the pore throat is greater than the pore body capillary pressure, non-wetting phase can not enter the pore throat, i.e., single-phase flow of the wetting phase in the pore throat. Once the pore body capillary pressure overcomes the threshold capillary pressure of the pore throat, the non-wetting phase enters the pore throat, which is called pore throat invasion. In fact, pore throat invasion is a local drainage where the non-wetting phase fully/partly displaces the wetting phase in the pore throat. The threshold capillary pressure of the throat which determines the onset of the invasion process is the entry capillary pressure for invasion, $p_{c,e}$. the entry capillary pressure has an inverse relationship with the contact angle and the pore throat radius, while a direct relationship with the interfacial tension between the fluid phases. For instance, the entry capillary pressure of a circular pore throat ij can be computed by:

$$p_{c,e,ij} = \frac{2\gamma \cos(\theta_{\text{rec}})}{r_{ij}} \,. \tag{2.16}$$

Where r_{ij} is the pore throat radius. Since the non-wetting phase displaces the wetting phase during the pore throat invasion, the receding contact angle, θ_{rec}, measured in the wetting phase, is used to compute the entry capillary pressure. For a pore throat with a non-circular cross-section, after the non-wetting phase invasion, the wetting phase might still be present in the pore throat by forming wetting layers in the pore throat corners. That means, the fluid phase configuration changes from a cross-section full of wetting phase to having wetting layers in the corners and non-wetting phase in the middle due to the invasion. To derive a relation for capillary entry pressure in such pore throats, Mason and Morrow [1991] and Øren et al. [1998] took an approach based on the change in free energy during the invasion process. For more details, we refer to, e.g., Blunt [2017].

Pore throat snap-off and snap-off capillary pressure Opposite to the pore throat invasion, snap-off is a local imbibition process. Snap-off might occur only in pore throats with angular cross-sections, where wetting layers can be present in the corners. A prerequisite for the snap-off is connection between the wetting layers in the pore throat corners and the wetting phase in the connected pore bodies. A pore throat, which has already been invaded by the non-wetting phase, can experience swelling of the wetting layers in the corner due to rising of the wetting phase saturation in the connected pore body. By increasing the wetting phase saturation in the pore body, the wetting pressure in the pore body increases correspondingly, i.e., the pore body capillary pressure decreases. Further increase in the wetting phase saturation in the pore body and, consequently, swelling of the wetting layers in the pore throat leads to a point when the establishment of a three-phase contact line in the pore throat is not possible. At this point, the wetting phase fills the throat spontaneously, which is called snap-off. The snap-off capillary pressure of the pore throat is used as a criterion to predict the snap-off. Snap-off occurs when the pore body capillary pressure decreases below the snap-off capillary pressure. Equation (2.17) is used to calculate the snap-off capillary pressure [Blunt, 2017]:

$$p_{c,s,ij} = \frac{\gamma \cos(\theta_{\text{adv}})}{r_{ij}} (1 - \tan(\theta_{\text{adv}}) \tan(\beta_{ij})) \,, \tag{2.17}$$

where β_{ij} is the corner half-angle of the pore throat. As we mentioned before, snap-off does not occur in pore throats with circular cross-section.

3 Porous medium and free-flow domain: Conceptual and numerical models

3.1 Porous medium: pore-network model

In this section, we briefly discuss the balance equations in a pore-network model, which is used to describe the porous medium flow. A pore-network model approximates the porous medium as a network of pore bodies scattered in a solid bulk, connected by tubes known as pore throats. Figure 3.1 shows two pore bodies, i and j, connected to each other by pore throat ij. In this model, pore throats determine the conductivity behavior of the system and pore bodies are responsible for the storage capacity. In addition, the primary variables are located at the center of the pore body, where the balance equations need to be fulfilled [Blunt, 2017].

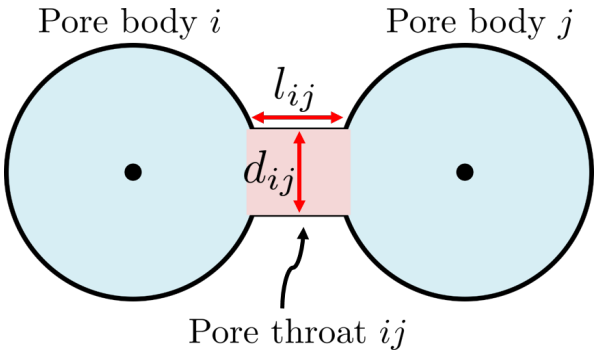

Figure 3.1: Pore bodies i and j are connected by pore throat ij [Veyskarami et al., 2023].

3.1.1 Single-phase flow in porous medium

Mass balance In a single-phase non-compositional flow, Eq. (3.1) describes the mass balance on each pore body, i.

$$V_i \frac{\partial(\rho_i)}{\partial t} + \sum_j (\rho Q)_{ij} = (Vq)_i \,. \tag{3.1}$$

In the above equation, the storage term is the first term on the left-hand side, in which V is the volume of the pore body and ρ indicates the density of the fluid. The second term is the advection term, which is the sum of the fluid flow into/out of the pore body in interaction with the connected neighboring pore bodies. Q is the volumetric fluid flow between each pore body, i, and its neighboring pore body, j. The density used to calculate this term comes from the upwind pore body. The term on the right-hand side refers to the possible source/sink in the pore body.

In a compositional flow, the mass balance equation for each component κ on each pore body i can be written as follows:

$$\begin{aligned} V_i \frac{\partial(x^\kappa \rho_{\text{mole}})_i}{\partial t} + \sum_j (x^\kappa \rho_{\text{mole}} Q)_{ij} \\ + \sum_j (\boldsymbol{j}^{\kappa,\text{pnm}}_{\text{diff, mole}} A)_{ij} = (V q^\kappa)_i \,. \end{aligned} \tag{3.2}$$

In the above equation, x is the mole fraction. The subscript "mole" indicates that the molar value is used in the calculations. The third term on the left-hand side of Eq. (3.2) accounts for the contribution of the diffusive mass transfer. A is the cross-sectional area of the pore throat and the diffusive flux, $\boldsymbol{j}^{\kappa,\text{pnm}}_{\text{diff, mole}}$, is described using the Fick's first law as:

$$\boldsymbol{j}^{\kappa,\text{pnm}}_{\text{diff, mole},ij} = -\frac{1}{M^\kappa} \rho D^\kappa \frac{X^\kappa_j - X^\kappa_i}{l_{ij}} \,, \tag{3.3}$$

where D is the binary diffusion coefficient, X is the mass fraction and l is the length of the pore throat connecting the two pore bodies. ρ and D^κ in Eq. (3.3) are computed

by averaging as:

$$\rho = \frac{\rho_j + \rho_i}{2}\,, \tag{3.4}$$

$$D^\kappa = \frac{2D_j^\kappa D_i^\kappa}{D_j^\kappa + D_i^\kappa}\,. \tag{3.5}$$

Momentum equation A pore-network model uses the well-known Hagen-Poiseuille equation as the basic principle to describe the one-dimensional flow in each pore throat of the network. The Hagen-Poiseuille equation can be derived from the Navier-Stokes equations by assuming a one-dimensional, fully developed, stationary laminar flow in a single pore throat [Weishaupt, 2020]. Neglecting the impact of gravity, the general equation to calculate the volumetric flow rate, Q_{ij}, into/out of pore body i through pore throat ij is:

$$Q_{ij} = -g_{ij}(p_j - p_i)\,, \tag{3.6}$$

where g is the conductance term and p is the pressure in each pore body. Depending on the pore throat cross-sectional area, there are different relationships for computing g [Weishaupt, 2020]. For example, when the pore throat has a circular cross-section, g can be obtained by the following equation:

$$g_{ij} = \frac{A_{ij} r_{ij}^2}{8\mu l_{ij}}\,, \tag{3.7}$$

where μ is the fluid viscosity, l is the pore throat length, and A and r are the pore throat cross-sectional area and the pore throat radius, respectively.

Energy balance Equation (3.8) shows the energy balance for each pore body, i, in a system consisting of more than one component.

$$\begin{aligned} &V_i \frac{\partial(\rho u)_i}{\partial t} + \sum_j (\rho h Q)_{ij} \\ &+ \sum_j (-\lambda \nabla T A)_{ij} + \sum_j \left[A \sum_\kappa (\boldsymbol{j}_{\mathrm{diff}}^{\kappa,\mathrm{pnm}} h^\kappa) \right]_{ij} = (V q^e)_i\,. \end{aligned} \tag{3.8}$$

From left to right, the first term is the storage term and u is the specific internal energy. The second term describes the convective energy transport and h is the specific

phase enthalpy, which is the weighted sum of specific enthalpy of each component, h^κ, as:

$$h = \sum_\kappa X^\kappa h^\kappa \,. \tag{3.9}$$

The conductive energy transport is described using the Fourier's law, as in the third term of Eq. (3.8), where λ is the heat conductivity and T is the phase temperature. λ is computed by averaging the heat conductivity of pore bodies i and j as:

$$\lambda = \frac{2\lambda_j \lambda_i}{\lambda_j + \lambda_i} \,. \tag{3.10}$$

The fourth term on the left-hand side of Eq. (3.8) takes the contribution of diffusive energy transport into account. The term on the right-hand side stands for any energy source/sink in the pore body.

3.1.2 Two-phase flow in porous medium

Mass balance In a two-phase non-compositional system, the mass balance of phase α on each pore body, i, is described by Eq. (3.11).

$$V_i \frac{\partial(\rho_\alpha S_\alpha)_i}{\partial t} + \sum_j (\rho_\alpha Q_\alpha)_{ij} = (V q_\alpha)_i \,. \tag{3.11}$$

In the above equation, S_α indicates the saturation of phase α.

In a two-phase compositional flow, Eq. (3.12) describes the mass balance equation for each component κ on each pore body i:

$$\begin{aligned} V_i \frac{\partial(\sum_\alpha x_\alpha^\kappa \rho_{\text{mole},\alpha} S_\alpha)_i}{\partial t} &+ \sum_\alpha \sum_j (x_\alpha^\kappa \rho_{\text{mole},\alpha} Q_\alpha)_{ij} \\ &+ \sum_\alpha \sum_j (\boldsymbol{j}^{\kappa,\text{pnm}}_{\text{diff, mole},\alpha} A_\alpha)_{ij} = (V q^\kappa_{\text{mole}})_i \,. \end{aligned} \tag{3.12}$$

The subscript "mole" indicates that the molar value of the parameter is used in the calculations. The Fick's first law describes the diffusive flux of component κ, $\boldsymbol{j}^{\kappa,\text{pnm}}_{\text{diff, mole}}$,

in each phase α, through each pore throat ij as:

$$\boldsymbol{j}^{\kappa,\mathrm{pnm}}_{\mathrm{diff,\ mole},\alpha,ij} = -\frac{1}{M^\kappa}\rho_\alpha D^\kappa_\alpha \frac{X^\kappa_{\alpha,j} - X^\kappa_{\alpha,i}}{l_{ij}}\,, \tag{3.13}$$

where ρ_α and D^κ_α in the above equation are averaged amounts for phase α and are computed as in Eqs. (3.4) and (3.5).

Momentum equation Neglecting the impact of gravity, the general equation to calculate the flow rate of phase α, $Q_{\alpha,ij}$, in pore throat ij connecting pore bodies i and j is:

$$Q_{\alpha,ij} = -g_{\alpha,ij}(p_{\alpha,j} - p_{\alpha,i})\,, \tag{3.14}$$

where g_α can be calculated as a function of the effective cross-sectional area and the effective radius related to the phase α in the throat. For more details about different approaches to calculate g_α, we refer to Weishaupt [2020].

Energy balance In a two-phase compositional system, the energy balance in each pore body, i, can be written as:

$$\begin{aligned} &V_i \frac{\partial(\sum_\alpha \rho_\alpha u_\alpha S_\alpha)_i}{\partial t} + \sum_\alpha \sum_j (\rho_\alpha h_\alpha Q_\alpha)_{ij} \\ &+ \sum_\alpha \sum_j (-\lambda_\alpha \nabla T A_\alpha)_{ij} + \sum_\alpha \sum_j \left[A_\alpha \sum_\kappa \left(\boldsymbol{j}^{\kappa,\mathrm{pnm}}_{\mathrm{diff},\alpha} h^\kappa_\alpha \right) \right]_{ij} = (V q^e)_i\,. \end{aligned} \tag{3.15}$$

Here, h_α is the specific phase enthalpy, which is obtained by:

$$h_\alpha = \sum_\kappa X^\kappa_\alpha h^\kappa_\alpha\,. \tag{3.16}$$

Further, λ_α is heat conductivity of phase α and computed by:

$$\lambda_\alpha = \frac{2\lambda_{\alpha,j}\lambda_{\alpha,i}}{\lambda_{\alpha,j} + \lambda_{\alpha,i}}\,. \tag{3.17}$$

Complementary relations Two more relations are required to close the system of equations in a two-phase system. The first relation guarantees that the sum of the

phase saturations in each pore body i is equal to one:

$$\sum_{\alpha} S_{\alpha,i} = 1\,. \tag{3.18}$$

Referring to the wetting phase by w and the non-wetting phase by n, Eq. (3.18) can be written as:

$$S_{w,i} + S_{n,i} = 1\,. \tag{3.19}$$

Another relation is the local capillary pressure–saturation relationship, which describes how the capillary pressure in a pore body i varies by the wetting phase saturation. Joekar-Niasar [2010] derived the following relation to describe the capillary pressure–saturation relationship in a cubic pore body:

$$p_{c,i} = \frac{2\gamma}{r_i(1 - \exp(-6.83 S_{w,i}))}\,. \tag{3.20}$$

In this equation, γ is the interfacial tension between the fluid phases and r is the inscribed pore body radius. Based on Joekar-Niasar [2010], Sweijen et al. [2018] proposed a general form of equation for capillary pressure–saturation relationship in pore bodies with platonic shapes:

$$p_{c,i} = \frac{2\gamma}{r_i(1 - \exp(c_i S_{w,i}))}\,, \tag{3.21}$$

where c is a geometrical constant determined by the shape of the pore body.

3.1.3 Numerical model

Primary variables In a single-phase non-compositional model, pressure is the primary variable which needs to be computed. In a compositional model, pressure and mole/mass fraction of the component other than the phase's major component are the primary variables.

In a two-phase non-compositional system, pressure of one phase and saturation of the other phase are primary variables. In a two-phase compositional system, dependent on the phase state in a pore body, each of two sets of primary variables might be used. If two phases are present in a pore body, the primary variables need to be used to describe that pore body are pressure of one phase and saturation of the other

phase. The mole/mass fraction of components can be computed by assuming chemical equilibrium in the pore body. However, if only one phase is present in a pore body, that pore body is described with a single-phase compositional set of primary variables, i.e., pressure and mole/mass fraction of the component other than the major component. In a case, where a pore body initially contains both phases and one of the phases vanishes during the process, e.g., due to evaporation, the set of primary variables needs to be changed such that they remain physically meaningful [Class et al., 2002]. For more details about the switch of primary variables due to the change in the phase state in a pore body, we refer to Weishaupt [2020].

If energy transport in the system needs to be taken into account, temperature is added to the set of primary variables. Table 3.1 summarizes the model types and the corresponding set of primary variables for single- and two-phase flow.

Table 3.1: Different types of model for single-phase flow and the corresponding set of primary variables. For two-phase two-component model, case A is when both phases are present in the pore body, case B is when only the wetting phase is present, and case C is when only the non-wetting phase is present.

model type		primary variables
Single-phase single-component (non-isothermal)	1p(ni)	p, (T)
Single-phase two-component (non-isothermal)	1pnc(ni)	p, x^{κ_2} (T)
Two-phase single-component (non-isothermal)	2p(ni)	p_w, S_n (T)
Two-phase two-component (non-isothermal)	2pnc(ni)	A: p_w, S_n (T) B: p_w, $x_n^{\kappa_2}$ (T) C: p_w, $x_w^{\kappa_2}$ (T)

Discretization In the pore-network model used in this work, the box method [Helmig et al., 1997, Huber and Helmig, 2000] is used for spatial discretization. This scheme is also called node centered finite volume method, i.e., a control volume (box) is associated to each grid node on which the balance equations are formulated. Each control volume is divided into sub-control volumes. Integration of fluxes over the faces makes the Box method locally mass conservative. In the context of pore-network modeling, the grid nodes correspond to the center of the pore bodies and each pore body is treated as a control volume (box). Thus, each pore body is divided to sub-control volumes according to its coordination number. The pore throats, which connect a pore body to other pore bodies, are treated as the faces between the control volumes on which the

fluxes are calculated. Accordingly, the balance equations are solved for each pore body. Figure 3.2 shows a configuration where the coordination number of pore bodies i and j are four and two, respectively. Thus, pore body i is divided into four and pore body j is divided into two sub-control volumes. The flux between the pore bodies i and j is calculated at the pore throat ij, which connects the two pore bodies.

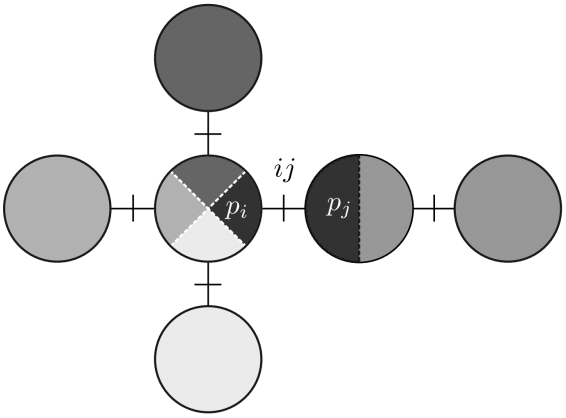

Figure 3.2: Application of the Box method for pore-network modeling. Each pore body is divided into sub-control volumes based on its coordination number. the primary variables, e.g., pressure, are located at the centers of pore bodies [Weishaupt, 2020].

3.2 Free-flow domain

In this work, the free flow is a single-phase gas flow, which consists of one or more components. Thus, we present the balance equations describing a single-phase free-flow domain in the following.

Mass balance The continuity equation, Eq. (3.22), is used to fulfill mass balance in the single-phase single-component free-flow domain,

$$\frac{\partial \rho}{\partial t} + \nabla \cdot (\rho \boldsymbol{v}) = q \,. \tag{3.22}$$

The following balance equation is solved for each component κ in a compositional flow.

$$\frac{\partial x^{\kappa} \rho_{\text{mole}}}{\partial t} + \nabla \cdot (x^{\kappa} \rho_{\text{mole}} \boldsymbol{v} + \boldsymbol{j}^{\kappa,\text{ff}}_{\text{diff, mole}}) = q^{\kappa}_{\text{mole}} \,. \tag{3.23}$$

In the above equations, x is the mole fraction, ρ is the fluid density, $\boldsymbol{v}$ is the velocity vector, q is the possible source or sink term and $\boldsymbol{j}^{\kappa,\mathrm{ff}}_{\mathrm{diff,\ mole}}$ is the diffusive flux. The subscript "mole" indicates that the molar value of the parameter is used in the calculations. The diffusive flux, $\boldsymbol{j}^{\kappa,\mathrm{ff}}_{\mathrm{diff,\ mole}}$, is approximated by Fick's first law for component κ as:

$$\boldsymbol{j}^{\kappa,\mathrm{ff}}_{\mathrm{diff,\ mole}} = -\frac{1}{M^{\kappa}}\rho D^{\kappa}\nabla X^{\kappa}\,, \tag{3.24}$$

where D is the binary diffusion coefficient and X is the mass fraction.

Momentum balance The Navier–Stokes equations describe the momentum balance in the free-flow domain,

$$\frac{\partial(\rho\boldsymbol{v})}{\partial t} + \nabla\cdot(\rho\boldsymbol{v}\otimes\boldsymbol{v}) + \nabla\cdot\left(p\boldsymbol{I} - \mu(\nabla\boldsymbol{v} + \nabla\boldsymbol{v}^{T})\right) - \rho\boldsymbol{g} = 0\,, \tag{3.25}$$

where p is the fluid pressure, μ is the fluid viscosity and $\boldsymbol{g}$ is the gravity vector.

Energy balance For a non-isothermal free flow, we use the following relation to describe the energy balance in the system:

$$\frac{\partial(\rho u)}{\partial t} + \nabla\cdot(h\rho\boldsymbol{v}) - \nabla\cdot(\lambda\nabla T) + \sum_{\kappa}\nabla\cdot\left(\boldsymbol{j}^{\kappa,\mathrm{ff}}_{\mathrm{diff}}h^{\kappa}\right) = q^{e}\,, \tag{3.26}$$

where h is the specific phase enthalpy, which in a compositional system can be computed as:

$$h = \sum_{\kappa} X^{\kappa}h^{\kappa}\,. \tag{3.27}$$

The contribution of diffusive energy transport in a compositional system is described by the fourth term of Eq. (3.26), $\sum_{\kappa}\nabla\cdot\left(\boldsymbol{j}^{\kappa,\mathrm{ff}}_{\mathrm{diff}}h^{\kappa}\right)$. In case of non-compositional flow, this term is zero. q^{e} is the possible energy sink or source term.

Numerical model We employ a staggered-grid finite volume approach to discretize the free-flow balance equations in space. In such an approach, the velocity degrees of freedom are located at the face of the primary cell, which is the center of the relevant secondary grid cell. The rest of the degrees of freedoms such as pressure, temperature

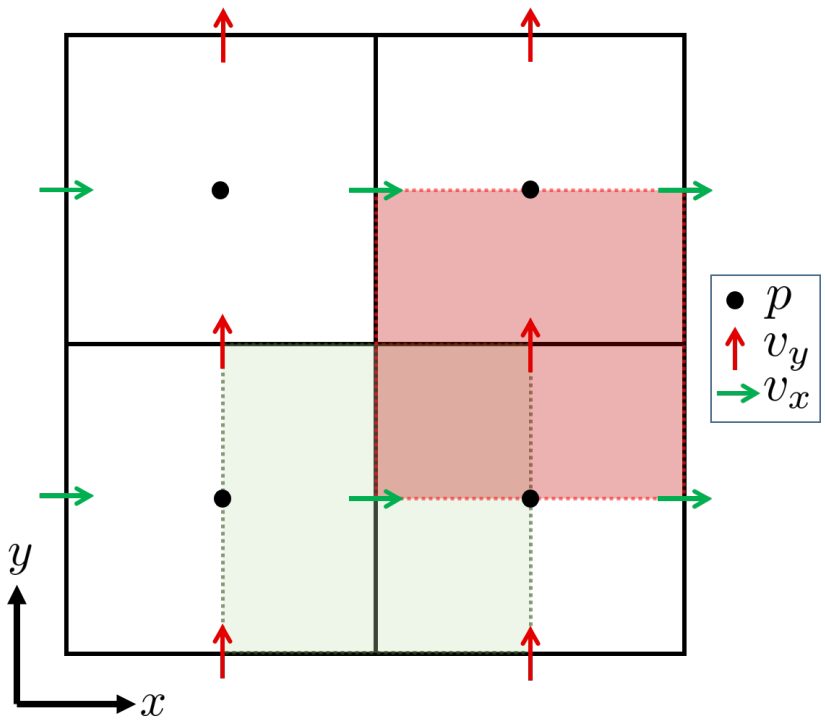

Figure 3.3: Staggered grid: the solid black lines are for the primary grid, the green dashed lines are for the secondary grids in x-direction and the red dashed lines are for the secondary grid in y-direction.

(in case of non-isothermal flow), and mole/mass fraction (in case of compositional flow) are located at the center of the primary grid cell (see Fig. 3.3). A detailed description on the staggered-grid finite volume approach is provided by, e.g., Schneider et al. [2020].

4 Interface between free flow and porous medium *

In this chapter, we discuss the interactions at the interface between a free flow and a porous medium. We derive coupling conditions for the exchange of mass, momentum, and energy between the domains with and without droplets. In addition, we discuss droplet dynamics at the interface and introduce modeling concepts to describe them. Furthermore, we present a concept to model the droplet evaporation.

4.1 Interface configurations

In a coupled system of a free flow and a porous medium without droplets, the two domains interact with each other directly through an interface. When droplets form at the interface, they cover a part of it and affect the interaction between the two flow domains. Consequently, two different sets of coupling conditions are required to describe the exchange of mass, momentum, and energy between the free flow and the porous medium with and without droplets. One set for the part of the interface which no droplet emerged, and another set for the covered part of the interface with droplets. Figure 4.1 illustrates a pore which is in direct contact with the free flow (left), and a droplet formed at the interface between a pore and the free flow (right). We need to distinguish between three interfaces: $\Gamma^{\mathrm{ff}}_{\mathrm{pore}}$ between a pore which is not covered by a droplet and the free flow, $\Gamma^{\mathrm{drop}}_{\mathrm{pore}}$ between the pore covered with a droplet and the droplet, and $\Gamma^{\mathrm{ff}}_{\mathrm{drop}}$ between the droplet formed at the interface and the free flow. These interfaces and their unit normal vectors are shown in Fig. 4.1. It is important to note

*Parts of this chapter were previously published by Transport in Porous Media (Springer) [Veyskarami et al., 2023]. Parts of this chapter have also been submitted for publication to Transport in Porous Media (Springer).

that since in the pore-network model used in this study, only pore bodies can be at the boundary, the interactions between the free flow and the porous medium occurs through the coupled pore bodies with the free flow at the interface. That means that $\Gamma^{\mathrm{ff}}_{\mathrm{pore}}$ describes an area at which a pore body meets the free-flow boundary. Similarly, $\Gamma^{\mathrm{pore}}_{\mathrm{drop}}$ is the interface between a droplet and the connected pore body.

Two scenarios might lead to droplet formation at the interface: the first one is when a droplet forms due to liquid breakthrough from the porous medium onto the interface, and the second scenario is settlement of floating droplets in the free flow at the interface. The focus of the present work is on the first scenario.

The models developed in this work are applicable to hydrophobic interfaces and porous media, and can be used for hydrophilic media with minor adjustments.

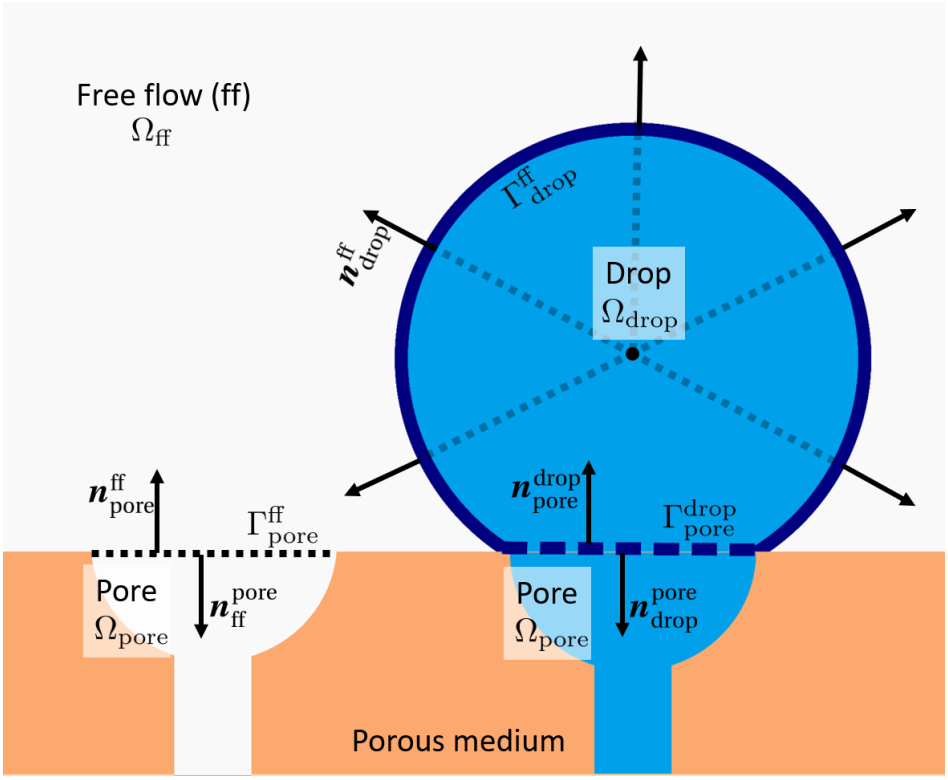

Figure 4.1: Interface configurations: in the absence of droplets (left), and with a droplet (right).

4.2 Interface without droplets

4.2.1 Coupling concept for free flow and porous medium without droplets

At the parts of the interface, where are not covered with droplets, the free flow and the porous medium interact with each other directly through $\Gamma^{\text{ff}}_{\text{pore}}$. This section discusses the coupling concept describing the mass, momentum, and energy interaction between a free flow and a porous medium without droplets.

Mass balance In a non-compositional system, at $\Gamma^{\text{ff}}_{\text{pore}}$, we have the continuity of the total mass flux:

$$[\rho \boldsymbol{v}]_{\text{ff}} \cdot \boldsymbol{n}^{\text{pore}}_{\text{ff}} = -[\rho \boldsymbol{v}]_{\text{pore}} \cdot \boldsymbol{n}^{\text{ff}}_{\text{pore}} \text{ at } \Gamma^{\text{ff}}_{\text{pore}}\,, \tag{4.1}$$

where ρ is density and v is velocity. The above equation can be seen as a Neumann-type boundary condition for the free flow.

In a compositional system, writing the continuity of the mass flux for each component κ at the interface gives:

$$[x^{\kappa}\rho_{\text{mole}}\boldsymbol{v} + \boldsymbol{j}^{\kappa}_{\text{diff, mole}}]_{\text{ff}} \cdot \boldsymbol{n}^{\text{pore}}_{\text{ff}} = -[x^{\kappa}\rho_{\text{mole}}\boldsymbol{v} + \boldsymbol{j}^{\kappa}_{\text{diff, mole}}]_{\text{pore}} \cdot \boldsymbol{n}^{\text{ff}}_{\text{pore}} \text{ at } \Gamma^{\text{ff}}_{\text{pore}}\,, \tag{4.2}$$

where the subscript "mole" indicates that the molar value is used in the calculation and $\boldsymbol{j}^{\kappa}_{\text{diff}}$ is the diffusive mole/mass flux. Equation (4.2) serves as a Neumann-type boundary condition for the free-flow cell at the interface. The mass/mole fraction of a component κ, x^{κ}, in the free-flow cell at the interface is used as a Dirichlet-type boundary condition for the pore at the interface:

$$x^{\kappa}_{\text{pore}} = x^{\kappa}_{\text{ff}} \text{ at } \Gamma^{\text{ff}}_{\text{pore}}\,. \tag{4.3}$$

Momentum balance Three forces contribute to the momentum exchange at the interface: inertial forces, viscous forces and pressure forces. Considering no-slip condition at the surface of the solid part of the porous medium and, thus, the low velocity at the interface, the inertial impacts could be neglected at the interface between a free flow and a porous medium. In the pore-network model, the viscous force is included in the

Hagen-Poiseuille equation to describe the fluid flow. However, the pore-network model does not explicitly provide information about velocity gradient. Thus, the normal momentum transfer at the interface between a pore and the free flow can be described as:

$$[p\boldsymbol{I}]_{\text{pore}} \cdot \boldsymbol{n}_{\text{pore}}^{\text{ff}} = [p\boldsymbol{I} - \mu(\nabla \boldsymbol{v} + \nabla \boldsymbol{v}^T)]_{\text{ff}} \cdot \boldsymbol{n}_{\text{ff}}^{\text{pore}} \tag{4.4}$$

In this work, we ignore the contribution of the free-flow viscous force in the normal momentum transfer, which reduces Eq. (4.4) to:

$$p_{\text{pore}} = p_{\text{ff}} \text{ at } \Gamma_{\text{pore}}^{\text{ff}}\,, \tag{4.5}$$

which means that the pressure of the free-flow grid cell at the interface is assigned to the connected pore body as a Dirichlet-type boundary condition.

We assign the velocity of the pore at the interface to the connected free-flow face, i.e., a Dirichlet-type coupling condition for the free flow:

$$\boldsymbol{v}_{\text{ff}} = \boldsymbol{v}_{\text{pore}} \text{ at } \Gamma_{\text{pore}}^{\text{ff}}\,. \tag{4.6}$$

It should be noted that since the pore-network model does not describe the velocity as a degree of freedom at the pore body, to obtain the pore velocity at the interface, we use the volumetric flow rate in the pore throat connected to the interface pore body divided by the cross-sectional area of the pore body.

To take the tangential momentum transfer between the pore and the free flow into account, we use the concept developed by Weishaupt [2020], which approximates the slip velocity at $\Gamma_{\text{pore}}^{\text{ff}}$ by assuming continuity of shear stress across the interface at the interface. For more details about this approach, we refer to Weishaupt [2020].

Energy balance Having local equilibrium at the interface, we use the free-flow temperature at the interface as a Dirichlet-type coupling condition for the porous medium:

$$T_{\text{pore}} = T_{\text{ff}} \text{ at } \Gamma_{\text{pore}}^{\text{ff}}\,. \tag{4.7}$$

Conservation of energy flux at $\Gamma^{\mathrm{ff}}_{\mathrm{pore}}$ can be described as:

$$\begin{aligned}\left[\rho h\boldsymbol{v} - \lambda\nabla T + \sum_{\kappa}\left(\boldsymbol{j}^{\kappa}_{\mathrm{diff}} h^{\kappa}\right)\right]_{\mathrm{ff}} \cdot \boldsymbol{n}^{\mathrm{pore}}_{\mathrm{ff}} = \\ -\left[\rho h\boldsymbol{v} - \lambda\nabla T + \sum_{\kappa}\left(\boldsymbol{j}^{\kappa}_{\mathrm{diff}} h^{\kappa}\right)\right]_{\mathrm{pore}} \cdot \boldsymbol{n}^{\mathrm{ff}}_{\mathrm{pore}} \text{ at } \Gamma^{\mathrm{ff}}_{\mathrm{pore}}\,.\end{aligned} \tag{4.8}$$

In a non-compositional system, the contribution of diffusive energy flux is zero. Equation (4.8) serves as a Neumann-type boundary condition for the free-flow cell at the interface.

4.3 Interface with droplets

4.3.1 Droplet geometry

Assuming a static condition, a homogeneous surface and a small droplet such that the effect of the gravity field is negligible, the droplet deformation can be neglected and a droplet forms as a part of a sphere having a circular contact area with the solid surface. Equations (4.9) and (4.10) describe a spherical droplet shown in Fig. 4.2, with the droplet radius of curvature, R, the contact radius of the droplet with the solid surface, r_{CA}, the height of the droplet, h, and the droplet contact angle, θ. V_{drop} is the droplet volume and the capillary pressure, p_c, due to the curvature of the droplet surface and the surface tension between the phases, γ_{lg}, is described using Eq. (4.11) [e.g., Baber, 2014].

$$R = \frac{h}{1-\cos\theta} = \frac{r_{\mathrm{CA}}}{\sin\theta}\,, \tag{4.9}$$

$$V_{\mathrm{drop}} = \frac{\pi}{3}h^2(3R-h) = \frac{\pi}{3}r^3_{\mathrm{CA}}\frac{(1-\cos(\theta))^2(2+\cos(\theta))}{(\sin(\theta))^3}\,, \tag{4.10}$$

$$p_c = \frac{2\gamma_{lg}}{R}\frac{2(1-\cos\theta)+\cos\theta(\sin\theta)^2}{(1-\cos\theta)^2(2+\cos\theta)}\,. \tag{4.11}$$

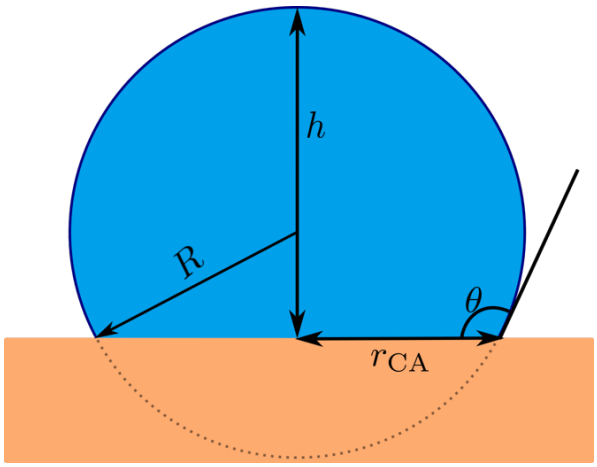

Figure 4.2: A sessile droplet and its descriptive parameters.

4.3.2 Droplet–porous medium interactions

Mass balance A droplet on the surface of the porous medium exchanges mass with the porous medium. Equation (4.12) shows the mass flux, $\dot{m}^{\text{pore}}_{\text{drop}}$, between the droplet and the connected pore through the droplet–pore interface, $\Gamma^{\text{pore}}_{\text{drop}}$. In this equation, ρ_{pore} is the fluid density in the pore, $\boldsymbol{v}^{\text{drop}}_{\text{pore}}$ is the velocity vector of the fluid at $\Gamma^{\text{pore}}_{\text{drop}}$, and $A^{\text{pore}}_{\text{drop}}$ is the area of $\Gamma^{\text{pore}}_{\text{drop}}$. The unit normal vector $\boldsymbol{n}^{\text{pore}}_{\text{drop}}$ is shown in Fig. 4.1. We assume that there is no mole fraction gradient between the droplet and the connected pore body, i.e., there is no diffusive mass exchange between the droplet and the connected pore.

$$\dot{m}^{\text{pore}}_{\text{drop}} = [\rho_{\text{pore}} \boldsymbol{v}^{\text{drop}}_{\text{pore}}] \cdot \boldsymbol{n}^{\text{pore}}_{\text{drop}} A^{\text{pore}}_{\text{drop}} \text{ at } \Gamma^{\text{pore}}_{\text{drop}} . \tag{4.12}$$

Momentum balance At the interface between a droplet and a pore, $\Gamma^{\text{pore}}_{\text{drop}}$, as shown in Fig. 4.3a, continuity of forces in the normal direction to the droplet surface is described as:

$$\boldsymbol{F}_{\text{pore}} + \boldsymbol{F}_{\text{drop}} = 0 \text{ at } \Gamma^{\text{pore}}_{\text{drop}} , \tag{4.13}$$

where $\boldsymbol{F}_{\text{pore}}$ and $\boldsymbol{F}_{\text{drop}}$ are the forces exerted on the droplet–pore interface due to the pore body and the droplet pressure, respectively. Substitution of the forces by the multiplication of the pressure and an infinitesimal area of the droplet–pore interface, $\mathrm{d}a^{\text{pore}}_{\text{drop}}$, results in a coupling condition based on the droplet and pore pressure.

$$[p_{\text{pore}} \boldsymbol{n}^{\text{drop}}_{\text{pore}} + p_{\text{drop}} \boldsymbol{n}^{\text{pore}}_{\text{drop}}] \cdot \boldsymbol{n}^{\text{pore}}_{\text{drop}} \, \mathrm{d}a^{\text{pore}}_{\text{drop}} = 0 \text{ at } \Gamma^{\text{pore}}_{\text{drop}} . \tag{4.14}$$

Rearrangement of Eq. (4.14) gives:

$$p_{\text{pore}} = p_{\text{drop}} \text{ at } \Gamma_{\text{drop}}^{\text{pore}}, \tag{4.15}$$

which shows that the pore pressure is equal to the droplet pressure at $\Gamma_{\text{drop}}^{\text{pore}}$. We assume no pressure gradient inside the droplet, which leads to equality of the pressure inside the droplet and the pressure at the droplet–pore interface. In the pore-network model, only one pressure is considered for each pore body. According to these assumptions, Eq. (4.15) not only holds at the interface, but also for the entire droplet and the connected pore, $\Omega_{\text{drop}} \cup \Omega_{\text{pore}}$.

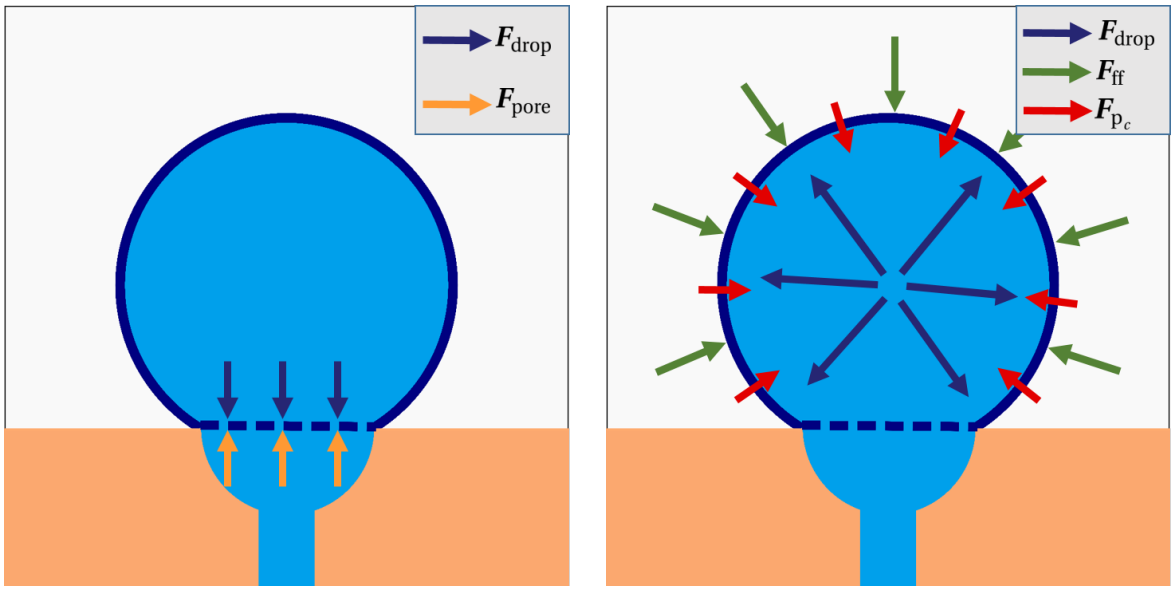

(a) (b)

Figure 4.3: Forces acting on: a) the drop–pore interface, and b) the drop–free-flow interface.

Energy balance At $\Gamma_{\text{drop}}^{\text{pore}}$, the temperatures of the droplet and the pore are assumed to be equal.

$$T_{\text{drop}} = T_{\text{pore}} \text{ at } \Gamma_{\text{drop}}^{\text{pore}}. \tag{4.16}$$

Assuming no temperature gradient inside the droplet due to the small size of the droplet, we assign one value for temperature for the entire droplet. Making the same assumption for the pore in pore-network model, the temperature of a pore is described using only one value. Thus, in our model, Eq. (4.15) is not only valid at the interface, but also for the whole droplet and the pore, $\Omega_{\text{drop}} \cup \Omega_{\text{pore}}$. Consequently, energy exchange between

the pore and the droplet, $\dot{e}^{\text{drop}}_{\text{pore}}$, occurs only through convection. The convective heat transfer can be expressed by Eq. (4.17).

$$\dot{e}^{\text{pore}}_{\text{drop}} = [\rho_{\text{pore}} h_{\text{pore}} \boldsymbol{v}^{\text{drop}}_{\text{pore}}] \cdot \boldsymbol{n}^{\text{pore}}_{\text{drop}} A^{\text{pore}}_{\text{drop}} \text{ at } \Gamma^{\text{pore}}_{\text{drop}} . \tag{4.17}$$

It is worth mentioning that considering the same temperature and pressure for the droplet and the pore, the density, ρ, and the specific enthalpy, h, of the droplet and the pore are equal as well. Figure 4.4 illustrates the droplet mass and energy exchange with the connected pore and the surrounding free flow.

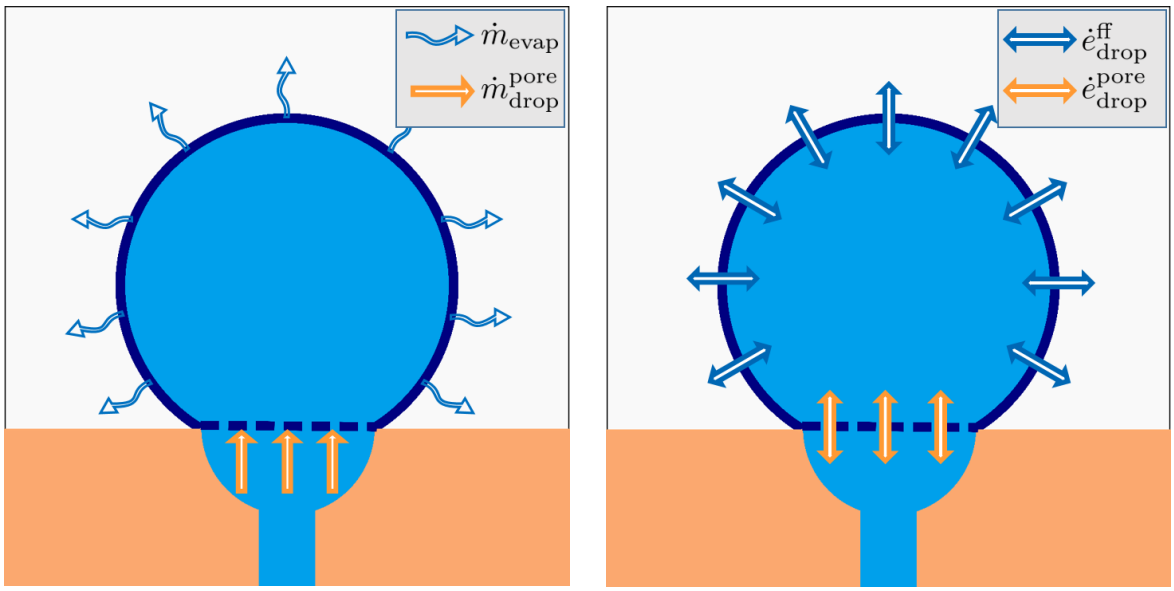

(a) (b)

Figure 4.4: a) Mass exchange between the free-flow, droplet and pore, and b) Energy exchange between the free-flow, droplet and pore.

4.3.3 Droplet–free-flow interactions

Mass balance In a compositional system, a droplet and the surrounding free flow exchange mass through evaporation from the surface of the droplet, $\Gamma^{\text{ff}}_{\text{drop}}$.

$$\dot{m}^{\text{ff}}_{\text{drop}} = \dot{m}_{\text{evap}} \text{ at } \Gamma^{\text{ff}}_{\text{drop}} , \tag{4.18}$$

where $\dot{m}_{\text{evap}}$ is the evaporative flux from the droplet surface to the free flow. In Section 4.5, we discuss how to compute the evaporative flux in detail.

The part of the free-flow domain that is occupied by the droplet, Ω_{drop}, is treated using a Dirichlet-type condition for mole/mass fraction, i.e., we assign the mole/mass fraction of the droplet for component κ to the cells that are occupied by the droplet.

$$x_{\text{ff}}^{\kappa} = x_{\text{drop}}^{\kappa} \text{ at } \Omega_{\text{drop}} \,. \tag{4.19}$$

Momentum balance Continuity of normal forces at the drop surface, $\Gamma_{\text{drop}}^{\text{ff}}$, at each infinitesimal area, $\mathrm{d}a$, needs to be fulfilled:

$$\boldsymbol{F}_{\text{ff}} + \boldsymbol{F}_{p_c} + \boldsymbol{F}_{\text{drop}} = 0 \text{ at } \Gamma_{\text{drop}}^{\text{ff}} \,, \tag{4.20}$$

where $\boldsymbol{F}_{\text{ff}}$ is the total free-flow force acting on each point of the droplet–free-flow interface, $\boldsymbol{F}_{p_c}$ is the capillary force on the droplet surface and $\boldsymbol{F}_{\text{drop}}$ is the droplet force exerted by the fluid inside the droplet on the droplet surface (see Fig. 4.3b).

We have that $\boldsymbol{F}_{\text{ff}}$ is the sum of three forces:

$$\boldsymbol{F}_{\text{ff}} = \boldsymbol{F}_{\rho v^2} + \boldsymbol{F}_{p} + \boldsymbol{F}_{\tau_{\text{ff}}} \,. \tag{4.21}$$

Considering an infinitesimal area of the droplet surface, $\mathrm{d}a_{\text{drop}}^{\text{ff}}$, each force can be computed as:

- Inertial force: $\boldsymbol{F}_{\rho v^2} = [(\rho \boldsymbol{v} \otimes \boldsymbol{v})_{\text{ff}}\, \boldsymbol{n}_{\text{ff}}^{\text{drop}}] \cdot \boldsymbol{n}_{\text{drop}}^{\text{ff}}\, \mathrm{d}a_{\text{drop}}^{\text{ff}}$,
- Pressure force: $\boldsymbol{F}_{p} = [p_{\text{ff}}\, \boldsymbol{n}_{\text{ff}}^{\text{drop}}] \cdot \boldsymbol{n}_{\text{drop}}^{\text{ff}}\, \mathrm{d}a_{\text{drop}}^{\text{ff}}$,
- Shear force: $\boldsymbol{F}_{\tau_{\text{ff}}} = [(-\boldsymbol{\tau})_{\text{ff}}\, \boldsymbol{n}_{\text{ff}}^{\text{drop}}] \cdot \boldsymbol{n}_{\text{drop}}^{\text{ff}}\, \mathrm{d}a_{\text{drop}}^{\text{ff}}$, where $\boldsymbol{\tau}$ is the shear stress tensor.

The capillary force, $\boldsymbol{F}_{p_c}$, is defined as:

- Capillary force: $\boldsymbol{F}_{p_c} = [p_c\, \boldsymbol{n}_{c}^{\text{drop}}] \cdot \boldsymbol{n}_{\text{drop}}^{c}\, \mathrm{d}a_{\text{drop}}^{\text{ff}}$, where the subscript c indicates that the capillary force stems from the curvature of the droplet surface. It should be noted that in fact $\boldsymbol{n}_{c}^{\text{drop}} = \boldsymbol{n}_{\text{ff}}^{\text{drop}}$ and $\boldsymbol{n}_{\text{drop}}^{c} = \boldsymbol{n}_{\text{drop}}^{\text{ff}}$.

The droplet force exerted by the fluid inside the droplet on the droplet surface is:

- Droplet force: $\boldsymbol{F}_{\text{drop}} = [p_{\text{drop}}\, \boldsymbol{n}_{\text{drop}}^{\text{ff}}] \cdot \boldsymbol{n}_{\text{drop}}^{\text{ff}}\, \mathrm{d}a_{\text{drop}}^{\text{ff}}$.

Thus, Eq. (4.20) can be rewritten as:

$$\boldsymbol{F}_{\rho v^2} + \boldsymbol{F}_p + \boldsymbol{F}_{\tau_{\mathrm{ff}}} + \boldsymbol{F}_{p_c} + \boldsymbol{F}_{\mathrm{drop}} = 0 \text{ at } \Gamma^{\mathrm{ff}}_{\mathrm{drop}} \,. \tag{4.22}$$

Using the definition of each force, we derive Eq. (4.23), which shows the mechanical coupling condition at the interface between the droplet and the free flow.

$$[((\rho \boldsymbol{v} \otimes \boldsymbol{v}) + p\boldsymbol{I} + (-\boldsymbol{\tau}))_{\mathrm{ff}} + p_c \boldsymbol{I} - p_{\mathrm{drop}} \boldsymbol{I}] \boldsymbol{n}^{\mathrm{drop}}_{\mathrm{ff}} \cdot \boldsymbol{n}^{\mathrm{ff}}_{\mathrm{drop}} \, \mathrm{d}a^{\mathrm{ff}}_{\mathrm{drop}} = 0 \text{ at } \Gamma^{\mathrm{ff}}_{\mathrm{drop}} \,. \tag{4.23}$$

The part of the free-flow domain that is occupied by the droplet is treated using a Dirichlet-type condition for velocity. As mentioned before, in the discretized free-flow domain using the staggered-grid finite volume approach, the velocity degrees of freedom are located at the face of grid cells. Thus, we assign zero velocity to the faces that are occupied by the droplet.

$$\boldsymbol{v}_{\mathrm{ff}} = 0 \text{ at } \Omega_{\mathrm{drop}} \,. \tag{4.24}$$

Energy balance Energy exchange between the droplet and the free flow takes place at the surface of the droplet through two mechanisms: heat conduction and heat transfer due to the evaporation. Heat conduction occurs as a result of temperature gradient between the surface of the droplet and the surrounding free flow. Evaporation from the surface of the droplet also causes energy exchange in the form of molecular diffusive energy transfer. Summing up the energy transfers through these two mechanisms and integrating over the surface of the droplet gives the total energy exchange between the droplet and the free flow:

$$\dot{e}^{\mathrm{ff}}_{\mathrm{drop}} = \int_{A^{\mathrm{ff}}_{\mathrm{drop}}} [-\lambda_{\mathrm{ff}} \nabla T^{\mathrm{ff}}_{\mathrm{drop}} + \boldsymbol{f}_{\mathrm{evap}} h^{\kappa}_{\mathrm{drop}}] \cdot \boldsymbol{n}^{\mathrm{ff}}_{\mathrm{drop}} \mathrm{d}a \text{ at } \Gamma^{\mathrm{ff}}_{\mathrm{drop}} \,. \tag{4.25}$$

Here, λ_{ff} is the free-flow conductivity, $\nabla T^{\mathrm{ff}}_{\mathrm{drop}}$ refers to the temperature gradient between the droplet surface and the free flow, $\boldsymbol{f}_{\mathrm{evap}}$ is the evaporative flux computed by Eq. (4.47), and $h^{\kappa}_{\mathrm{drop}}$ is the specific enthalpy of the main component, e.g., H_2O, in the droplet.

The droplet temperature is assigned to the part of the free-flow domain that is occupied by the droplet, Ω_{drop}:

$$T_{\mathrm{ff}} = T_{\mathrm{drop}} \text{ at } \Omega_{\mathrm{drop}} \,. \tag{4.26}$$

Droplet impact on the free-flow field We discussed the balance equations at the droplet–free-flow and droplet–pore interfaces. We also mentioned that we assign the droplet related properties to the parts of the free flow which are occupied by droplets, Ω_{drop}. In this section, we explain how the free-flow parts invaded by the droplet are recognized and treated.

To include the impact of the droplet on the free flow, we take a simplified approach. In this approach, we keep the free-flow domain single-phase and the free flow sees the droplet as an obstacle, which might grow or shrink over time. In the discretized free-flow domain, the free-flow cell centers or faces that are occupied by the droplet are recognized. It should be noted that we do not solve the degrees of freedom that are inside the droplet, but they are treated using Dirichlet-type conditions. That means, we assign a fix value to the degree of freedom which is located inside the droplet. In what follows, we explain the steps need to be taken:

1. Considering the mass exchange of the droplet with the free flow and the pore, the droplet volume is calculated.

2. Having the contact angle and computing the droplet radius and position using Eqs. (4.9) and (4.10), we identify grid cells and cell faces in the free-flow region affected by the droplet. To do so, a dimensionless variable, β, is defined and used. For velocity degree of freedom which is located on the face of the free-flow grid cell, β_{face} is defined as:

$$\beta_{\text{face}} = \frac{\text{Area of the face occupied by the droplet}}{\text{Total area of the face}} \,. \tag{4.27}$$

   For other degrees of freedom which are located at the cell center, such as temperature and mole/mass fraction, we have:

$$\beta_{\text{cell}} = \frac{\text{Volume of the cell occupied by the droplet}}{\text{Total cell volume}} \,. \tag{4.28}$$

   If $\beta_{\text{cell}} = 1$ for a cell, the grid cell is completely inside the droplet. Otherwise, if $0 < \beta_{\text{cell}} < 1$, the cell is partially occupied by the droplet and it is recognized as an interface grid cell. The cell faces are treated similarly.

3. The free-flow gird cells which are inside the droplet are treated using Eqs. (4.19) and (4.26).

4. The free-flow gird faces which are inside the droplet are treated using Eq. (4.24).

5. The coupled system is solved, including the droplet impact on the free-flow domain.

Furthermore, we calculate the temperature and mole/mass fraction gradient between the cells which are recognized as interface grid cells and the cell inside the droplet. The free-flow shear and inertial forces are calculated on the interface grid faces and the pressure force on the interface grid cells. Figure 4.5 shows the free-flow grid cells inside the droplet and interface grid cells.

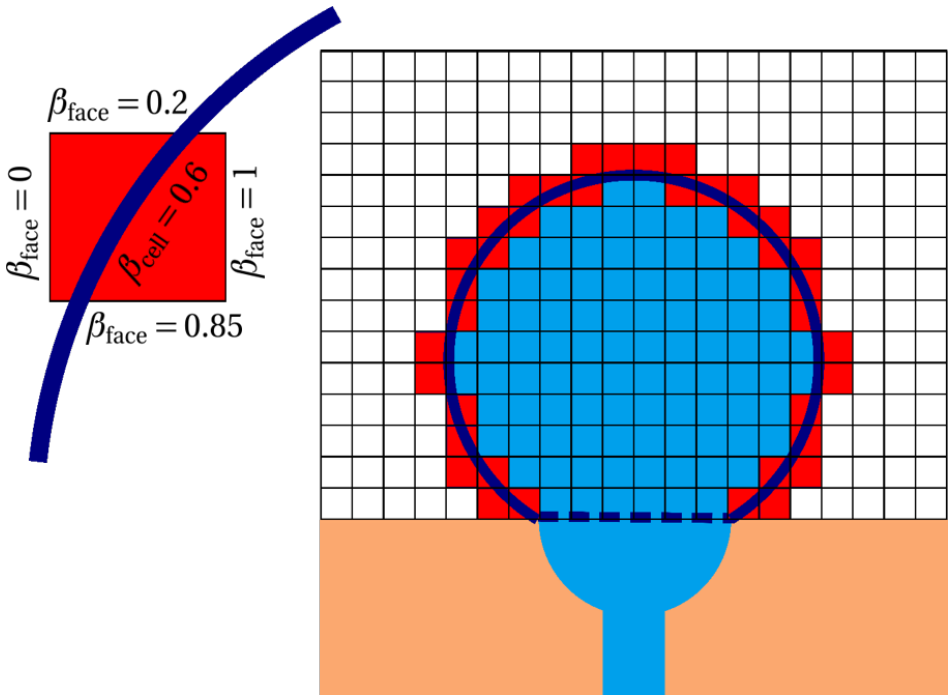

Figure 4.5: The blue grid cells are completely inside the droplet and the red ones are the grid cells that are partially occupied by the droplet.

4.3.4 Coupling concept for free flow and porous medium with droplets

To describe the exchange through the interface between a free flow and a porous medium including droplets' impacts, we need to combine the droplet–pore interactions (see Section 4.3.2), and droplet–free-flow interactions (discussed in Section 4.3.3).

Mass balance The total mass balance for the droplet in a coupled system can be derived through adding up the droplet mass exchange with the porous medium and the free flow.

$$\frac{\mathrm{d}m_{\mathrm{drop}}}{\mathrm{d}t} + \dot{m}^{\mathrm{pore}}_{\mathrm{drop}} + \dot{m}^{\mathrm{ff}}_{\mathrm{drop}} = 0\,, \tag{4.29}$$

where

$$\begin{aligned} &\frac{\mathrm{d}m_{\mathrm{drop}}}{\mathrm{d}t} = \frac{\mathrm{d}(\rho_{\mathrm{drop}} V_{\mathrm{drop}})}{\mathrm{d}t}\,, \\ &\dot{m}^{\mathrm{pore}}_{\mathrm{drop}} = [\rho_{\mathrm{pore}} \boldsymbol{v}^{\mathrm{drop}}_{\mathrm{pore}}] \cdot \boldsymbol{n}^{\mathrm{pore}}_{\mathrm{drop}} A^{\mathrm{pore}}_{\mathrm{drop}}\,, \\ &\dot{m}^{\mathrm{ff}}_{\mathrm{drop}} = \dot{m}_{\mathrm{evap}}\,. \end{aligned} \tag{4.30}$$

The evaporation from the droplet surface to the free flow is discussed in Section 4.5.

As we discussed before, for the parts of the free-flow domain that are occupied by the droplet, we set the mole/mass fractions of the components to the droplet values (Eq. (4.19)).

Momentum balance Since we don't introduce a new primary variable for the droplet, we write the momentum coupling condition for the pore connected to the droplet, including the droplet effect. Thus, we substitute the droplet pressure in Eq. (4.23) with the pore pressure according to Eq. (4.15) which leads to:

$$[((\rho \boldsymbol{v} \otimes \boldsymbol{v}) + p\boldsymbol{I} + (-\boldsymbol{\tau}))_{\mathrm{ff}} + p_c \boldsymbol{I} - p_{\mathrm{pore}} \boldsymbol{I}] \boldsymbol{n}^{\mathrm{drop}}_{\mathrm{ff}} \cdot \boldsymbol{n}^{\mathrm{ff}}_{\mathrm{drop}}\, \mathrm{d}a^{\mathrm{ff}}_{\mathrm{drop}} = 0\,. \tag{4.31}$$

As we discussed before, we assign zero velocity to the parts of the free-flow domain that are occupied by the droplet (Eq. (4.24)).

Energy balance Since the droplet temperature is equal to the temperature of the interface pore in our model, we write the energy balance for the interface pore and take the pore–free-flow energy exchange through the droplet into account. Considering the configuration shown in Fig. 4.6 and having no sink/source term, the energy balance for the interface pore body, i, can be written as:

$$\frac{\mathrm{d}e_i}{\mathrm{d}t} + \dot{e}^{j}_{i} + \dot{e}^{\mathrm{drop}}_{i} + \dot{e}^{\mathrm{ff}}_{i} = (Vq^e)_i\,. \tag{4.32}$$

The first term describes the energy storage in the interface pore body, $\dot{e}_i^j$ is the energy exchange between the interface pore body i and the neighboring pore body j, $\dot{e}_i^{\text{drop}}$ is the energy exchange between the interface pore body, and the droplet and $\dot{e}_i^{\text{ff}}$ is the energy exchange between the interface pore body and the free flow, which occurs through the droplet.

For a case where fluid flows from pore body j to pore body i and from pore body i to the droplet, pore body j is the upstream pore body for pore body i, while pore body i itself is the upwind pore body for the droplet.

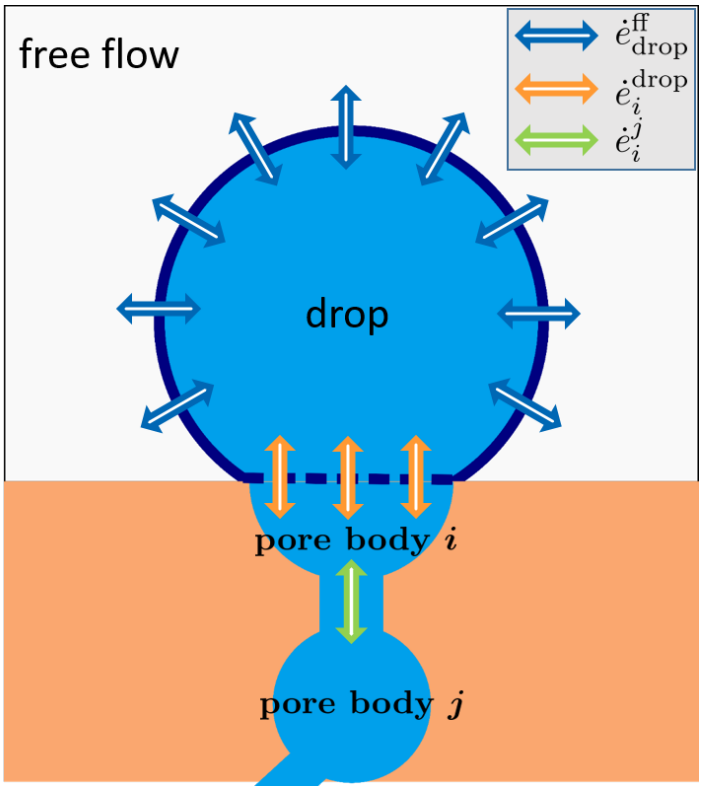

Figure 4.6: Free-flow–droplet–pore energy exchange at the interface.

We have that $\dot{e}_i^j$ can be described using the following equation:

$$\dot{e}_i^j = [\rho_j h_j \boldsymbol{v}_j^i - \lambda_{ji} \nabla T_i^j] \cdot \boldsymbol{n}_i^j A_i^j \,. \tag{4.33}$$

To describe the energy exchange between the interface pore body and the free flow through the droplet, we assume that all energy exchanged at the droplet–free-flow

interface, $\dot{e}^{\mathrm{ff}}_{\mathrm{drop}}$, is evenly distributed throughout the droplet and the interface pore body. Thus, the amount of $\dot{e}^{\mathrm{ff}}_{i}$ is a proportion of $\dot{e}^{\mathrm{ff}}_{\mathrm{drop}}$ that affects pore body i. Accordingly, the ratio of the pore body volume, V_i, to the sum of the pore body and droplet volume, $V_i + V_{\mathrm{drop}}$, is used to calculate $\dot{e}^{\mathrm{ff}}_{i}$:

$$\dot{e}^{\mathrm{ff}}_{i} = \left(\frac{V_i}{V_i + V_{\mathrm{drop}}} \right) \dot{e}^{\mathrm{ff}}_{\mathrm{drop}} \,. \tag{4.34}$$

Rewriting Eq. (4.32) using the definition of each term gives the following relation, which describes the energy balance for pore body i at the interface,

$$\begin{aligned} &\frac{\mathrm{d}(\rho_i u_i V_i)}{\mathrm{d}t} + [\rho_j h_j \boldsymbol{v}^i_j - \lambda_{ji} \nabla T^j_i] \cdot \boldsymbol{n}^j_i A^j_i + \rho_i h_i \boldsymbol{v}^{\mathrm{drop}}_i \cdot \boldsymbol{n}^{\mathrm{drop}}_i A^{\mathrm{drop}}_i \\ &+ \left(\frac{V_i}{V_i + V_{\mathrm{drop}}} \right) \int_{A^{\mathrm{ff}}_{\mathrm{drop}}} [-\lambda_{\mathrm{ff}} \nabla T^{\mathrm{ff}}_{\mathrm{drop}} + \boldsymbol{f}_{\mathrm{evap}} h^{\kappa}_{\mathrm{drop}}] \cdot \boldsymbol{n}^{\mathrm{ff}}_{\mathrm{drop}} \mathrm{d}a = (V q^e)_i \,. \end{aligned} \tag{4.35}$$

In the above equation, $\boldsymbol{f}_{\mathrm{evap}}$ is the evaporative flux vector. We treat the energy exchange at the interface for the interfacial pore body as a source/sink term. Such a source/sink term is the sum of the droplet–pore convection heat transfer and the proportion of the energy exchange between the droplet and the free flow, which impacts the pore body. Equation (4.36) shows the computation of the source/sink term related to the droplet, which affects pore body i at the interface, Q^{drop}_i:

$$\begin{aligned} Q^{\mathrm{drop}}_i = &- \rho_i h_i \boldsymbol{v}^{\mathrm{drop}}_i \cdot \boldsymbol{n}^{\mathrm{drop}}_i A^{\mathrm{drop}}_i \\ &- \left(\frac{V_i}{V_i + V_{\mathrm{drop}}} \right) \int_{A^{\mathrm{ff}}_{\mathrm{drop}}} [-\lambda_{\mathrm{ff}} \nabla T^{\mathrm{ff}}_{\mathrm{drop}} + \boldsymbol{f}_{\mathrm{evap}} h^{\kappa}_{\mathrm{drop}}] \cdot \boldsymbol{n}^{\mathrm{ff}}_{\mathrm{drop}} da \,. \end{aligned} \tag{4.36}$$

Using the source/sink term given by the above equation, the energy balance relation for pore body i, Eq. (4.35), can be rewritten as:

$$\frac{\mathrm{d}(\rho_i u_i V_i)}{\mathrm{d}t} + [\rho_j h_j \boldsymbol{v}^i_j - \lambda_{ji} \nabla T^j_i] \cdot \boldsymbol{n}^j_i A^j_i = (V q^e)_i + Q^{\mathrm{drop}}_i \,. \tag{4.37}$$

As we discussed before, for the parts of the free-flow domain that are occupied by the droplet, we set the temperature to the droplet temperature (Eq. (4.26)).

4.4 Droplet dynamics

After discussing the droplet interactions with a free flow and a porous medium, in this section, first, we focus on the droplet formation and growth at the interface. Then, we discuss the detachment of the droplet. Droplet formation and growth are functions of the droplet–free-flow and the droplet–porous medium mass exchange. Detachment of a droplet occurs due to the impact of the free-flow forces on the droplet.

4.4.1 Droplet formation and growth

Both the free flow and porous medium flow can affect the formation of a droplet at the surface of the porous medium. In the case of droplet formation as a result of the porous medium liquid breakthrough, it is the porous medium that play the role of a supplier for the droplet and acts in favor of the droplet growth. In fact, the droplet stores the mass coming from the porous medium. Evaporation from the surface of the droplet in the free flow region, on the contrary, causes shrinkage of the droplet. Summing up these two interactions, the variation of the droplet volume can be expressed using Eq. (4.29).

Growth mode A droplet might grow at the interface in constant contact angle mode, constant contact radius mode, or a combination of them. In our concept, to describe how a droplet grows, we divide the droplet growth process into two periods:

1. Initially, when a droplet just emerged from a pore and starts growing, the droplet contact angle is less than the advancing contact angle of the hydrophobic surface. In this stage, the droplet contact area is equal to the pore surface area and the droplet contact angle grows until it reaches the surface advancing contact angle. In other words, a constant contact radius and an increasing contact angle describes the droplet growth and the triple contact line is pinned in this stage to the pore perimeter.

2. The second stage begins once the droplet contact angle reaches the advancing contact angle of the surface. At this time we switch to a constant contact angle approach, which means that the droplet grows while its contact angle is constant,

i.e, equal to the surface contact angle, and the droplet contact radius increases, i.e., the droplet contact area expands.

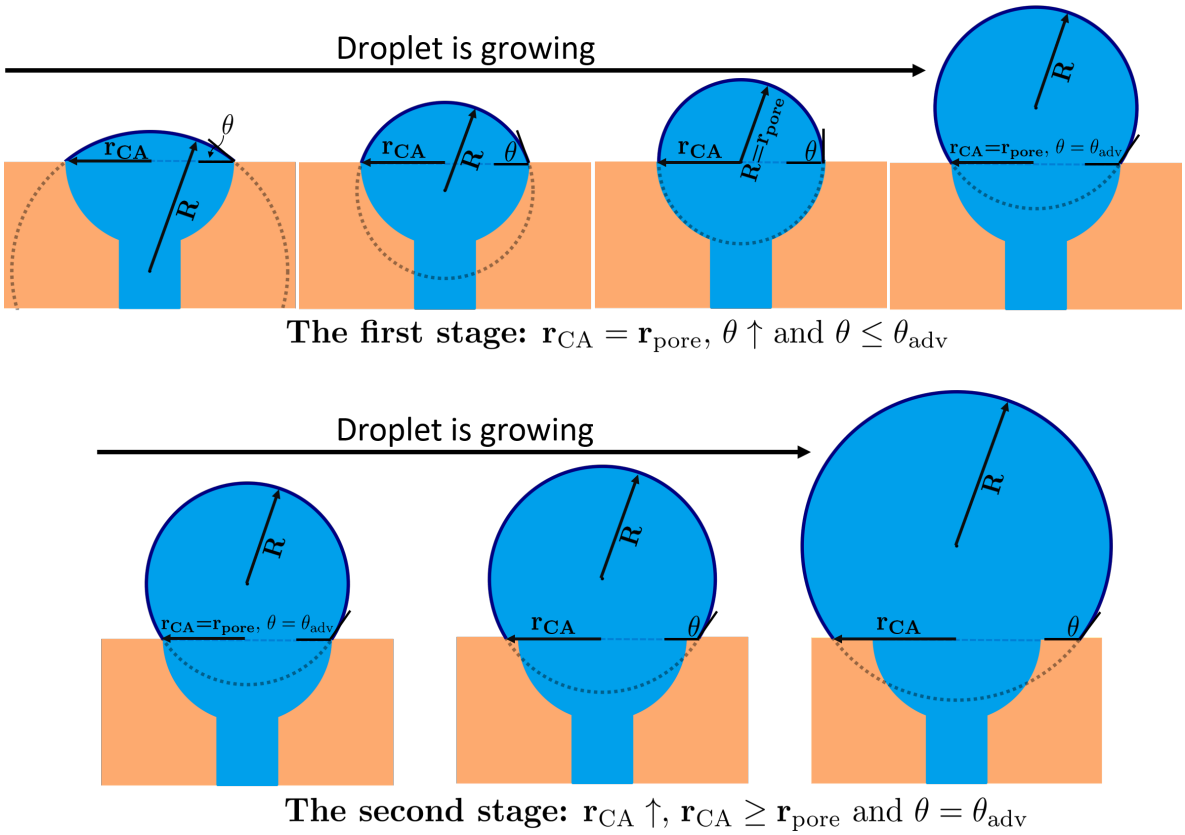

Figure 4.7: Droplet formation and growth on a pore, where θ is the droplet contact angle before it reaches the surface advancing contact angle, θ_{adv}, while the droplet contact radius is equal to the pore radius, r_{pore}. After the triple contact line expands and leaves the pore perimeter, the droplet contact radius is r_{CA}.

It should be noted that in both stages, we assume that the droplet is part of a sphere (i.e., non-deformed droplet), whose radius can be calculated based on the droplet contact angle and contact radius described in Section 4.3.1. Figure 4.7 shows the stages of a droplet growth on the surface of a pore.

4.4.2 Droplet detachment

The detachment of a droplet from the porous medium surface has a significant impact on the coupled system of a free flow–porous medium. To predict the droplet detachment

due to the free-flow influence, it is necessary to recognize and calculate the forces acting in favor and against the droplet detachment.

Forces involved in the droplet detachment The free flow around a droplet exerts forces on the droplet surface on every point of the droplet–free-flow interface, $\Gamma^{\mathrm{ff}}_{\mathrm{drop}}$. Integration of the forces over the droplet surface gives the total free-flow force, which acts on the droplet as a whole. This force can be decomposed to a force in the flow direction (i), called drag force, and a force perpendicular to the flow direction (j) called lift force:

$$\boldsymbol{F}^{\mathrm{ff}}_{\mathrm{total}} = \boldsymbol{F}_{\mathrm{drag}} + \boldsymbol{F}_{\mathrm{lift}} \,. \tag{4.38}$$

The drag force is the main force that acts to detach the droplet from the solid surface which can be calculated as:

$$\boldsymbol{F}_{\mathrm{drag}} = \boldsymbol{F}_{\tau i} + \boldsymbol{F}_{pi} + \boldsymbol{F}_{\rho v^2 i} \,, \tag{4.39}$$

where

$$\begin{aligned}
\boldsymbol{F}_{\tau i} &= \int_{A^{\mathrm{ff}}_{\mathrm{drop}}} [(-\boldsymbol{\tau})\boldsymbol{n}]^{\mathrm{drop}}_{\mathrm{ff}} \cdot \boldsymbol{n}_i \, \mathrm{d}a^{\mathrm{ff}}_{\mathrm{drop}} \,, \\
\boldsymbol{F}_{pi} &= \int_{A^{\mathrm{ff}}_{\mathrm{drop}}} [p\boldsymbol{n}]^{\mathrm{drop}}_{\mathrm{ff}} \cdot \boldsymbol{n}_i \, \mathrm{d}a^{\mathrm{ff}}_{\mathrm{drop}} \,, \\
\boldsymbol{F}_{\rho v^2 i} &= \int_{A^{\mathrm{ff}}_{\mathrm{drop}}} [(\rho \boldsymbol{v} \otimes \boldsymbol{v})\boldsymbol{n}]^{\mathrm{drop}}_{\mathrm{ff}} \cdot \boldsymbol{n}_i \, \mathrm{d}a^{\mathrm{ff}}_{\mathrm{drop}} \,.
\end{aligned} \tag{4.40}$$

$\boldsymbol{F}_{\tau i}$, $\boldsymbol{F}_{pi}$ and $\boldsymbol{F}_{\rho v^2 i}$ are the total shear, pressure and inertial force components acting on the droplet in the flow direction. $\boldsymbol{n}_i$ is the unit vector in the flow direction (i).

The impacts of the free-flow forces on the droplet, before the detachment, are the deformation in the shape of the droplet as well as the contact angle hysteresis on the triple contact line between the free-flow fluid, the droplet fluid and the solid.

The adhesion force, $\boldsymbol{F}_{\mathrm{adh}}$, is the sum of forces acting on each point of the triple contact line, which tries to keep the droplet attached to the surface in the presence of the free-flow force. The adhesion force is influenced by the droplet deformation, the droplet fluid–free-flow fluid interfacial tension and the wettability state of the porous medium. The resultant adhesion force can be decomposed into two components: one tangential to the solid surface and another one perpendicular to the solid interface. The component

acting tangential to the solid surface results from the droplet contact angle hysteresis. Thus, we use the name "hysteresis force", $\boldsymbol{F}_{\mathrm{hyst}}$, to refer to it. Figure 4.8 shows a sessile drop in two-dimension under influence of the free-flow forces acting on the droplet surface, the forces acting on the triple contact line, and the weight force. For instance, For the two-dimensional droplet shown in Fig. 4.8, we have the following relation in i direction:

$$\boldsymbol{F}_{\mathrm{hyst}} = \boldsymbol{F}_{\mathrm{adh,i}} = \boldsymbol{F}_{\mathrm{rec,i}} + \boldsymbol{F}_{\mathrm{adv,i}}\,, \tag{4.41}$$

where $\boldsymbol{F}_{\mathrm{rec}}$ and $\boldsymbol{F}_{\mathrm{adv}}$ are forces acting on the triple contact line at the receding and advancing point. It should be noted, since we describe the forces acting on a droplet as a whole, we assume the center of the droplet–solid/pore contact area as the point of action of the resultant adhesion force. In a three-dimensional case, integration of the forces on the triple contact line gives the total adhesion force.

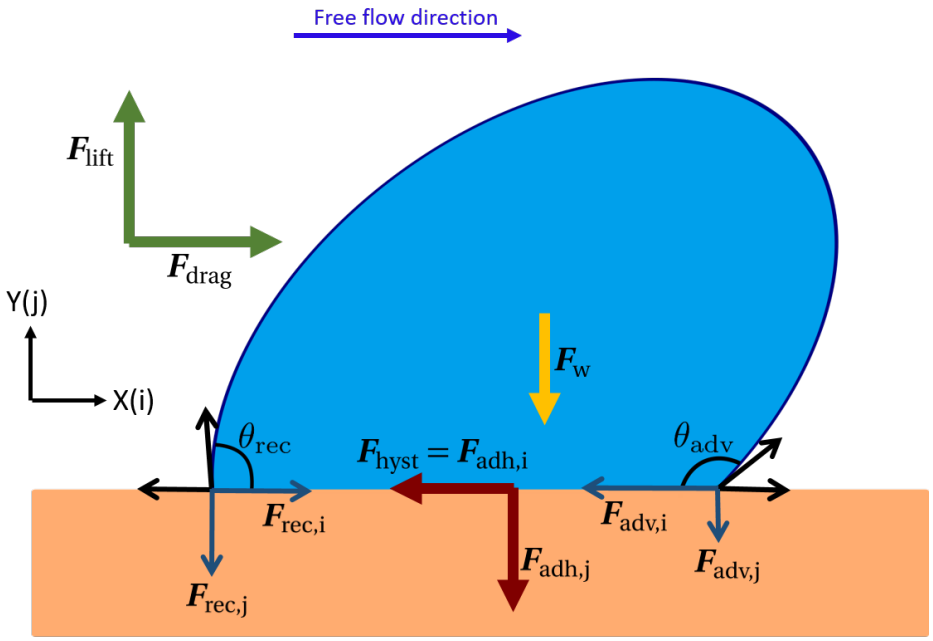

Figure 4.8: Free-flow drag force and hysteresis force acting on the droplet.

Droplet detachment criteria The triple contact line becomes unstable either once the free-flow lift overcome the sum of adhesion force component perpendicular to the solid surface and the droplet weight, or when the free-flow drag force exceeds the adhesion force tangential to the solid surface (hysteresis force). Whether a droplet first slides

for some time at the interface and then detaches or detaches rather immediately once the triple contact line becomes unstable, depends on different factors, e.g., surface wettability, fluids surface tension, droplet contact angle hysteresis, droplet growth rate, pore geometry and free-flow velocity [Li et al., 2012, Wang et al., 2011]. In the developed model here, we assume that the movement of the triple contact line due to the free-flow forces is the detachment criterion, which determines when the droplet detaches from the solid surface. Such a criterion has shown to be a proper indicator of the droplet detachment [Kumbur et al., 2006, Cho et al., 2012]. Thus, the detachment can occur when either of the following criteria is fulfilled:

$$\boldsymbol{F}_{\text{lift}} > \boldsymbol{F}_{\text{adh,j}} + \boldsymbol{F}_{\text{w}} \,, \tag{4.42}$$

$$\boldsymbol{F}_{\text{drag}} > \boldsymbol{F}_{\text{adh,i}} = \boldsymbol{F}_{\text{hyst}} \,. \tag{4.43}$$

It has been shown that the first criterion, relation (4.42), is more difficult to be satisfied. Therefore, the second criterion, relation (4.43), is the critical condition which is used to predict the droplet detachment [Cho et al., 2012, Kumbur et al., 2006, Basu et al., 1997].

The maximum hysteresis force The maximum hysteresis force, $\boldsymbol{F}_{\text{hyst}}^{\max}$, occurs when a droplet experiences the ultimate difference between the advancing and receding contact angles. Such a situation happens just before the droplet detachment. Thus, having a proper estimation of this force leads to a more accurate prediction of the droplet detachment.

Several expressions to calculate the hysteresis force have been proposed [Chen et al., 2005, Kumbur et al., 2006, Cho et al., 2012]. Kumbur et al. [2006] assumed a linear variation of the contact angle along the triple contact line and derived Eq. (4.44) by integrating the forces on the contact line to describe the maximum hysteresis force:

$$\begin{aligned}\boldsymbol{F}_{\text{hyst}}^{\max} = \gamma_{lg}\pi R \sin\theta [& \frac{\sin(\Delta\theta^{\max} - \theta_{\text{adv}}) - \sin(\theta_{\text{adv}})}{\Delta\theta^{\max} - \pi} + \\ & \frac{\sin(\Delta\theta^{\max} - \theta_{\text{adv}}) - \sin(\theta_{\text{adv}})}{\Delta\theta^{\max} + \pi}] \,.\end{aligned} \tag{4.44}$$

In Eq. (4.44), $\Delta\theta^{\max}$ is the maximum difference between the advancing and receding

contact angle. Assuming two semi-circles with contact angles of receding and advancing contact angles, Chen et al. [2005] proposed the following equation to calculate the maximum hysteresis force on the triple contact line:

$$\boldsymbol{F}_{\text{hyst}}^{\max} = 2\gamma_{lg}\pi R \sin\theta \sin(\frac{\theta_{\text{adv}} + \theta_{\text{rec}}}{2}) \sin\left(\frac{\Delta\theta^{\max}}{2}\right). \tag{4.45}$$

Cho et al. [2012] et al. simplified Eq. (4.45) by assuming $\theta = (\theta_{\text{adv}} + \theta_{\text{rec}})/2$ and proposed the following equation:

$$\boldsymbol{F}_{\text{hyst}}^{\max} = 2\gamma_{lg}\pi R \sin^2\theta \sin\left(\frac{\Delta\theta^{\max}}{2}\right). \tag{4.46}$$

4.5 Droplet evaporation

The mass transfer between a droplet and the surrounding free flow occurs through evaporation from the surface of the droplet. We describe the droplet evaporation as a quasi-stationary diffusion driven process [Fuchs, 2013], in which the diffusion of the vapor from the surface of the droplet to the gaseous free flow controls the evaporation rate. In other words, the vapor concentration gradient between the droplet surface and the surrounding free flow determines the droplet evaporation. Such a process can be described using the Fick's first law. Decomposing the evaporative flux, $\boldsymbol{f}_{\text{evap}}$, into its Cartesian components, i.e., in i and j directions in a two-dimensional setup, we use the Fick's first law to calculate the diffusive flux in each direction from the surface of the droplet into the neighboring free-flow cell, N, as shown by Eq. (4.47) for i-direction. The flux in j-direction is calculated similarly.

$$f_{\text{evap},i} = \rho_{\text{g,ff}} D_{\text{g,ff}}^{\kappa} \frac{X_{\text{g,ff,int}}^{\kappa} - X_{\text{g,ff},N}^{\kappa}}{d_i}. \tag{4.47}$$

In the above equation, subscripts "g" and "ff" are used to emphasize that the evaporation occurs in the gas phase from the surface of the droplet to the surrounding free flow. Thus, the parameters used to calculate the evaporative flux are related to the free flow, i.e., gas phase. The mass fraction of component κ in the gas phase at the interface grid face and in the neighboring cell are respectively indicated by $X_{\text{g,ff,int}}^{\kappa}$ and $X_{\text{g,ff},N}^{\kappa}$, and d_i is the distance between the interface grid face and the center of the neighboring

grid cell in i-direction (see Fig. 4.9b). It should also be noted that the subscripts "int" and "N" indicate the values at the interface grid face and neighboring cell, respectively. Here, the interface grid face is the face of the grid cell that is occupied by the droplet and has a neighboring cell that is outside the droplet.

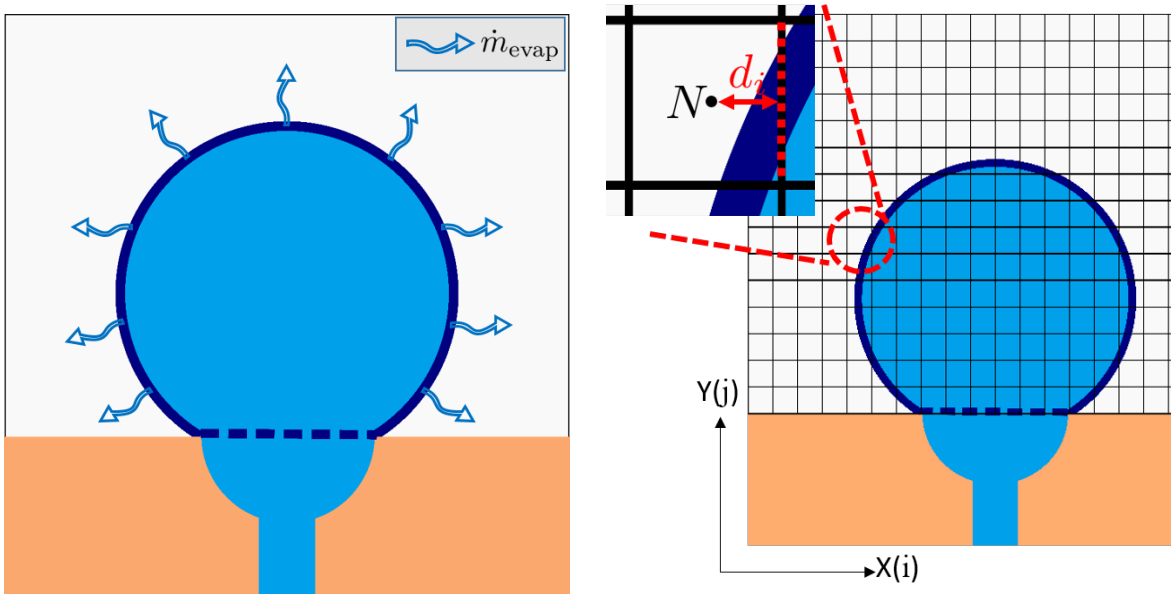

(a) (b)

Figure 4.9: a) Evaporation from the surface of a droplet into the free flow, and b) an interface grid face (red dashed line) and its neighboring grid cell (N).

Integrating the evaporative flux over the surface of the droplet gives the total mass flux leaving the droplet surface due to evaporation, $\dot{m}_{\mathrm{evap}}$.

$$\dot{m}_{\mathrm{evap}} = \int_{A^{\mathrm{ff}}_{\mathrm{drop}}} \boldsymbol{f}_{\mathrm{evap}} \cdot \boldsymbol{n}^{\mathrm{ff}}_{\mathrm{drop}} \mathrm{d}a \,. \tag{4.48}$$

In the above equation, we use $\boldsymbol{n}^{\mathrm{ff}}_{\mathrm{drop}}$ to get the evaporative flux from the surface of the droplet in radial direction.

To compute the evaporative flux using Eq. (4.47), we need the value of $X^{\kappa}_{\mathrm{g,ff,int}}$ beforehand. To obtain that, we assume mechanical, thermal and chemical equilibrium at the surface of the droplet, $\Gamma^{\mathrm{ff}}_{\mathrm{drop}}$. Such equilibrium conditions are demonstrated in Fig. 4.10.

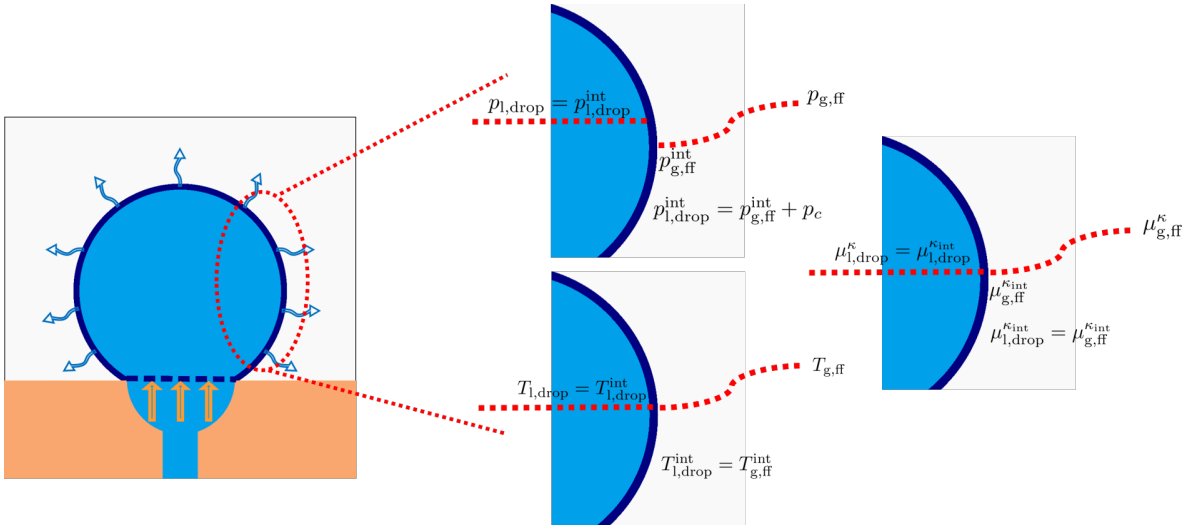

Figure 4.10: Equilibrium conditions at the surface of the droplet.

The mechanical equilibrium at the droplet surface means that the droplet pressure at $\Gamma^{\mathrm{ff}}_{\mathrm{drop}}$ is equal to the sum of free-flow pressure and capillary pressure. The thermal equilibrium indicates that the temperature of the droplet and the free flow are the same at the droplet surface. Based on the chemical equilibrium, a component κ in the liquid phase (droplet) and the gas phase (free flow) must have the same chemical potential, μ^{κ}, at the droplet surface.

Having chemical equilibrium at $\Gamma^{\mathrm{ff}}_{\mathrm{drop}}$, for the vapor component, κ, Raoult's law can be employed to compute the partial pressure of that component in the gas phase using the vapor pressure, $p^{\kappa}_{\mathrm{vap}}$, and the mole fraction of the component κ in the liquid phase, $x^{\kappa}_{\mathrm{l,drop}}$:

$$p^{\kappa}_{\mathrm{g,ff}} = p^{\kappa}_{\mathrm{vap}} x^{\kappa}_{\mathrm{l,drop}} \quad \text{at } \Gamma^{\mathrm{ff}}_{\mathrm{drop}}\,. \tag{4.49}$$

Then, using the Dalton's law, the mole fraction of the component κ in the gas phase, $x^{\kappa}_{\mathrm{g,ff}}$, at $\Gamma^{\mathrm{ff}}_{\mathrm{drop}}$ is computed as the ratio of the partial pressure of the component κ to the total gas pressure, $p_{\mathrm{g,ff}}$:

$$x^{\kappa}_{\mathrm{g,ff}} = \frac{p^{\kappa}_{\mathrm{g,ff}}}{p_{\mathrm{g,ff}}} \quad \text{at } \Gamma^{\mathrm{ff}}_{\mathrm{drop}}\,. \tag{4.50}$$

Converting mole fraction to mass fraction is straightforward. We assign the value computed by Eq. (4.50) to the cells occupied by the droplet. To identify the grid cells in the free-flow domain that are affected by the droplet, we take the approach explained in Section 4.3.3. In this study, it is assumed that the mole fraction of the

main component in the liquid phase is equal to one.

Evaporation mode In our model, the droplet evaporation mode might follow the constant contact area mode or a combination of constant contact angle and constant contact area modes. If the droplet contact radius is equal to the pore body radius, the droplet shrinkage due to the evaporation occurs in a constant contact area mode. In this mode, the contact angle, θ, of the droplet diminishes during the evaporation, while the droplet contact area remains constant. Shrinkage of a droplet with an initial contact radius greater than the pore radius, however, starts with a constant contact angle mode. The droplet contact radius decreases as long as it is greater than the pore radius, whereas the droplet contact angle remains constant and equal to the surface contact angle, θ_{eq}. By further shrinkage of the droplet and when the droplet contact radius reduces to the pore radius, the droplet contact angle begins to decrease and the contact radius stays constant. Such a process is illustrated by Fig. 4.11.

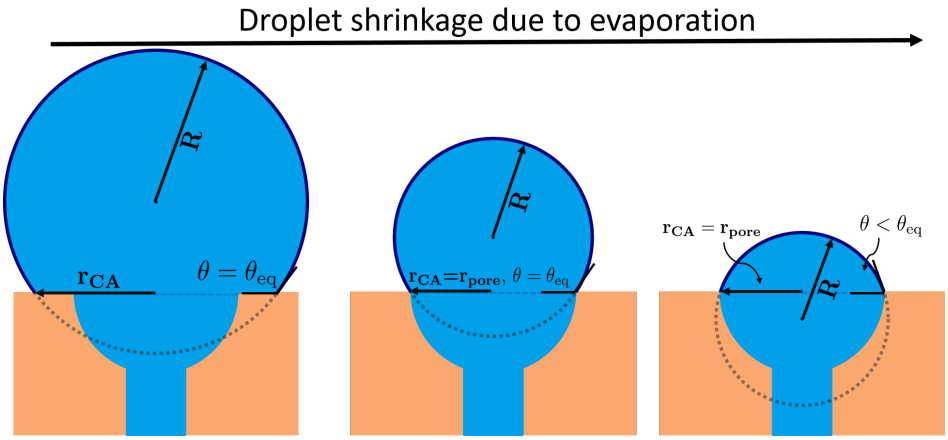

Figure 4.11: Droplet evaporation modes.

5 Results and discussions for droplet dynamics at the interface: Droplet formation, growth, and detachment

In this chapter, at first, we focus on the droplet formation and growth at the interface and compare the simulation results with the experimental data. Then, we discuss simulation results of droplet detachment and compare them with experimental data and simulation results from ANSYS Fluent. After that, we analyze the interactions between two neighboring droplets formed at the interface on the droplet detachment. At the end, we present a showcase consists of a free-flow channel coupled with a pore network to show the application of the developed model in describing multiple droplets formation and growth at the interface.

5.1 Droplet formation and growth: Comparison with experiment*

5.1.1 Experimental setup and image analysis

A cylindrical Polytetrafluoroethylene (PTFE) block with diameter of 1.5×10^{-2} m and height of 3×10^{-2} m is used, which a pore with diameter of 1.495×10^{-3} m is drilled at its center. A high precision peristaltic pump (Ismatec REGLO Digital MS-2/12) is connected to the bottom end of the pore and injects potassium iodide (KI)-doped water with volume flow of $Q = 8.85 \times 10^{-10}$ m^3/s$\pm 4.83 \times 10^{-11}$ m^3/s until a drop forms

*A large portion of this section was previously published by International Journal of Multiphase Flow (Elsevier) [Ackermann et al., 2023].

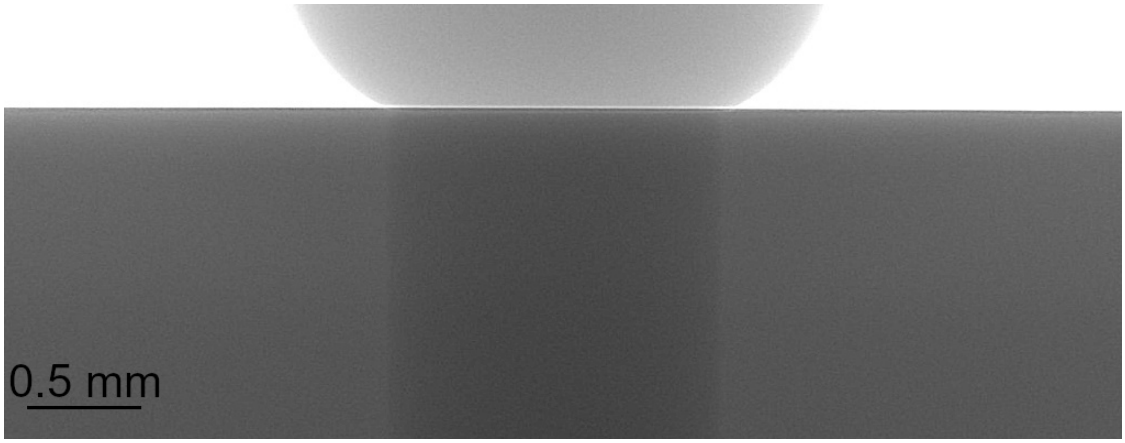

Figure 5.1: High-resolution X-ray radiographies of the single pore in the center of the PTFE cylindrical block [Ackermann et al., 2023].

on the surface. A high resolution X-ray radiography of the pore entrance is shown in Fig. 5.1. The mass ratio of potassium iodide to water was 1:6, yielding a surface tension of $\sigma = 0.0681$ N/m.

To monitor the drop formation and growth onto the pore, high-resolution X-ray radiographies were employed. For more details about the x-ray radiographies used in this work and the components of the X-ray microCT equipment, we refer to Ackermann et al. [2023] and Santini et al. [2013].

Using a metrological calibration, the resolution of the X-ray radiographies was determined [Santini et al., 2016], to be used in image analysis. Measured distances have an error twice the meter-scale, so that droplet radii could be determined with a precision of about 1×10^{-5} m.

During acquisition, the projections were corrected for charge accumulation of the detector, the so called "dark-field", and were normalized by "bright-field" correction. The latter characterizes the response of the non-uniform radiography acquisition system due to variation in the detector sensitivity and the X-ray source flux density. The normalized projections are post-processed in Matlab®. Ackermann et al. [2023] describe the image processing in more details. Figure 5.2 depicts some post-processed projections for a growing droplet and the extracted contours for a droplet pinned to the pore at different time steps.

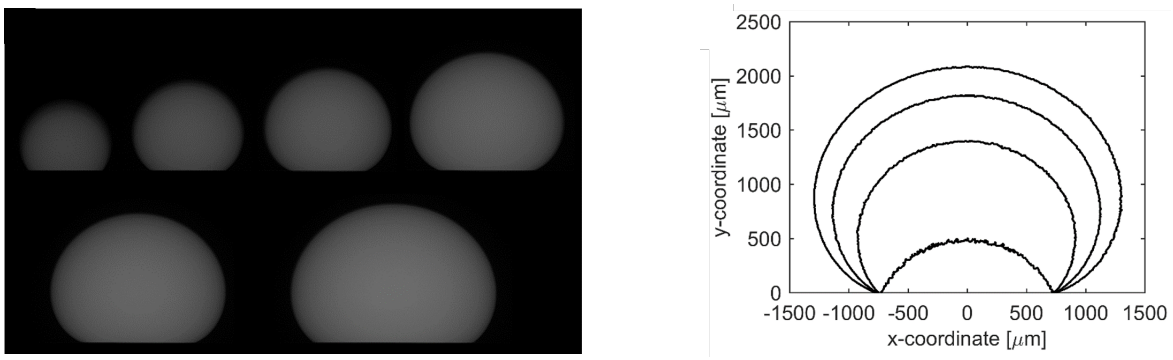

(a) (b)

Figure 5.2: a) Post-processed radiographies for a growing droplet, b) extracted contours for a droplet pinned to the pore at different time steps [Ackermann et al., 2023].

To compute the drop volume, the half-droplet contours were rotated around the y-axis. From the obtained solid of revolution, the enclosed volume was determined with the disc method. To extract the contact angle from the obtained data, the drop profile is fitted to the Young Laplace equation [Santini et al., 2013], which is evaluated at the triple contact line. The absolute measurement error for contact angles smaller than 160° results less than 1° (for validation, see Santini et al. [2013] and Guilizzoni [2011]).

To estimate the droplet mean curvature, κ, droplet profiles have been approximated as symmetrical ellipses. Measuring vertical and horizontal half axis lengths, R_{ver} and R_{hor}, respectively, the mean curvature of the droplet surface was calculated as shown in Eq. (5.1):

$$\kappa = \frac{\kappa_{\text{ver}} + \kappa_{\text{hor}}}{2} = \frac{\frac{1}{R_{\text{ver}}} + \frac{1}{R_{\text{hor}}}}{2} \,. \tag{5.1}$$

The mean droplet radius of curvature, R, is the inverse of the droplet mean curvature and can be determined with an accuracy of $\pm 4 \times 10^{-5}$ m.

$$R = \frac{1}{\kappa} \,. \tag{5.2}$$

5.1.2 Simulation setup

We use an inlet and an outlet pore bodies connected via a single pore throat to model the hole in the cylindrical PTFE block used in the experiment. The pore bodies and the pore throat have the same radius of 7.475×10^{-4} m and the length of the pore

throat is 15×10^{-3} m. The network is initially filled with water and a Neumann in-flow boundary condition is applied to the inlet pore body. Water is injected to the inlet pore body with the inflow rate of 8.85×10^{-10} m^3/s $\pm$ 4.83×10^{-11} m^3/s. The outlet pore body is connected to the free-flow domain. The droplet starts growing in a constant contact radius mode. Once the contact angle of the droplet reaches the surface contact angle, which is here equal to 140°, the droplet contact radius expands and its contact angle remains equal to the surface contact angle.

5.1.3 Comparison between the simulation results and experimental data

Figure 5.3 compares the simulation results and the experimental data for the change in droplet volume over time. The comparison of droplet contact angle is shown by Fig. 5.4. As can be seen, the experimental data show an initial stage of growing contact angle with time. However, after reaching the surface contact angle, the drop contact angle remains almost constant with small fluctuations around the surface contact angle. Such behavior shows that assuming a constant contact angle mode for the second stage of the droplet growth is reasonable. It should be noted that the droplet is constantly growing. That means that after depinning of the triple contact line from the pore perimeter, the triple contact line is most of the time advancing. Thus, the contact angle measured in the experiment is the dynamic contact angle. According to the results, the model is able to predict the behavior of the droplet contact angle.

Figure 5.5 represents the droplet radius of curvature variation versus time. According to the simulation results, the radius of curvature peaks early in time. Then it plunges until it reaches the pore radius, and it starts an upward trend. Considering the droplet formation and growth process, at a short time after the water injection into the throat, a small droplet forms on the surface which has a small contact angle and the contact area of the throat. That results into a large radius of curvature and explains the peak in the simulation results. However, the experimental results do not show such a behavior at the beginning due to the difference of time resolution in the simulation and the time resolution used in the experiment to monitor the droplet growth. In other words, if a smaller time-step size is applied in the simulation, a higher peak in the droplet radius of curvature is expected at the early time. However, a small time-step size in the

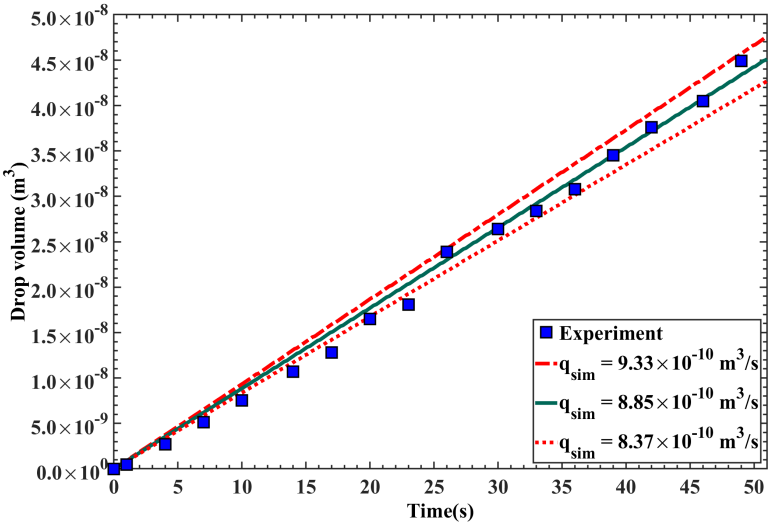

Figure 5.3: Comparison of the drop volume from the experiment (squares) and simulation (lines).

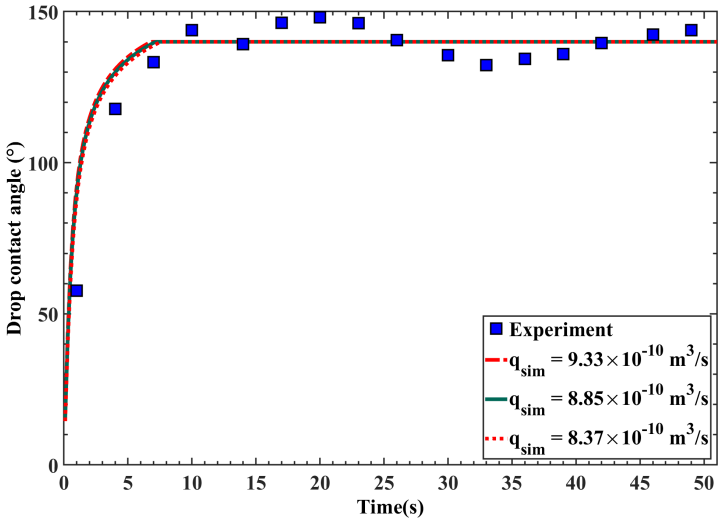

Figure 5.4: Comparison of drop contact angle from experiment (squares) and simulation (lines).

experiment such that the peak in the radius of curvature is observed, can not be easily applied. In addition, looking into the whole droplet formation and growth process, such a momentary phenomenon is not much of importance.

Overall, the results show a good match between the experiment and simulation results and that our approach is able to describe the formation and growth of the droplet.

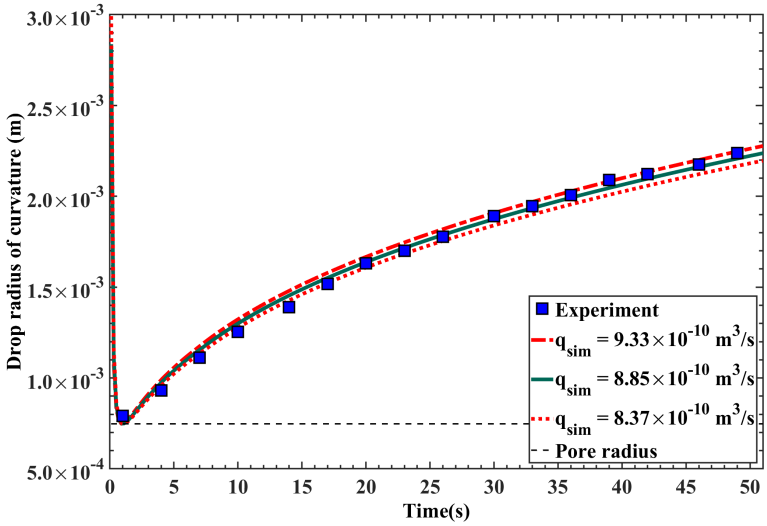

Figure 5.5: Comparison of drop radius of curvature from experiment (squares) and simulation (lines).

5.2 Droplet detachment

5.2.1 Comparison with experimental data

In this section, we compare the results obtained from the developed model in this work and the experimental data from the study conducted by Theodorakakos et al. [2006b] for the detachment of a single droplet by the surrounding free flow.

5.2.1.1 Experimental and simulation setup

In the experiment presented by Theodorakakos et al. [2006b], the experimental setup consists of a 7 mm × 2.7 mm × 34 mm (width × height × length) gas channel. A Dirichlet-type boundary condition for velocity is applied to the channel inlet, i.e., the gas flows uniformly into the channel at the inlet. The outlet is at atmospheric pressure, which is a Dirichlet-type pressure boundary condition. Droplets of different sizes are placed 17 mm downstream of the inlet on the bottom wall of the channel, which is made of carbon cloth and has a static contact angle of 145°. The ultimate advancing and receding contact angles of the surface are 150° and 90° respectively. The experiment starts with generating droplets using a syringe and placing them on the solid surface.

In the simulation, we use a free-flow channel with the same size used in the experiment. A small porous medium composed of two pore bodies connected with a pore throat is connected to the bottom wall of the channel to form a droplet through injection of water at the inlet pore body until a droplet with a desirable size forms on the solid surface. The pore bodies and the pore throat have the same radius of 0.1 mm and the length of the pore throat is 0.8 mm length. After formation of the droplet, the gas starts flowing into the channel at a low flow rate with a uniform velocity profile, followed by gradually increasing of the inlet gas flow until the droplet detaches. Figure 5.6 shows the simulation setup and the applied boundary conditions.

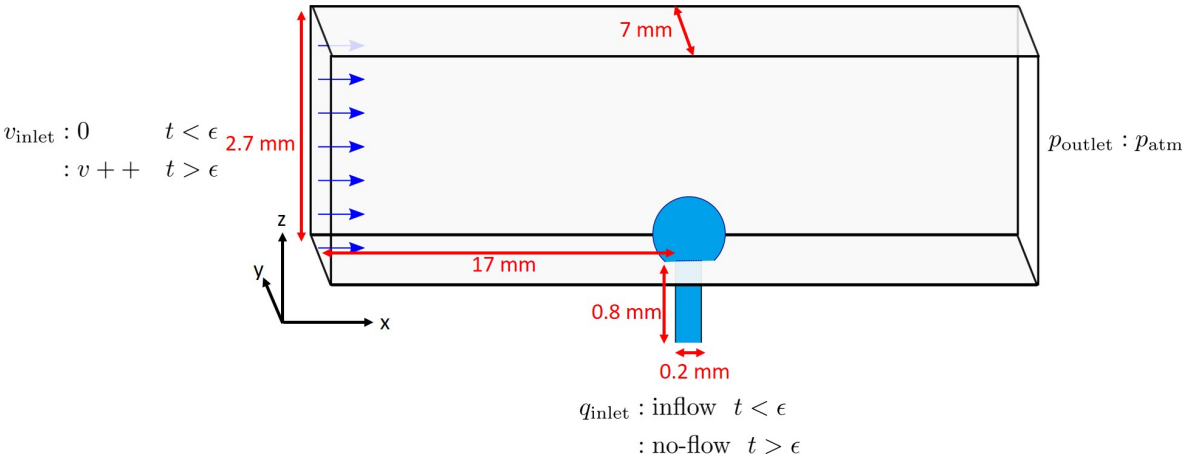

Figure 5.6: The setup used for the comparison between the simulation results and the experimental data provided by Theodorakakos et al. [2006b].

5.2.1.2 Results

Figure 5.7 shows the comparison between the experimental results from the study by Theodorakakos et al. [2006b] and the results of our developed model. According to the results, the model shows a high ability to predict the droplet detachment. The difference between the simulation and experimental data could stem from the droplet deformation in the experiment, which is not included in the model. For a droplet with certain diameter, the three-dimensional simulations predict a higher free-flow velocity required for detachment than predictions by the two-dimensional simulations. This could be explained by the more reduction in the area available for the free flow in the two-dimensional case than in the three-dimensional case. In other words, the two-

dimensional simulation overestimates the partial blockage of the free-flow channel by the droplet.

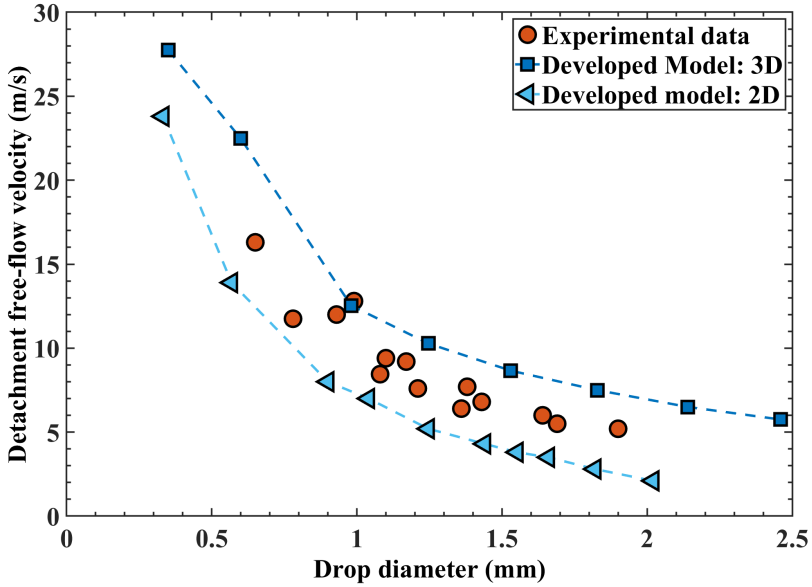

Figure 5.7: Comparison of the experimental data provided by Theodorakakos et al. [2006b] and the results of our developed model for the free flow velocity detaching the droplets in an air channel.

5.2.2 Analysis and comparison with ANSYS Fluent†

In this section, first, we will examine the impact of grid resolution in the free-flow domain on the simulation results. Then, we will look at the droplet dynamics and the variation of forces acting on the droplet with the droplet growth. After that, we will compare the results predicted by the developed model for the droplet detachment with the ANSYS Fluent model. Then, the separation line obtained from the developed model will be compared with the line predicted by analytical/empirical approaches. At the end, we will present a showcase, which consists of a free-flow channel coupled with a pore network, including multiple droplets formation at the interface.

†This section was previously published by Transport in Porous Media (Springer) [Veyskarami et al., 2023].

5.2.2.1 Model setup

Figure 5.8 shows the setup in which air flows through a channel with dimensions of 1.35 mm × 4.15 mm × 1 mm (width × length × height). A vertical pore consists of two pore bodies and a pore throat with a circular cross-section (radius = 0.15 mm and length = 0.5 mm) is connected to the middle of the bottom wall of the channel. Air enters the channel at the inlet with a fully developed laminar velocity profile given by [Hartnett and Kostic, 1989]:

$$v(y,z) = v_{\max} \cdot \left(1 - \left(\frac{y-a}{a}\right)^2\right) \cdot \left(1 - \left(\frac{z-b}{b}\right)^{2.3}\right), \tag{5.3}$$

where $v_{\max}$ is the maximum flow velocity at the center line, and a and b are half of the width and height of the channel, respectively. Atmospheric pressure is assigned as the Dirichlet boundary condition for pressure at the channel outlet. Initially, there is no flow in the channel and the air pressure is equal to the atmospheric pressure.

Water is injected into the inlet of the pore at a constant mass flow rate of 10^{-5} kg/s. A droplet forms and grows in the channel at the outlet of the throat until it is detached due to the air flow in the channel.

For comparison purposes, we use the above-described setup for simulations using a model based on the volume of fluid method, which is implemented in ANSYS Fluent. ANSYS Fluent R2019 is chosen for this study due to its established and stable implementation of a multiphase solver and the applicability on high performance computing clusters for fast calculations [Michalkowski et al., 2022].

5.2.2.2 Grid resolution in the free-flow domain

To find the suitable grid resolution in the free-flow domain such that it preserves accuracy but at the same time prevents high computational cost, we apply three different grid resolutions in a case with maximum free-flow velocity of 20 m/s, mean velocity of 9.3 m/s, at the inlet of the free-flow channel. For the fine grid resolution, we use 110400 grid cells to discretize the domain. We use 16875 cells for the medium grid resolution and 6000 cells to generate the course grids in the free-flow domain. However, in all cases, a refinement algorithm is employed to have smaller grids around the droplet and

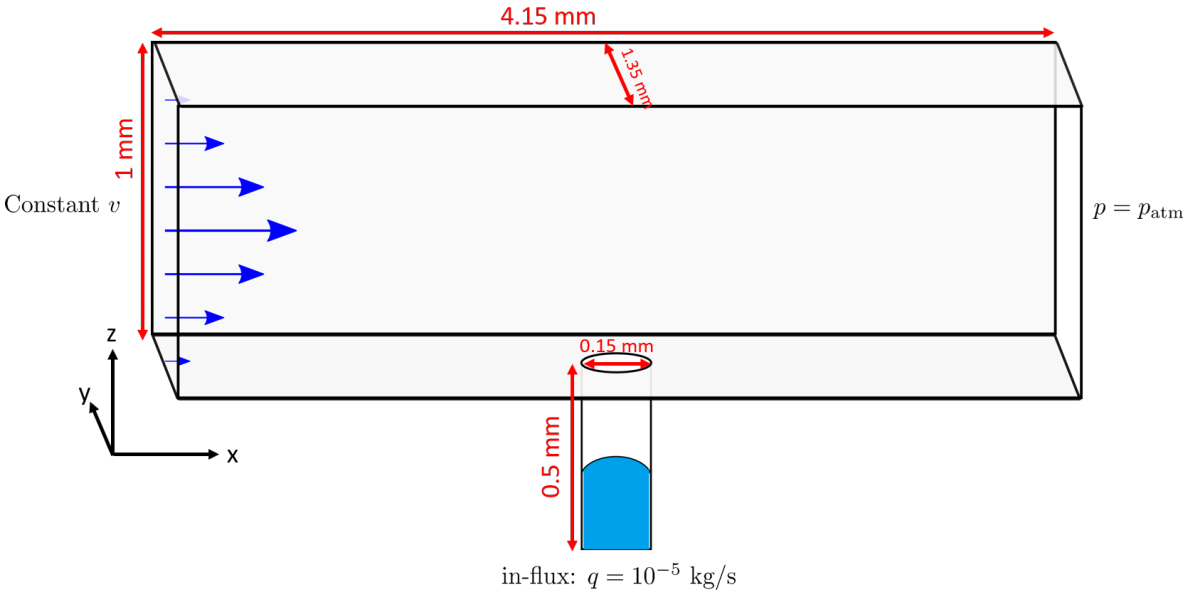

Figure 5.8: The simulation setup used in the droplet detachment analysis.

larger grids in areas far from the droplet. For instance, in the fine grid resolution we have 48000 cells in the area where droplet presence is probable, whereas there are 2700 grid cells in the coarse grid resolution. Figure 5.9 illustrates the aforementioned grid resolutions. In this figure, the area in the middle of the channel with smaller grid cells is where the droplet is more likely to invade, and therefore, a finer grid is used. It should be noted that the fluid flows in x-direction in the free-flow channel.

Table 5.1 compares the predicted droplet properties once the detachment occurs for the three grid resolutions in the free-flow channel. It can be seen that using the coarse grid in the channel results in more deviation from the predicted values by the simulation using the fine grid. The simulation results using the medium and fine grid resolutions show less than one percent difference in prediction of the detachment height and a bit more than two percent difference for the detachment volume. Since the grid resolution

Table 5.1: Predicted droplet height and volume at the detachment time using three different grid resolution in the free-flow channel with $v_{\max} = 20$ m/s. Δ is the difference between the predicted value using the fine grid resolution and the other resolutions.

	Detachment height(m)	$\Delta_h\%$	Detachment volume(m^3)	$\Delta_V\%$
Fine grid	6.30×10^{-4}	–	1.70×10^{-10}	–
Medium grid	6.25×10^{-4}	0.73	1.66×10^{-10}	2.17
Coarse grid	5.97×10^{-4}	5.26	1.45×10^{-10}	14.97

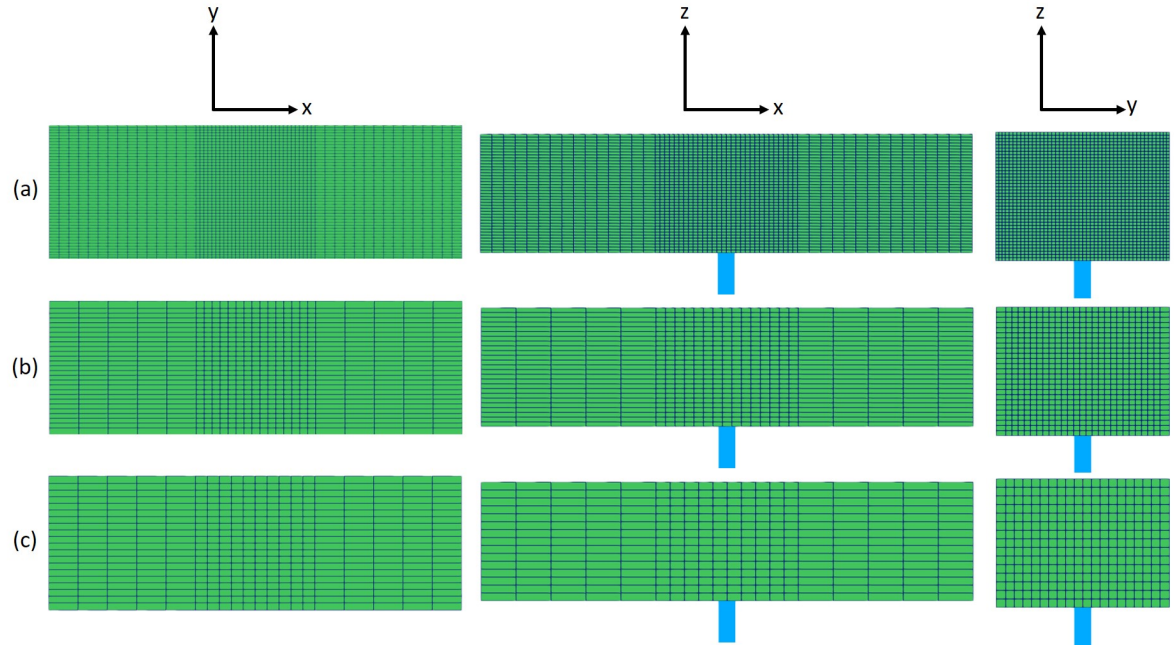

Figure 5.9: The three grid configurations used to analyze the impact of the grid resolution: a) the fine grid, b) the medium grid and c) the coarse grid resolution.

in the free-flow domain mainly affects the forces acting on the droplet, we compare the variation of the free-flow drag force during the droplet growth predicted by the three aforementioned grid resolutions in Fig. 5.10. As can be seen, the drag force increases almost steadily and free of fluctuation when the fine grid is used. Whereas by coarsening the grid, the fluctuation increases, although the trend remains the same. This happens because having a fine grid resolution provides a better estimation of the free-flow grid faces invaded by the droplet in each time step. In fact, since in our approach the invasion of the grid face happens once the droplet occupies the whole grid face, the impact of this sudden invasion on the free-flow field is larger when the grid is coarser. It is also noticeable that the level of fluctuation becomes stronger over time due to the fact that the droplet invades and blocks the grid cells, which have a stronger influence on the free-flow velocity field.

Taking all these into account, it is reasonable to use the medium grid resolution for the remaining simulations, as it provides less computational cost while gives almost the same results as the fine grid. It is worth to note that the ANSYS Fluent model uses more than 2×10^6 grid cells.

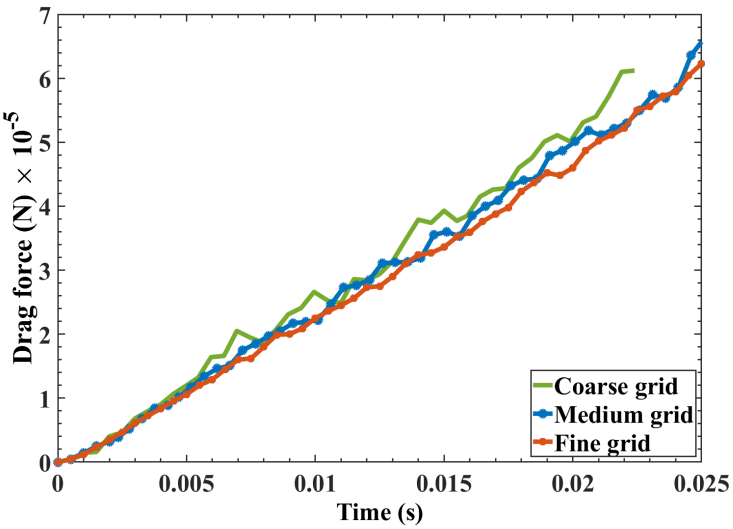

Figure 5.10: The impact of the grid resolution on the free-flow drag force in the free-flow channel with a maximum flow velocity of 20 m/s.

5.2.2.3 Droplet dynamics

Figure 5.11 shows how droplet properties and forces vary over time during a one formation-growth-detachment period of a droplet at the interface. We use the contact angles reported by Theodorakakos et al. [2006b] for carbon cloth. The equilibrium contact angle of water with the solid surface is 145° at the channel wall and in the pore. The maximum advancing contact angle is 150° and the minimum receding contact angle is 90°. The results shown in Fig. 5.11 belong to the case that the maximum velocity of the free flow at the inlet of the channel is 15 m/s, i.e., mean velocity of 6.98 m/s. Figure 5.11a shows that the volume of the droplet increases with a constant rate over time due to the constant injection rate into the throat. Figure 5.11a also shows that the variation rate of the radius of curvature and the height of the droplet decreases by time, i.e., by the growth of the droplet. We can see in the Fig. 5.11b that the contact radius of the droplet stays constant and the contact angle increases over a time frame at the beginning of the droplet growth, followed by a constant contact angle and growing contact radius period.

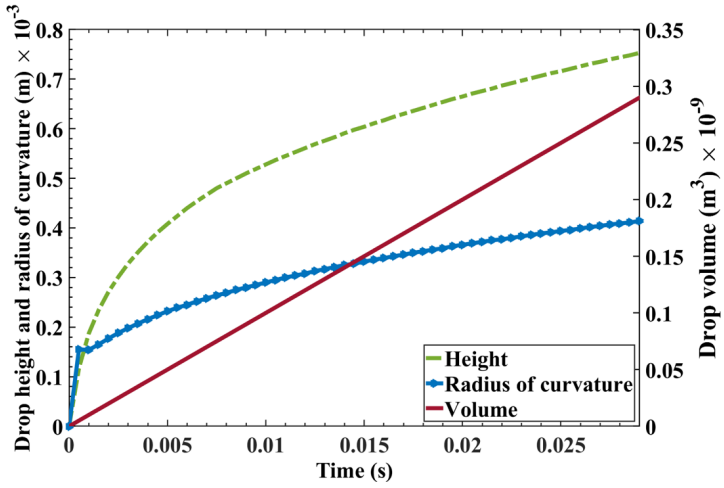

(a)

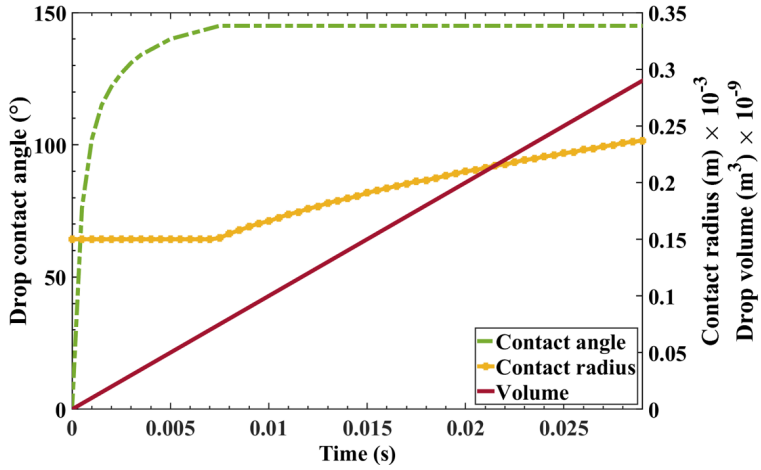

(b)

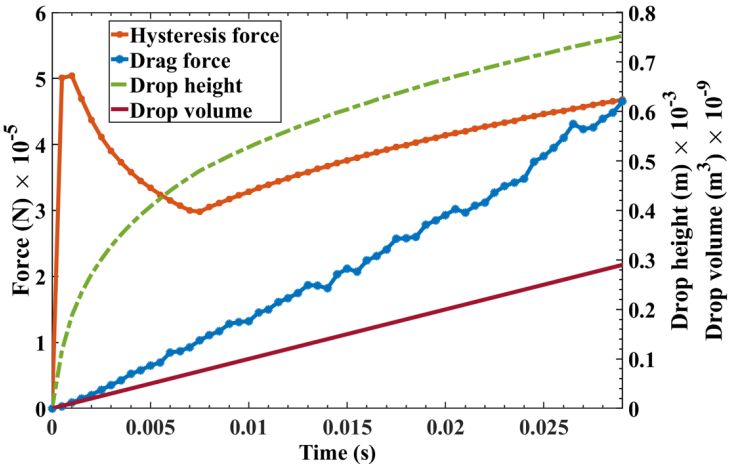

(c)

Figure 5.11: Droplet dynamics: a) variation of the droplet height, radius of curvature and volume over time, b) variation of the droplet contact angle and contact radius during the droplet growth and c) the drag and hysteresis forces variation until the droplet detaches.

If we look at Fig. 5.11c, the drag force increases almost monotonically with the droplet volume. The variation of the drag force becomes more extreme over time, although the rate at which the droplet height changes is decreasing. That means that when the droplet is larger, a change in the droplet height affects the free-flow field stronger than when the droplet is small. The hysteresis force peaks locally when the droplet contact angle reaches 90°. After that, it dips and reaches a local minimum when the droplet contact angle reaches the ultimate contact angle of the surface. By expanding the contact area of the droplet, the hysteresis force recovers and starts an upward trend.

5.2.2.4 Comparison with the ANSYS Fluent model

As mentioned before, the model introduced in this work is implemented in DuMu^x [Koch et al., 2021a], and is referred to as the "DuMu^x model" in the current section.

Figure 5.12 compares the predicted droplet detachment volume and height versus the mean free-flow velocity for DuMu^x and ANSYS Fluent model. In the DuMu^x model, we apply different descriptions of the hysteresis force, provided by Eqs. (4.44)–(4.46), to predict the detachment of the droplet and compare the results. It should be noted that in this comparison, the highest value used as maximum free-flow velocity is 30 m/s, the mean velocity is 13.95 m/s, while the lowest value is determined as the minimum velocity which detaches the droplet before reaching the upper wall of the channel. The static contact angle of the surface is 145° and the advancing and receding contact angles used in the DuMu^x model are 150° and 90°, respectively. It can be seen in Fig. 5.12a that the predicted detachment volumes by the ANSYS Fluent model and the DuMu^x model are closer at higher free-flow velocities. By decreasing the velocity, however, the difference between the results of the two models for the droplet detachment volume increases. The DuMu^x model and the ANSYS Fluent model both predict almost the same minimum free-flow velocity by which the droplet can be detached by the free flow. However, the detachment volume predicted by the ANSYS Fluent model is considerably larger than the value predicted by the DuMu^x model.

To get a better understanding, Fig. 5.12b compares the height of the droplet when it detaches, which are predicted by the DuMu^x and ANSYS Fluent model. It shows that although the different versions of the DuMu^x model and the ANSYS Fluent model predict a similar trend, the difference of the predicted values using Eq. (4.44) with the

other results is significant, especially at high free-flow velocities. Although such an observation may seem opposite to what we see in Fig. 5.12a, where the graphs converge by increasing velocity, it can be explained by looking back to Fig. 5.11a, where the variation of the droplet volume and height is compared. As explained in Section 5.2.2.3, a small change in the droplet volume when the droplet is small, can drastically affect the droplet height. At a high free-flow velocity, the droplet detaches when it is small. Thus, although the predicted values for the droplet detachment volumes differ slightly, the corresponding difference in the predicted detachment heights is noticeable. On the other hand, the predicted values by all models for the least free-flow velocity at which the droplet can be detached are close. Such behavior might be related to the deformation of the droplet which is included in the ANSYS Fluent model, whereas is not taken into account by the DuMu^x model. In fact, by lowering the free-flow velocity, the droplet can grow larger before the detachment. Therefore, the droplet experiences more deformation during its life at the interface, which enables it to gain more volume before it touches the upper wall of the channel.

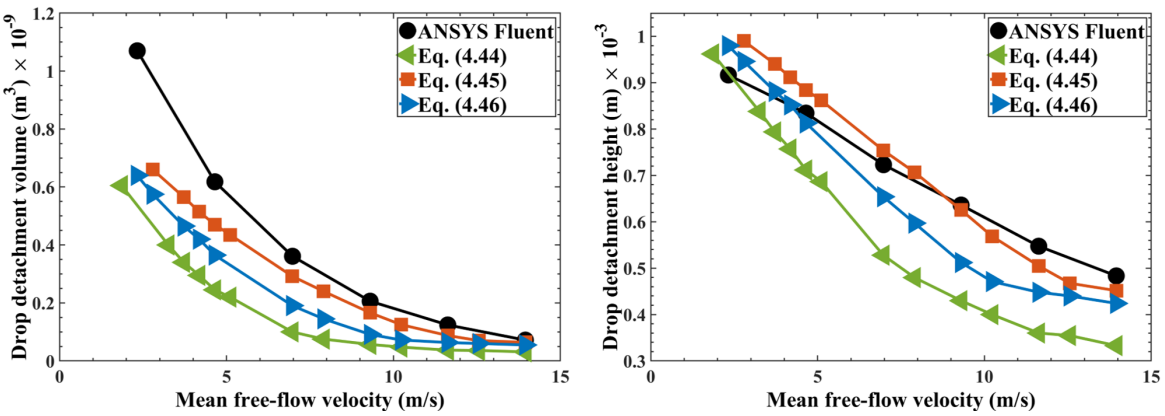

(a) (b)

Figure 5.12: Comparison between the simulation results of the DuMu^x model using various formulations for the hysteresis force and the ANSYS Fluent for a) the droplet detachment volume and b) the droplet detachment height.

To take a deeper look at the impact of the deformation, we compare the detachment values predicted by the ANSYS Fluent model and the corresponding value computed by assuming no deformation in the droplet (see Fig. 5.13). For example, in Fig. 5.13a, the detachment volumes reported for the undeformed droplet are for a droplet with the same height as the simulated droplet by the ANSYS Fluent model, if there were

no deformation. That means that the detachment height predicted by the ANSYS Fluent model is used in Eqs. (4.9) and (4.10) to calculate the droplet volume. Similarly, for the detachment height of the undeformed droplet, it would be the height of a droplet with the same detachment volume as predicted by the ANSYS Fluent model, if the deformation was not included. In other words, the detachment volume predicted by the ANSYS Fluent model is used to back calculate the detachment height by using Eqs. (4.9) and (4.10). According to Fig. 5.13a, the difference between the detachment volume for the deformed droplet, predicted by ANSYS Fluent model, and the undeformed droplet increases significantly by decreasing the free-flow velocity. The comparison of detachment height by Fig. 5.13b also shows a similar behavior. That is to say, the impact of the droplet deformation on the detachment becomes more significant when the free-flow velocity is lower. As mentioned before, when the droplet becomes larger, the change in its height has more impact on the drag force that it experiences. Therefor, the change in the height of a large droplet due to the deformation affects the detachment process more significantly than a small droplet.

One of the main differences between the DuMu^{x} model and ANSYS Fluent model is that the ANSYS Fluent model does not take the contact angle hysteresis into account. That means that the two models apply different criteria for droplet detachment. In the DuMu^{x} model, the droplet detaches when the free-flow drag force becomes larger than the hysteresis force on the contact line and consequently the droplet contact line starts to move in the drag force direction, whereas in the ANSYS Fluent model, since the contact angle hysteresis is not included, the triple contact line can move freely over the surface while the droplet is still attached to the pore. That is to say, in the ANSYS Fluent model, the surface tension force tries to hold the liquid phase together while maintaining the minimum surface area rather than keeping the droplet on the surface. That means that the droplet detachment occurs once the free-flow drag force overcomes the surface tension force and phase rapture occurs. To take the impact of contact angle hysteresis in the volume of fluid method into account, for instance, Theodorakakos et al. [2006b] took an approach to recalculate the contact angle by considering the droplet deformation due to a free flow. In another study, Fang et al. [2008] used a transient modeling approach, in which the contact angle is updated locally in each time step for each cell at the triple contact line during the simulation. Since including the contact angle hysteresis in the volume of fluid method is not in the scope of the present work, we refer to Theodorakakos et al. [2006b] and Fang et al. [2008] for more details.

To show how the maximum contact angle hysteresis impacts the detachment prediction by the DuMu^{x} model, three different values for maximum contact angle hysteresis are used in the simulations and the results are compared with the ANSYS Fluent simulations in Fig. 5.14. As expected, a droplet on the surface of the porous medium with higher ultimate contact angle hysteresis, can remain longer attached to the surface and withstand higher free-flow velocities. It can also be seen that a smaller free-flow velocity is needed to detach a droplet with lower contact angle hysteresis before it touches the upper wall of the channel. The results confirm that the contact angle hysteresis as a reflection of the solid surface properties plays a crucial role in the droplet detachment.

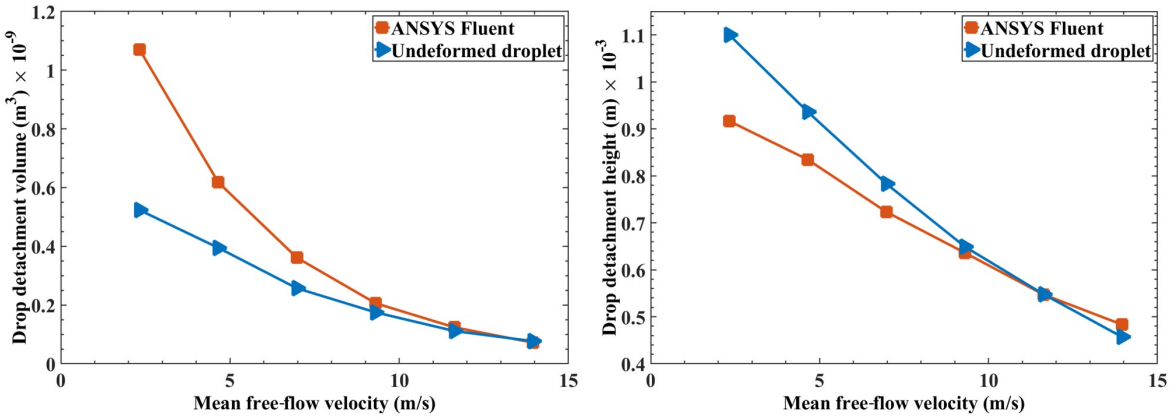

(a) (b)

Figure 5.13: Comparison between the predicted value by ANSYS Fluent model and the undeformed estimation of: a) the droplet detachment volume and b) the droplet detachment height.

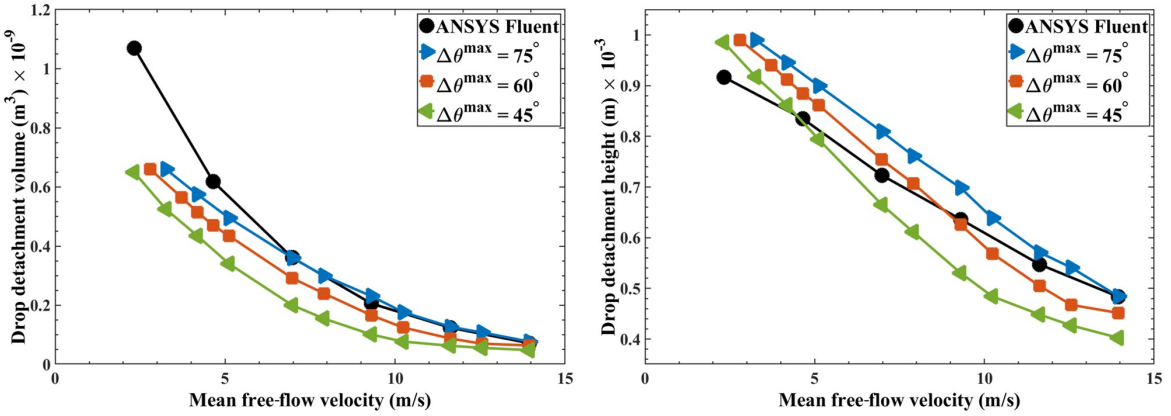

(a) (b)

Figure 5.14: Impact of the maximum contact angel hysteresis on the detachment predictions by the DuMu^x model using Eq. (4.45) to describe the contact angel hysteresis: a) drop detachment volume and b) drop detachment height.

5.2.2.5 Comparison with analytical and semi-analytical derivations for the droplet detachment

There are several analytic and semi-analytical approaches describing the detachment behavior of liquid water droplets from hydrophobic surfaces in the literature [Chen et al., 2005, Kumbur et al., 2006, Cho et al., 2012, Hao and Cheng, 2010]. Chen et al. [2005] developed an analytical relation to predict the detachment of a droplet using a two-dimensional (2D) description of the force balance around the droplet on a solid surface influenced by surrounding gas flow. They used Eq. (4.45) to compute the hysteresis force. The 2D approximation represents an infinitely wide channel (parallel plates) but also an infinitely wide droplet (deformed cylindrical shape), such that shear forces at the sides of the droplet are not included. Except using Eq. (4.44), Kumbur et al. [2006] used an approach similar to Chen et al. [2005] to predict the detachment of the droplet. Cho et al. [2012] extended the concept presented by Chen et al. [2005] by computing the drag force employing a drag coefficient derived from numerical simulations. Figure 5.15 compares the separation line generated by the analytical/empirical approaches, the ANSYS Fluent model and the DuMu^x model. In this figure, the dimensionless drop height is the ratio of the drop height to the channel height. The static contact angle and contact angle hysteresis used in this section are 145° and 60°, respectively.

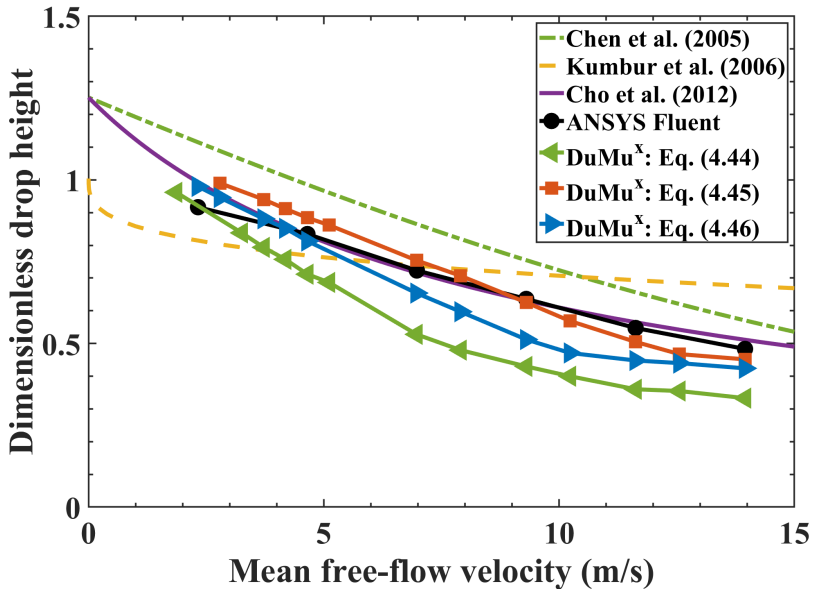

Figure 5.15: Comparison of separation lines predicted by analytical/empirical approaches, the ANSYS Fluent and the DuMu^x model using various description of the hysteresis force.

The separation line generated by Cho et al. [2012] derivation shows the best agreement with the DuMu^x and ANSYS Fluent model. However, it does not include the possible contact of the droplet with the top wall of the channel, such that it predicts a dimensionless drop height larger than one for low free-flow velocities. The separation line generated by Chen et al. [2005] derivation has the same issue at low velocities. Although the separation line predicted by Kumbur et al. [2006] approach tends to a dimensionless drop height of one at low velocities, it suffers from lack of accuracy in prediction of the droplet detachment. The disability of the analytical approaches to generate a reliable separation line might stem from their two-dimensional derivation, which Cho et al. [2012] tried to improve by using numerical simulations in a three-dimensional channel. Another point is that the DuMu^x and ANSYS Fluent models show results for a channel width of $W_{\text{channel}} = 1.35$ mm and height $H_{\text{channel}} = 1$ mm (aspect ratio ≈ 0.74), which is common in modern proton-exchange membrane fuel cells. Other studies, however, used channels with higher aspect ratios for fitting and validating the data.

5.2.3 Droplets interactions at the interface

Thus far, we have discussed the detachment of a single droplet at the interface between a free-flow domain and a porous medium. In this section, we look at the impact of a neighboring droplet on the detachment of a droplet at the interface.

5.2.3.1 Simulation setup

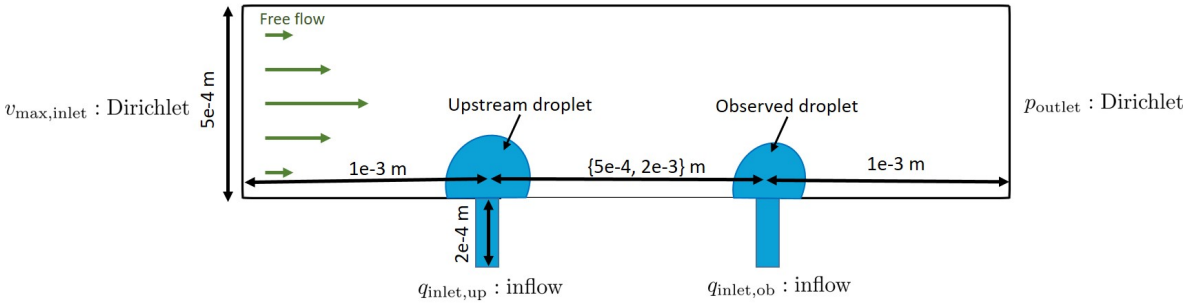

Figure 5.16: The simulation setup used to analyze the interactions between two neighboring droplets at the interface.

Figure 5.16 shows the simulation setup used to analyze the impact of an upstream droplet on the detachment of a droplet. In this setup, two pores are connected to the bottom wall of a free-flow channel. Water is injected to the inlet of the pores with different injection rates. Gas (air) flows into the free-flow channel with a fully developed laminar velocity profile, and at the channel outlet, pressure is fixed. We examine the impact of injection rate to the throats, distance between the pores at the interface, and free-flow velocity on the process.

5.2.3.2 Results

We compare the droplet detachment volume including the impact of the upstream droplet, $V_{\text{detachment, two droplets}}$, with the detachment volume of the observed droplet when it is the only droplet forming at the interface, $V_{\text{detachment, single droplet}}$ and define the change in the detachment volume as:

$$\Delta V_{\text{detachment}} = 100 \times \frac{V_{\text{detachment, two droplets}} - V_{\text{detachment, single droplet}}}{V_{\text{detachment, single droplet}}}. \tag{5.4}$$

To analyze the impact of throat injection rate, we use the ratio of the injection rate of the upstream droplet, $q_{\text{inlet,up}}$, to the injection rate of the (observed) droplet, $q_{\text{inlet,ob}}$. We define the upstream injection rate ratio as $q^*_{\text{inlet,up}} = q_{\text{inlet,up}}/q_{\text{inlet,ob}}$.

Figures 5.17a and 5.17b show the change in $\Delta V_{\text{detachment}}$ with $q^*_{\text{inlet,up}}$ and the distance between the droplets for the free-flow velocities of 5 m/s and 10 m/s respectively. In Fig. 5.17a, increasing the injection rate of the upstream droplet leads to longer delays in the droplet detachment when the distance between the two droplets is 0.5 mm whereas in cases where the distance between the droplets is 2 mm, the upstream droplet with different injection rates has no considerable impact on the droplet detachment. Figure 5.17b, however, shows that when the free-flow velocity is 10 m/s, the influence of the upstream droplet on the droplet detachment is significant, whether the distance between the droplets 0.5 mm or 2 mm is. In this figure, the delay in the droplet detachment increases and peaks by increasing the upstream injection rate and then decreases. Such a peak occurs earlier for a shorter distance.

Figures 5.18a and 5.18b compare the change in the detachment volume by free-flow velocity for cases where the distance between the droplets are 0.5 mm and 2 mm, respectively.

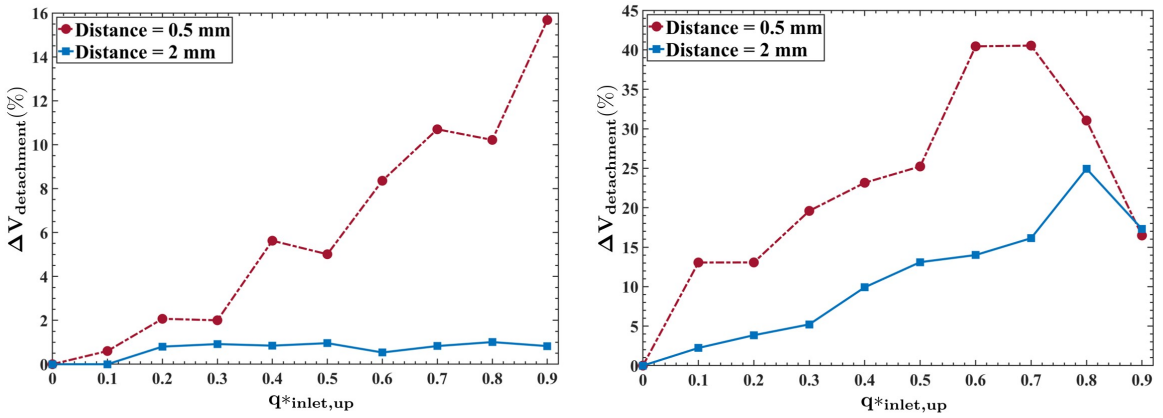

(a) (b)

Figure 5.17: Impact of injection rate ratio of the upstream droplet on the detachment volume of the observed droplet when the maximum free-flow inlet velocity is a) 5 m/s, and b) 10 m/s.

Depending on the free-flow velocity and the distance between the droplets, both neighboring droplets might affect the free-flow field which the other droplet experiences. The

upstream droplet acts similar to a shield for the observed droplet by reducing the drag force acting on it. Such an impact is visualized by Fig. 5.19. This figure shows the impact of the droplets on the free-flow velocity field shortly before the observed droplet detaches when the injection rate ratio of the upstream droplet is 0.5 and the maximum free-flow inlet velocity is 10 m/s.

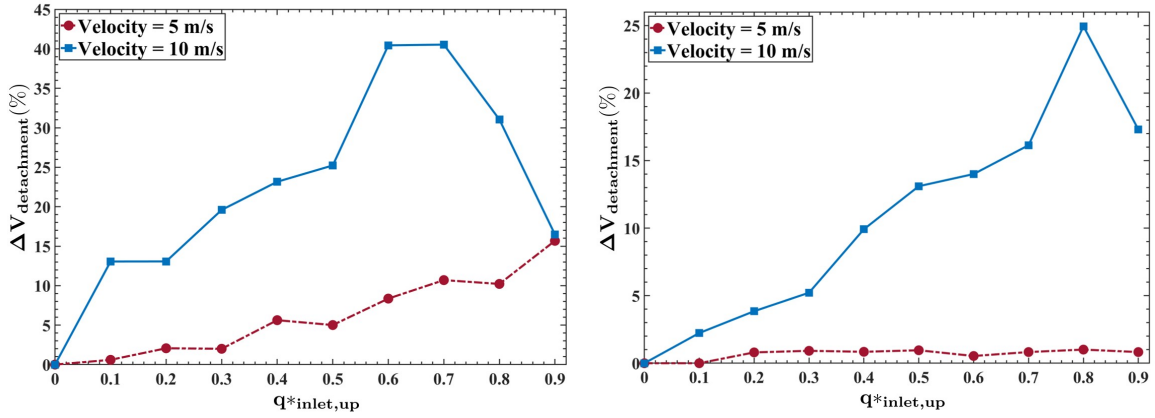

Figure 5.18: Impact of injection rate ratio of the upstream droplet on the detachment volume of the observed droplet when the distance between the droplets is a) 0.5 mm, and b) 2 mm.

Having the observed droplet at the downstream could advance the detachment of the upstream droplet by increasing the flow recirculation at the back of it. After the upstream droplet detaches, the (observed) droplet detaches due to an increase in the drag force acting on it. As an instance, Fig. 5.20a shows the impact of the two droplets on the free-flow velocity field in the channel shortly before the upstream droplet detaches. Figure 5.20b illustrates the free-flow velocity field shortly before the observed droplet detaches. As can be seen, due to the early detachment of the upstream droplet, the reemerged upstream droplet is not large enough to delay the detachment of the observed droplet.

The interactions between two neighboring droplets at the interface are more significant when the droplets are larger and closer together, which might lead to more delay in the detachment of the observed droplet or/and earlier detachment of the upstream droplet.

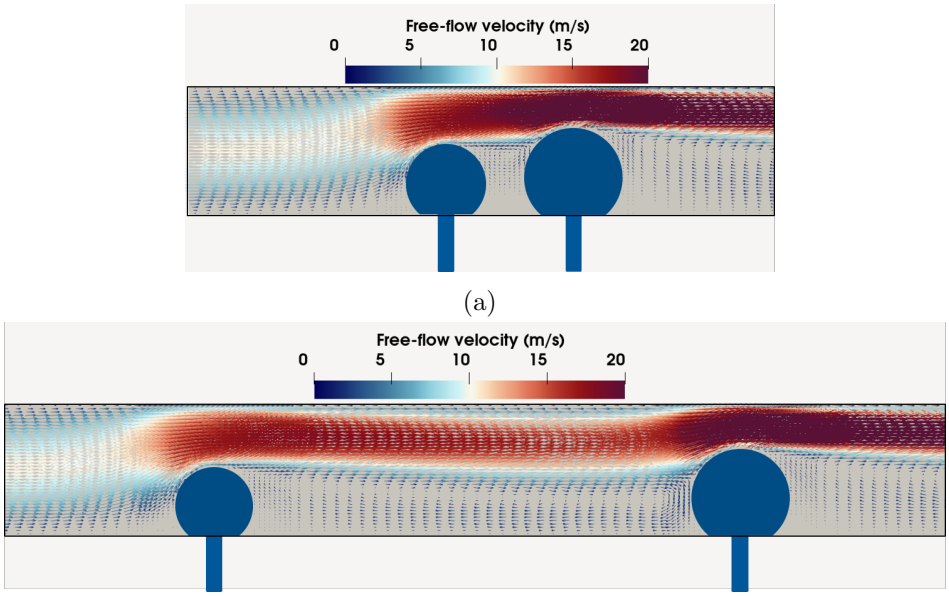

(a)

(b)

Figure 5.19: Impact of two droplets at the interface on the free-flow velocity field when the distance between the droplets is a) 0.5 mm, and b) 2 mm and the maximum free-flow inlet velocity is 5 m/s.

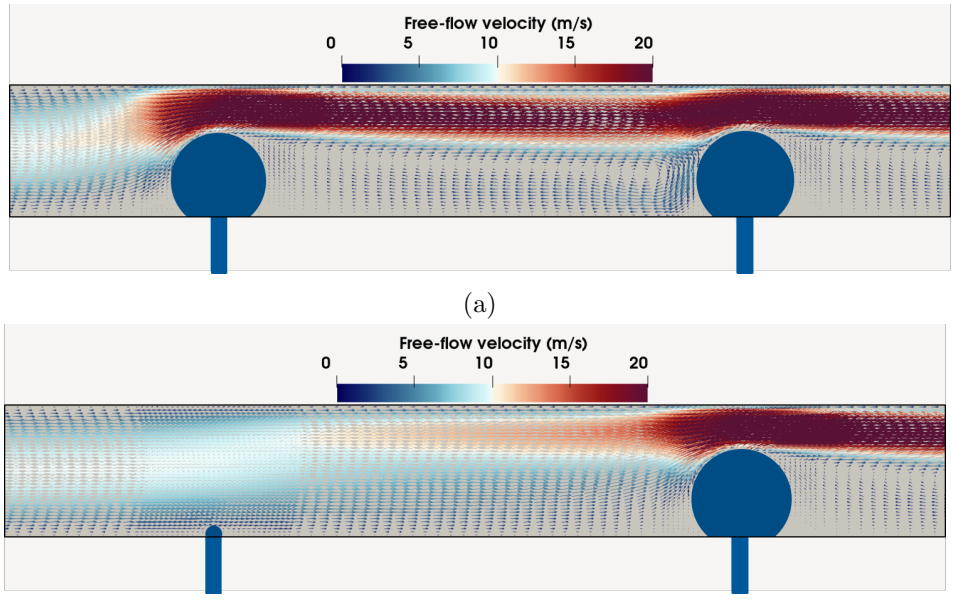

(a)

(b)

Figure 5.20: Free-flow velocity field a) shortly before the upstream droplet detaches and b) shortly before the observed droplet detaches for a case in which the maximum free-flow inlet velocity is 10 m/s, the injection rate ratio of the upstream droplet is 0.9, and the distance between the droplets is 2 mm.

5.2.4 Free-flow–droplet–pore-network system[‡]

To show the application of the model in modeling of formation, growth, and detachment of multiple droplets at the interface, we use a setup shown in Fig. 5.21. In this setup, a two-dimensional channel with dimensions of 10 mm × 1 mm (length × height) is used as the free-flow domain. A pore network, as the porous medium, is connected to the bottom wall of the channel. The pore network consists of 142 pore bodies connected by 190 pore throats to each other. The radii of the pore bodies vary between 0.019 to 0.063 mm. The pore throats have radii from 0.014 to 0.04 mm and lengths from 0.02 to 0.4 mm. The free-flow channel is initially filled with air and the pore network is initially fully saturated with water. Air flows to the channel with maximum velocity of 15 m/s in a fully developed laminar profile and the outlet of the channel is exposed to the atmospheric pressure. Water is injected to the inlet pores of the network with the rate of 5×10^{-7} kg/s. The droplets form and grow onto pore bodies with various sizes at the interface. Figure 5.22 shows a snapshot of such a process, where the multiple droplets formed at the interface influence the free-flow velocity field.

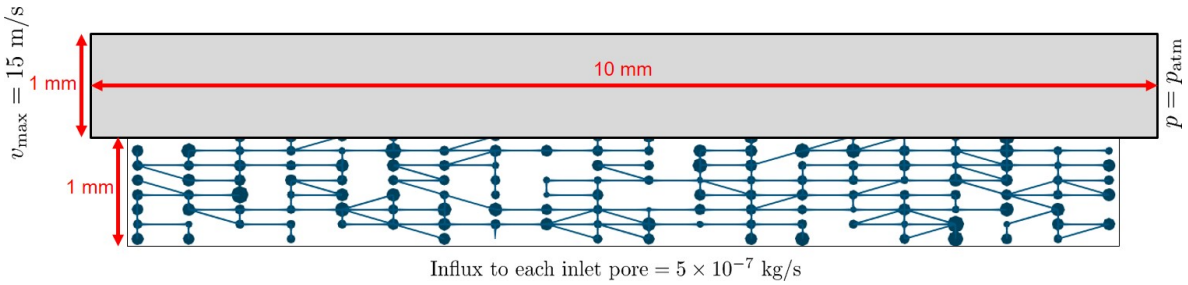

Figure 5.21: Simulation of formation and growth of multiple droplets at the interface of a coupled free-flow–pore-network system: a) the simulation setup, b) formation of multiple droplets at the interface and their impacts on the velocity field of the free flow.

[‡]This section was previously published by Transport in Porous Media (Springer) [Veyskarami et al., 2023].

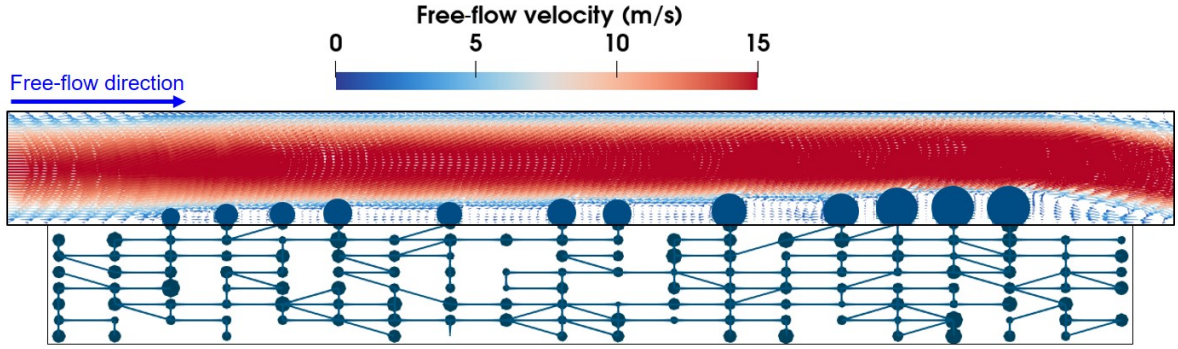

Figure 5.22: Simulation of formation and growth of multiple droplets at the interface of a coupled free-flow–pore-network system: a) the simulation setup, b) formation of multiple droplets at the interface and their impacts on the velocity field of the free flow.

6 Results and discussions for droplet evaporation at the interface *

In this chapter, we first look into a non-isothermal compositional coupled free-flow–porous medium system using a small pore network in which drainage occurs in the network and then a droplet forms at the interface. After that, we compare the simulation results for droplet evaporation with experimental data. Then, we analyze the impact of various factors on the evaporation of a droplet at the free-flow–porous medium interface. Furthermore, we analyze the impact of evaporation on the droplet detachment. At the end, we present a showcase consists of a free flow domain coupled with a pore network to show the application of the developed model in describing multiple droplets formation and evaporation.

6.1 Free-flow–porous medium interactions in a non-isothermal compositional system: Porous medium drainage, droplet formation and evaporation

This section focuses on the mass, momentum, and energy interactions between a single-phase two-component gaseous free flow and a two-phase two-component porous medium. We discuss the impacts of phenomena occurring in a simple porous medium during a drainage process and the interactions with the free flow, as well as droplet formation on the pressure, temperature, and vapor mass fraction of the interface pore body.

*Parts of this chapter have been submitted for publication to Transport in Porous Media (Springer).

6.1.1 Simulation setup

Figure 6.1 illustrates the simulation setup that we used in this analysis. The simulation setup consists of a free-flow channel connected to a small porous medium, composed of three pore bodies and two pore throats. Both domains are initially completely saturated with dry gas (air), i.e., with zero relative humidity. Dry air flows into the channel at the inlet with the maximum velocity of 5 m/s and the temperature of 298.15 K. Liquid (water) is injected to the inlet of the pore network with the rate of 1×10^{-5} kg/s and the temperature of 288.15 K. Since the porous medium is hydrophobic, the water phase is the non-wetting phase and displaces the air, i.e., wetting phase, in a drainage process. After water fills the interface pore body, a droplet forms at the interface.

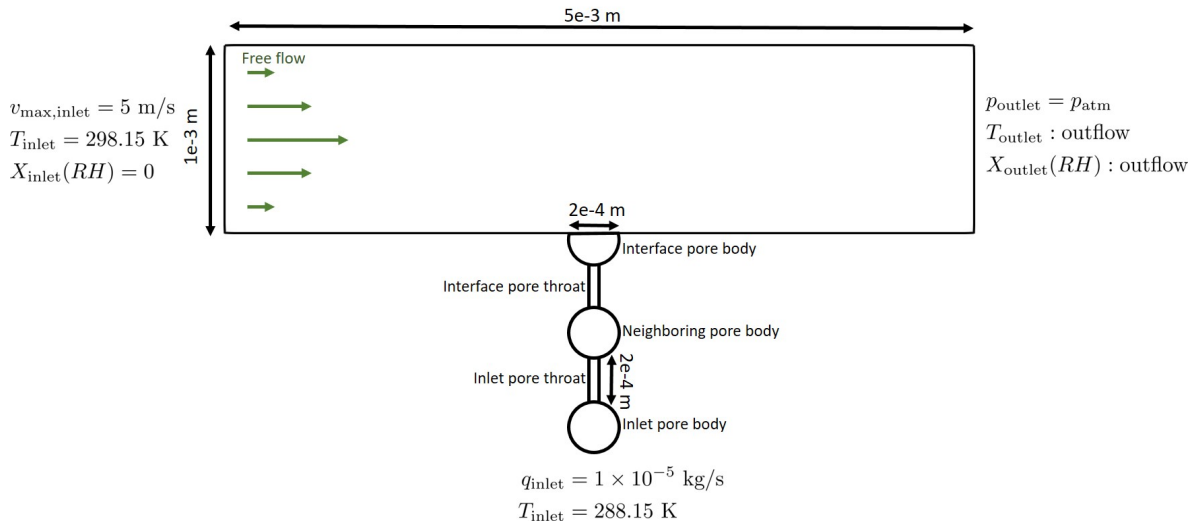

Figure 6.1: The simulation setup used to analyze the free-flow–porous medium interactions in a non-isothermal compositional system.

6.1.2 Results

Figure 6.2 shows the variation of the interface pore pressure versus time. Since the interface pore body is initially filled with gas, it interacts with the free flow directly and its pressure is equal to the free-flow pressure at the interface, which is almost constant (time period of 0 to 6×10^{-3} s in Fig. 6.2). Due to invasion of the interface pore throat, water flows to the interface pore body and the saturation of the water, i.e., non-wetting phase, starts to increase, which raises the capillary pressure in the

pore body and a jump in the pore pressure (the first jump in the pressure shown in Fig. 6.2). In a short time, water fills the pore body completely and a droplet emerges at the interface. At this time, the interface pore body is covered by a droplet and it interacts with the free flow indirectly through the droplet. Formation of the droplet causes the second sharp increase in the pore pressure, which is followed by gradual reduction of the pressure due to droplet growth and the consequent decrease in the droplet capillary pressure.

In Figs. 6.3a and 6.3b, it is shown how the temperature and vapor mass fraction of the interface pore body changes during the drainage of the porous medium, followed by the droplet formation at the interface. As Fig. 6.3a shows, having initially a temperature of 288.15 K, the interface pore body becomes warmer and its temperature increases due to direct interaction with the free flow with the inlet temperature of 298.15 K in a short time. Then, due to the impact of the neighboring pore body with lower temperature, the interface pore body temperature slightly decreases and levels off for a period. Once water invasion occurs in the inlet pore throat, which causes falling of the temperature in the neighboring pore body because of water flow with the temperature of 288.15 K, the interface pore body also experiences a decrease in the temperature as a consequence of the water front advancement toward the interface in the porous medium. Remaining almost constant over a period of time, the temperature of the interface pore body falls steeply to near 288.15 K due to the water invasion in the interface pore throat, i.e., water flow to the interface pore body. After the interface pore body is filled with water, the droplet forms at the interface and the pore temperature remains almost constant and equal to 288.15 K.

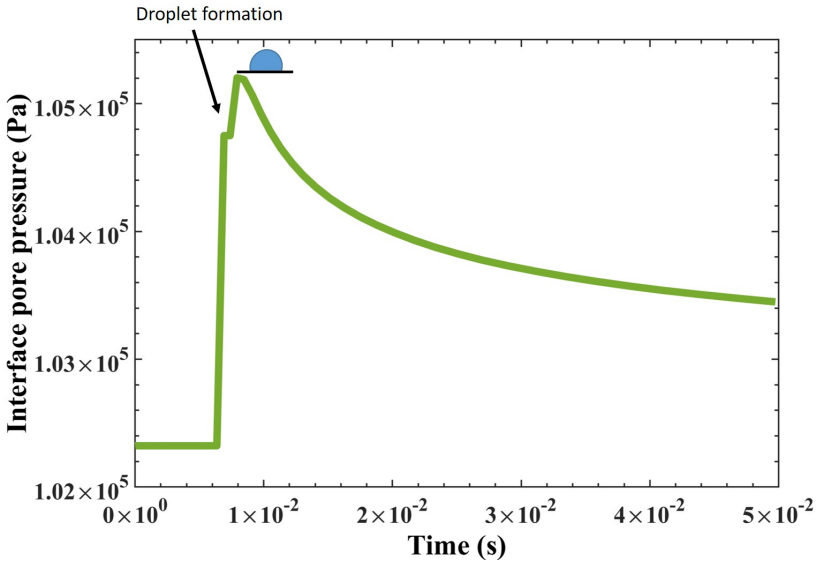

Figure 6.2: Variation of the interface pore pressure during the drainage of the porous medium and droplet formation.

Looking at Fig. 6.3b, vapor mass fraction (concentration) in the interface pore body starts gradually increasing from zero, i.e., dry air, as water comes to existence in the system due to injection into the inlet pore body and the advective and diffusive vapor transport between the pore bodies. Water invasion in the inlet pore throat and flow of water to the neighboring pore body results in a fast increase in the vapor concentration at the interface pore body related to the moving of water front toward the interface. By water invasion in the interface pore throat, a two-phase flow is established in the interface pore body and the vapor mass fraction increases to the equilibrium vapor mass fraction. Further water flow to the interface pore body raises the water saturation until the pore body is filled with water and the droplet forms at the interface. It should be noted that since in our numerical approach to solve the system, we don't introduce a new degree of freedom for the droplet at the interface and we use the degree of freedom of the interface pore body for the whole droplet and the pore body, the vapor mass fraction of the interface pore body after droplet formation is in fact the mass fraction at the droplet surface.

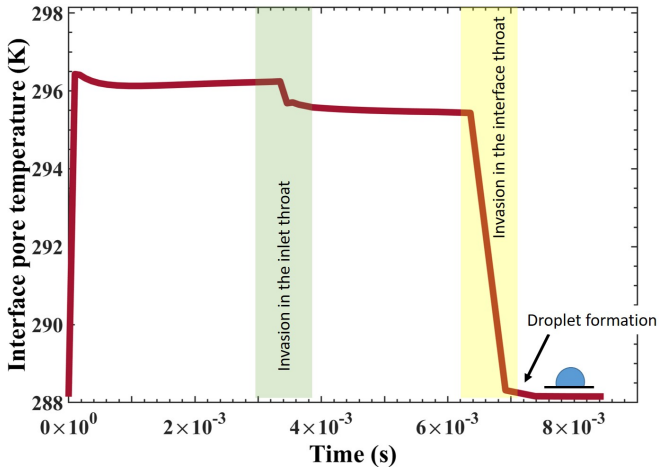

(a)

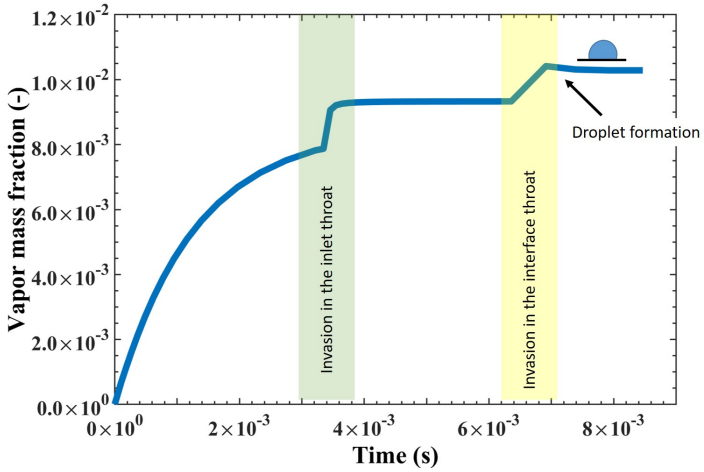

(b)

Figure 6.3: Variation of a) the interface pore temperature and b) vapor mass fraction (concentration) during the drainage of the porous medium and droplet formation.

Figure 6.4 shows the temperature field in the system before and after droplet formation at the interface. Figure 6.4a presents a snapshot in time when the inlet throat is invaded, i.e., the inlet and neighboring pore bodies contain water. It is evident that the pore body at the interface has a temperature higher than the other pore bodies but lower than the free flow. In the free flow, the cooling effect of the porous medium slightly decreases the temperature at the interface and its downstream. Figure 6.4b shows a snapshot of when a droplet formed at the interface. Conductive and diffusive heat transfer between the droplet and the free flow leads to cooling of the free flow at the

vicinity of the droplet surface. Furthermore, energy transfer due to the free flow in the flow direction in the form of heat convection influence the temperature field in the channel. In Fig. 6.4b, the cooling effect of the droplet is significant, especially near the triple contact point upstream of the droplet, where fluid circulates in a low velocity and in the wake region downstream of the droplet, in which flow circulation occurs.

(a) (b)

Figure 6.4: Temperature field: a) before droplet formation and b) after droplet formation.

Figure 6.5 shows vapor mass fraction (concentration) distribution in the system before and after droplet formation. It can be seen that the vapor distribution and the temperature field are similar and the interactions between the domains in terms of vapor concentration can be described using the same reasoning as for the temperature field. Before the formation of the droplet, free-flow vapor concentration increases due to the mass exchange with the interface pore body, which is connected to the neighboring pore body containing two phases in thermodynamic equilibrium. After the droplet forms, evaporation from the surface of the droplet increases the vapor concentration around the droplet through vapor diffusion. Advective vapor transfer by the free flow in the flow direction results in unsymmetrical vapor distribution upstream and downstream of the droplet.

(a) (b)

Figure 6.5: Distribution of vapor mass fraction: a) before droplet formation and b) after droplet formation.

6.2 Droplet evaporation: Comparison with experimental data

In this section, we compare the simulation results of droplet evaporation with experimental data provided by Bansal et al. [2017].

Bansal et al. [2017] examined the impact of confinement on the evaporation of a sessile droplet. Their results show that evaporation time increases in a channel due to accumulation of vapor around the droplet. The impact of vapor accumulation becomes more significant by increasing the channel length. Bansal et al. [2017] characterized this effect by introducing a vapor accumulation length scale, which determines how far from the droplet the vapor concentration reduces to the ambient concentration.

We first describe the simulation setup used for the comparison. Then, we present the comparison of simulation and experimental results for evaporation of a single sessile droplet in a channel.

6.2.1 Simulation setup

The setup used in the experiment is thoroughly discussed in Bansal et al. [2017]. Thus, we only focus on the simulation setup in this part. The simulation setup consists of a two-dimensional channel with the height of 1.2×10^{-3} m. The channel length, L, varies

from 2.55×10^{-3} m to 1.765×10^{-2} m. It should be noted that the channel length used here is determined based on the vapor accumulation length-scale introduced by Bansal et al. [2017], which is a length over which the vapor concentration varies from the concentration at the droplet surface to the ambient concentration. We apply pressure of 1 atm, temperature of 298.15 K, and relative humidity of 45% to the channel inlet and outlet (see Fig. 6.6). Using a pore connected to the bottom wall of the channel, a droplet with the volume of 1.5×10^{-9} m^3 is formed and then evaporates until it disappears.

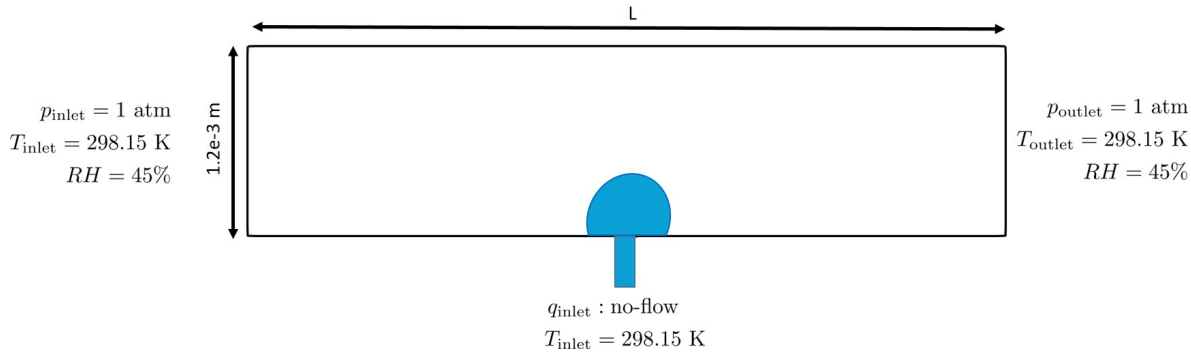

Figure 6.6: Simulation setup and boundary conditions used in comparison with experimental data for droplet evaporation. "L" is the channel length, which varies in each simulation to examine the impact of channel length on droplet evaporation.

6.2.2 Results

Figure 6.7 shows the impact of channel length on the evaporation time and compares the simulation results and experimental data provided by Bansal et al. [2017] for a single droplet evaporating in a channel. According to the results, there is a good match between the simulation and experimental data and our model is able to predict the impact of the channel length on the evaporation time of the droplet.

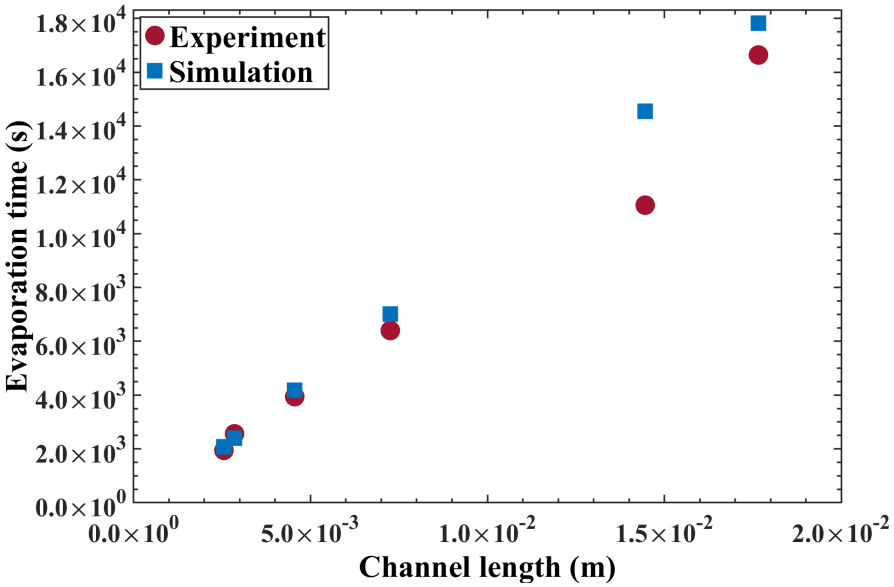

Figure 6.7: Comparison of simulation results with the experimental data given in Bansal et al. [2017] for impact of channel length on the evaporation of a single droplet confined in a channel.

Having validated our concept for droplet evaporation through comparison with experimental data, we employ our model for further analysis in the next section.

6.3 Droplet evaporation analysis

In this section, we use the developed model to simulate the evaporation of a single droplet formed at the interface between a free flow and a porous medium. At first, we describe the setup that is used for the simulations and then, we analyze the impact of free-flow and porous medium properties on the droplet evaporation.

6.3.1 Simulation setup

To simulate a single droplet evaporation, we use a setup shown in Fig. 6.8. The setup is composed of a two-dimensional free-flow channel and a simple porous medium, which consists of two pore bodies connected by a pore throat.

The channel is fully filled with gas (air) initially. At the inlet, gas flows into the channel with a fully developed laminar velocity profile. Dirichlet boundary conditions are applied at the inlet for gas velocity, temperature, and mole fraction (relative humidity). At the outlet of the channel, a constant pressure is applied, and outflow boundary conditions are used for temperature and mole fraction.

The porous medium is fully saturated with water initially. At the inlet pore body, Dirichlet boundary conditions are applied for temperature and mole fraction of the components. Water is injected to the inlet pore for a short time, ϵ, such that a droplet with an intended volume is formed at the bottom wall of the channel. Then, the injection stops and the droplet starts to shrink due to evaporation until it vanishes from the surface. It should be noted that in comparison to the whole time of the evaporation process, the injection time is so small that droplet evaporation during injection is negligible.

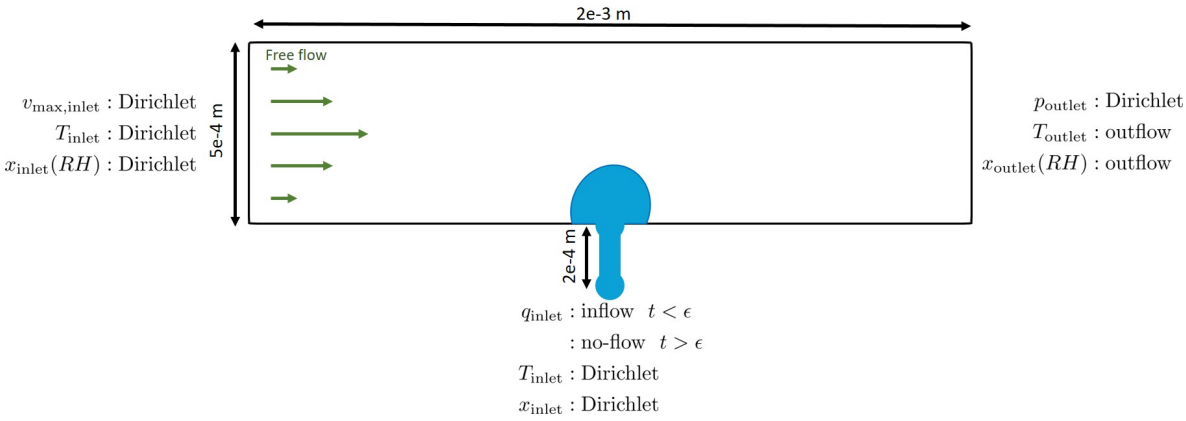

Figure 6.8: The simulation setup used for droplet evaporation analysis: Dimensions and boundary conditions.

6.3.2 Grid resolution in the free-flow domain

To find the suitable grid resolution in the free-flow domain such that it preserves accuracy but at the same time prevents high computational cost, we apply three different grid resolutions to the channel. In all cases, a refinement algorithm is employed to have finer grids around the droplet (see Fig. 6.9). The area in the middle of the channel with smaller grid cells is where the droplet forms. For this area, 3050, 1240, and 750 grid cells are used in the fine, medium, and course resolutions respectively.

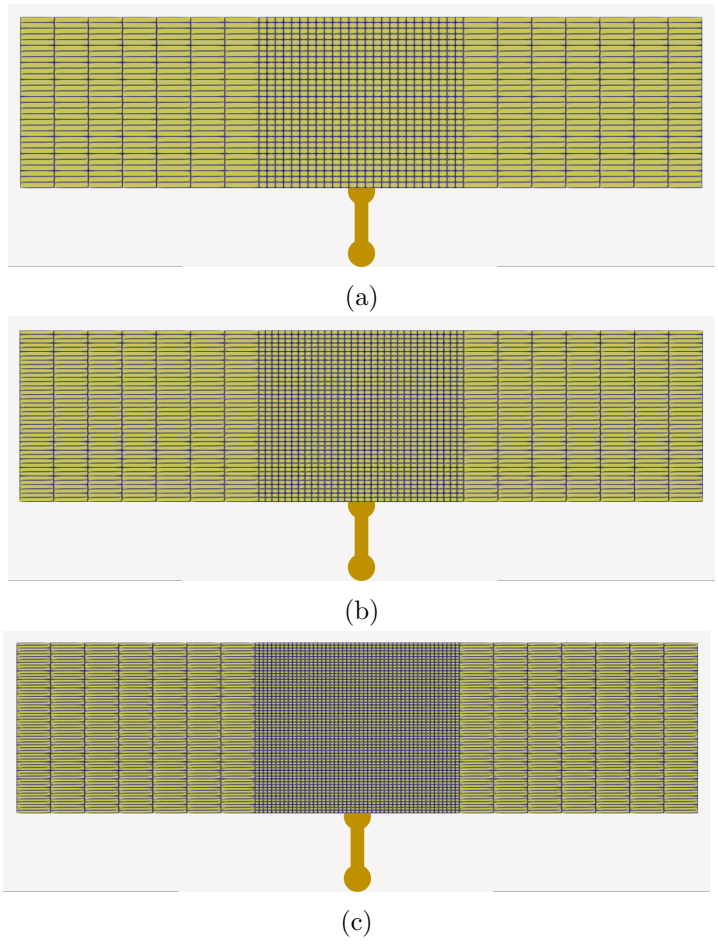

Figure 6.9: Three grid configurations used to analyze the impact of the grid resolution: a) the course grid, b) the medium grid and c) the fine grid resolution.

Figure 6.10 shows the variation of droplet volume versus time as a result of evaporation for the three grid resolutions. Although a slight difference between the results can be observed, refining the mesh does not have a considerable impact on the evaporation rate for the range of grid resolution used in this analysis. However, it is expected that using a coarser grid than what is used here makes the effect of the grid resolution on the simulation results more visible. Since, the main purpose of this section is to find a proper grid resolution to conduct the simulation, we use the medium grid resolution which gives results almost similar to the fine grid resolution and also reduces the simulation time comparing to using the fine grid resolution.

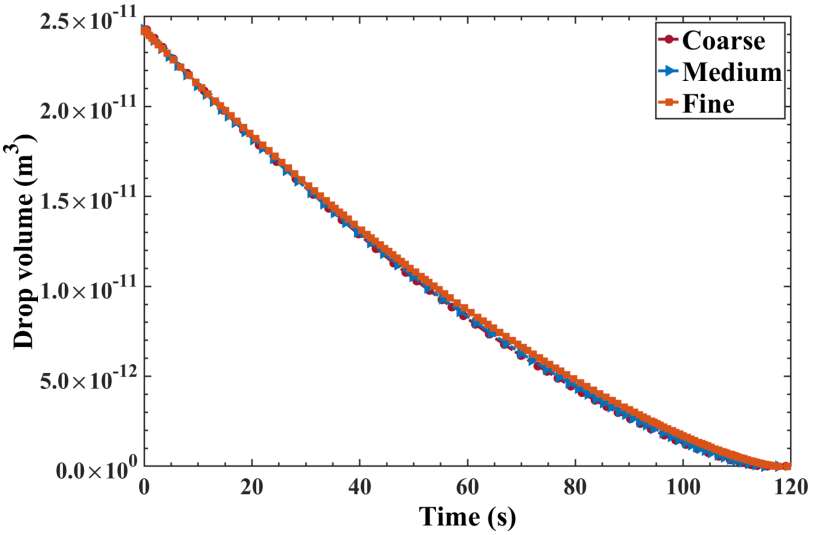

Figure 6.10: Impact of grid resolution on the simulation of droplet evaporation.

6.3.3 Impact of pore body radius (evaporation mode)

Two main modes of droplet evaporation are: constant contact angle (CCA) and constant contact radius (CCR). In this section, we analyze the impact of the evaporation mode on the droplet evaporation. Since the pore body radius is a factor that determines the switch of the droplet evaporation mode, using different pore radii varies the duration of the evaporation mode. Having a droplet with a specific volume, a small pore body connected to the droplet means mainly following the constant contact angle mode during the evaporation. That is because the evaporation of a droplet with a contact radius greater than the pore body radius starts in the constant contact angle mode. The evaporation mode switches to the constant contact radius mode once the contact radius of the droplet reduces to the pore body radius. Therefore, the smaller the pore body radius, the later the switch of evaporation mode occurs. On the contrary, a larger pore body radius gives a greater weight to the constant contact radius mode in the evaporation process. In our analysis, we use two different radii for the pore connected to the evaporative droplet: a radius of 1×10^{-4} m and another radius of 5×10^{-5} m. Figure 6.11 depicts the modes of evaporation for the two pore body radii in terms of the contact angle and contact radius variation, as well as the change in the volume of the droplets in the two cases. In this figure, the mode of evaporation is indicated using CCA (constant contact angle) or CCR (constant contact radius) mode.

Figure 6.12a shows that the evaporation occurs slightly faster when the pore body radius is smaller, i.e., the constant contact angle mode is the main evaporation mode. In the case that constant contact radius is the dominant mode, the contact angle of the droplet starts to decrease earlier, which leads to reduction of the droplet surface area. That results in a slightly slower evaporation process for the constant contact radius mode. This effect can be seen in Fig. 6.12b, where the change of droplet surface area versus the droplet volume for each evaporation mode is shown.

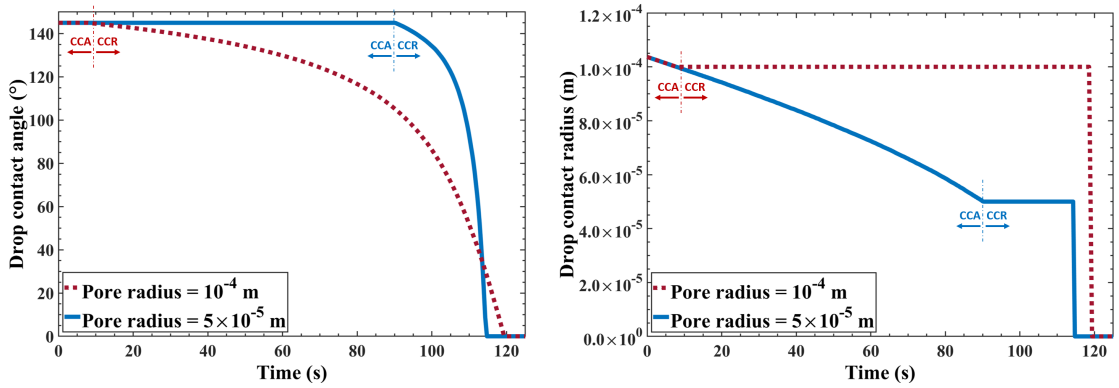

(a) (b)

Figure 6.11: Variation of a) droplet contact angle and b) droplet contact radius over time during droplet evaporation for two pore body radii.

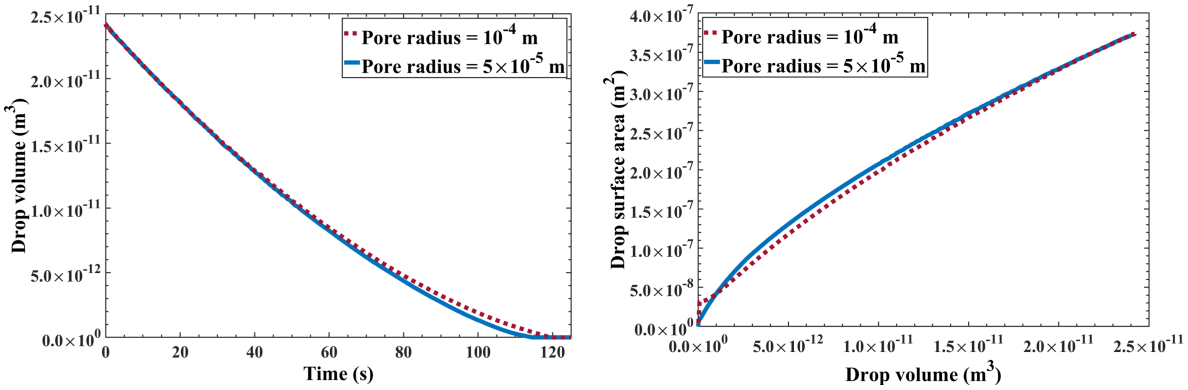

(a) (b)

Figure 6.12: Variation of a) droplet volume over time, and b) droplet surface area versus droplet volume during droplet evaporation for two pore body radii.

6.3.4 Impact of free-flow relative humidity

As the evaporation from the surface of the droplet is diffusion-driven, the relative humidity of the free flow is one of the key parameters affecting the evaporation rate. Figure 6.13 shows how relative humidity of the free flow influences the droplet evaporation. In Fig. 6.13a, the average evaporation rate versus the relative humidity (RH), which is applied to the inlet of the free-flow channel as a boundary condition, and the pore body temperature is depicted. The average evaporation rate is calculated by dividing the initial droplet mass to the total time of the droplet evaporation, i.e., how long it takes for a droplet to completely evaporate. Expectedly, increasing the relative humidity of the free flow decreases the average evaporation rate. It can be seen that the average evaporation rate decreases almost linearly with the relative humidity for each free-flow temperature. Figure 6.13b shows the evaporation rate versus time for different relative humidities for a case that the pore body temperature is 298.15 K. The evaporation rate reported in this figure is the rate of change in the droplet mass due to the evaporation. The evaporation rate follows a downward trend with time for all cases, which could be due to the shrinkage of the droplets with time, which reduces the evaporation rate. The change in the evaporation rate varies over the life of the droplet. Each graph experiences a major increase in slope as it approaches to the end, which corresponds to the switch in the evaporation from constant contact angle to constant contact radius mode. After the switch, the evaporation rate falls faster than before, i.e., the evaporation occurs slower. In addition, when a droplet shrinks, its surface moves toward the bottom wall of the free-flow channel. Thus, the local velocity of the free-flow surrounding the droplet decreases, which leads to a further decrease in the evaporation rate. The impact of the free-flow velocity on the droplet evaporation is examined in Section 6.3.6. Figure 6.13c shows variation of the droplet volume due to the evaporation versus time for three different values of relative humidity. This figure is for a case where the pore body temperature is 298.15 K.

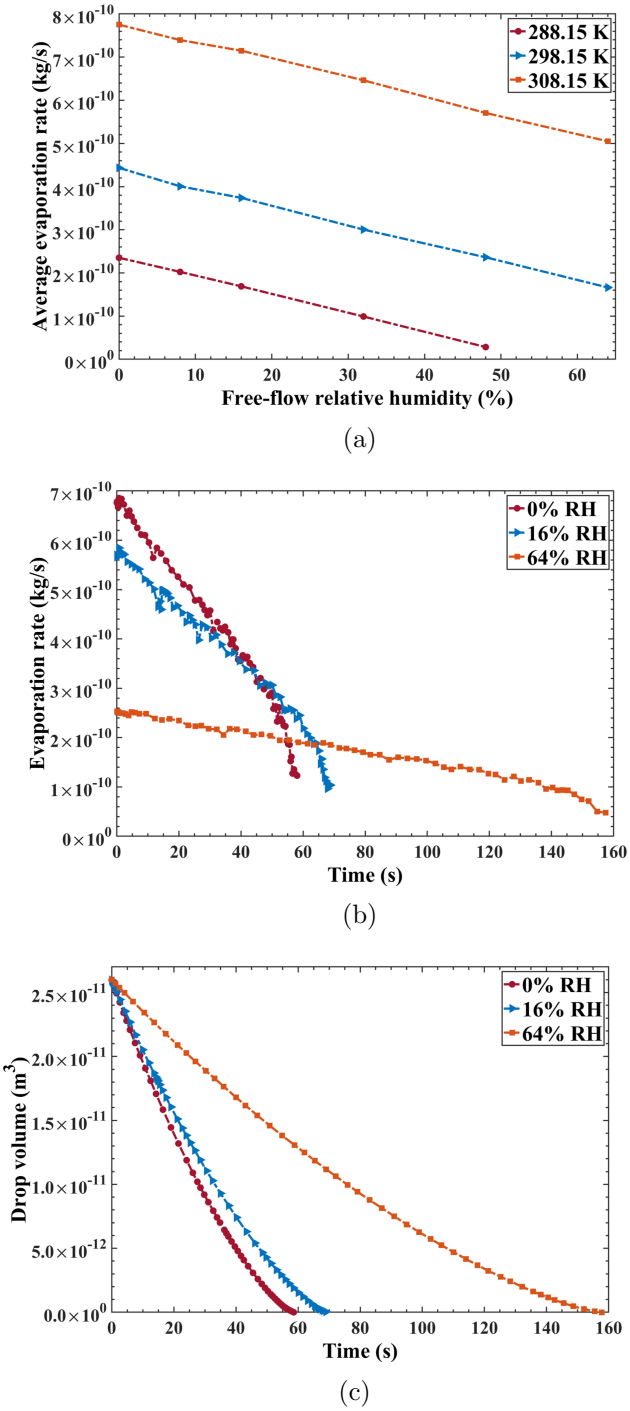

Figure 6.13: Impact of free-flow relative humidity on droplet evaporation: a) average evaporation rate, b) evaporation rate for a case where the pore and free-flow inlet temperature are 298.15 K and c) droplet volume variation over time for a case where the pore and free-flow inlet temperature are 298.15 K.

6.3.5 Impact of free-flow temperature

Figure 6.14 shows the change of droplet volume due to evaporation in various inlet free-flow temperatures and relative humidities. It should be noted that the inlet pore body temperature is the same in all cases and equal to 298.15 K. According to Fig. 6.14a, which shows the results for a setup with inlet relative humidity of 0%, the free-flow temperature has no impact on the droplet evaporation. Two reasons could be given for such a behavior. The first reason could be even energy distribution over the droplet and the connected pore body, i.e., no temperature gradient inside the droplet and the connected pore body. In our model, the free-flow temperature affects mainly the energy exchange between the droplet and the surrounding gas through heat conduction. Since we assume no temperature gradient inside the droplet and the connected pore body, the energy exchanged with the free flow is consumed not only near the surface of the droplet but to change the temperature of the whole droplet and the pore body connected to it. Thus, our model underestimates the change in the droplet surface temperature due to energy exchange with the free flow. Another reason is the heat conductive exchange between the droplet and the inlet pore body, where a constant temperature of 298.15 K is applied.

Figure 6.14b shows that when the inlet relative humidity of the free flow is 16%, increasing the free-flow temperature results in longer evaporation time. This is because the gas phase with a specific relative humidity contains more vapor concentration in a higher temperature, which decreases the evaporation rate with increasing the temperature in a constant relative humidity.

In Fig. 6.14c, when gas with temperature of 308.15 K and relative humidity of 64% is injected to the inlet of the free-flow channel, droplet evaporation does not occur and the droplet volume remains constant. In that case, due to the cooling effect of the droplet, the temperature drops to (near) the dew point at the vicinity of the droplet surface, which stops the evaporation. Although, in such a case, condensation might occur, since a concept to describe the possible condensation process is not included in our model, the droplet volume remains constant in the simulation.

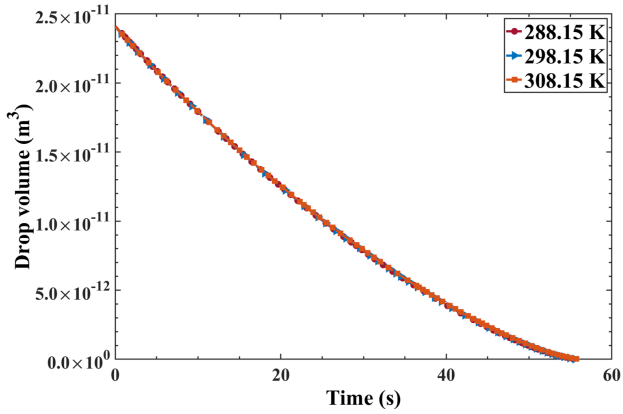

(a)

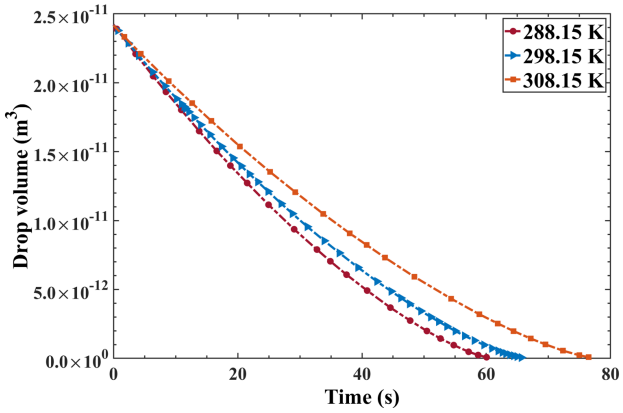

(b)

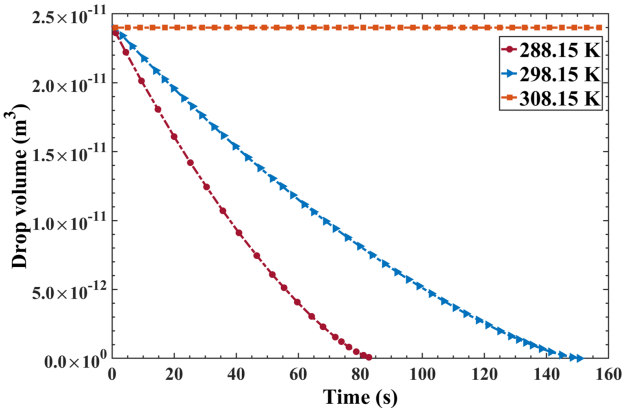

(c)

Figure 6.14: Variation of the droplet volume over time due to evaporation in three free-flow temperatures: a) relative humidity = 0%, b) relative humidity = 16%, and c) relative humidity = 64%.

6.3.6 Impact of free-flow velocity

To analyze the impact of free-flow velocity on droplet evaporation, we define two velocity groups: low range (0–0.1 m/s) and high range (0.5–10 m/s). Figure 6.15 shows how free-flow velocity affects droplet evaporation. The results shown in these figures are for cases where inlet free-flow and pore temperatures are equal to 298.15 K and the relative humidity of the gas flowing into the free-flow channel is 16%. Figures 6.15a and 6.15b show the change in the droplet volume with time due to evaporation for the two groups of free-flow velocities. The velocity values reported in these figures are the maximum velocities applied to the inlet of the free-flow channel, which occurs on the center line of the channel. In Fig. 6.15a, which shows the results for the low range of free-flow velocity, the droplet volume decreases with an almost constant rate during the whole period of time, i.e., constant evaporation rate over time. For the high range of free-flow velocities shown in Fig. 6.15b, however, the rate of the droplet shrinkage declines over time, i.e., decreasing the evaporation rate with time. Such a behavior is more evident by looking at the evaporation rate versus time shown by Fig. 6.15c, where the droplet evaporation rate experiences a rapid decrease over time when the free-flow velocity is 0.5 m/s in comparison with the lower velocities. Considering the velocity profile in the channel, the velocity varies from zero at the walls to a maximum at the center line of the channel. During the shrinkage of the droplet due to the evaporation, the droplet surface moves further from the center line and closer to the bottom wall. In fact, the effective free-flow velocity acting on the surface of the droplet decreases with the droplet shrinkage, which accelerates the reduction of the evaporation rate. This change in the velocity of the free flow impacting the droplet is more considerable when the free-flow velocity in the channel is higher.

How the impact of free-flow velocity on evaporation differs with the relative humidity of free flow is shown by Fig. 6.16. Regardless of the relative humidity, increasing the free-flow velocity is in favor of droplet evaporation, although the impact of raising the velocity is greater when the original velocity is lower. Furthermore, the free-flow velocity increases the evaporation rate more significantly when the relative humidity of the gas flowing into the free-flow channel is lower.

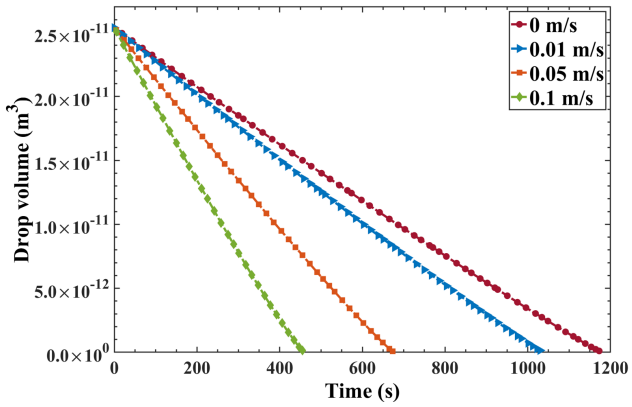

(a)

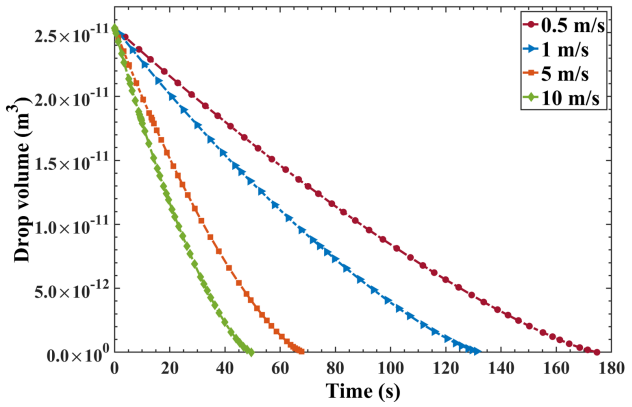

(b)

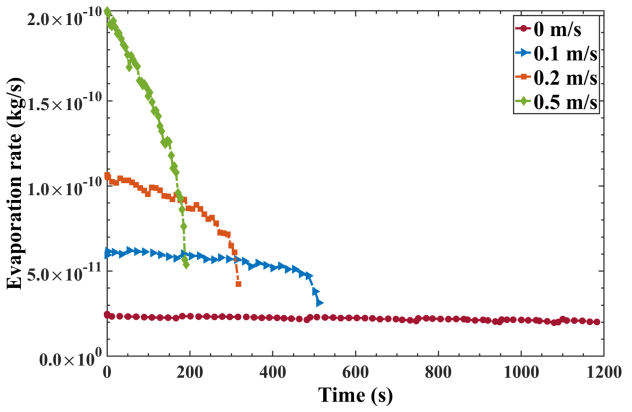

(c)

Figure 6.15: Droplet volume variation over time due to evaporation for a) free-flow velocities in the range of 0–0.1 m/s and b) free-flow velocities in the range of 0.5–10 m/s. c) Impact of free-flow velocity on the droplet evaporation rate.

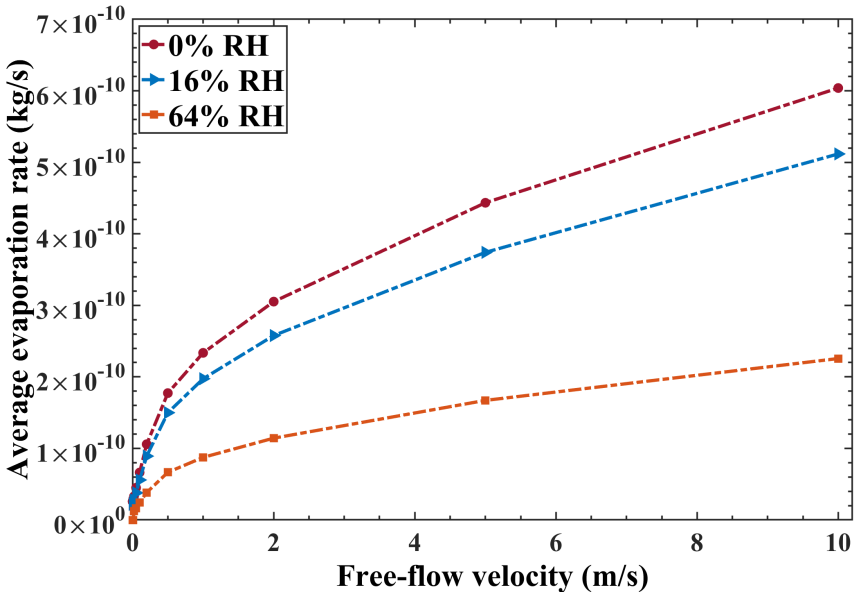

Figure 6.16: Impact of free-flow velocity on the average evaporation rate of the droplet in three free-flow relative humidities.

According to our assumption, local thermodynamic equilibrium holds at the surface of the droplet. This means that the air at the surface of the droplet is totally saturated with vapor. That creates a concentration gradient, which causes a diffusive flux of vapor from the surface of the droplet into the free flow. In the absence of the free flow, i.e., free-flow velocity = 0 m/s, a low concentration gradient is established between the surface of the droplet and the surrounding. The free flow brings the air with lower vapor concentration, i.e., lower relative humidity, from upstream and replace the high concentrated air surrounding the droplet. This causes an increase in the concentration gradient and boosts the evaporation. When the free-flow velocity is so low that the concentration gradient around the droplet remains low, a small increase in the velocity leads to supplying the less humid air to the surrounding of the droplet and increases the evaporation rate. However, when the free-flow velocity is high enough to maintain a high concentration gradient around the droplet, raising the velocity might still increase the air supply, but the degree of the consequent change in the concentration gradient is limited. In addition, the upstream humidity determines how significant such a boosting effect is. When the upstream air contains a high concentration of vapor, it impacts the concentration gradient around the droplet to some extent, even in a free flow with high velocity. Consequently, increasing the free-flow velocity influences the evaporation rate

less when the relative humidity of the air flowing into the channel is higher, which is in agreement with the experimental data presented by Jodat and Moghiman [2012] for the impact of forced convection in gas flow on evaporation. It also should be noted that the maximum concentration gradient, which theoretically can be achieved by increasing the free-flow velocity, is limited by the difference between the relative humidity applied at the channel inlet and the 100% relative humidity at the droplet surface.

6.3.7 Impact of pore fluid temperature

In this section, we investigate the impact of the inlet pore body temperature on the droplet evaporation. The inlet free-flow temperature is the same for all cases and equal to 298.15 K.

Figure 6.17a shows how the average evaporation rate changes with inlet pore body temperature. Raising the pore body temperature increases the average evaporation rate. Such an impact becomes more significant as the temperature goes up. Changing the temperature of the pore leads to change in the droplet temperature. The droplet temperature determines the vapor pressure at the surface of the droplet and, consequently, the concentration of vapor at the surface of the droplet. Thus, changing the pore temperature varies the vapor concentration gradient between the droplet surface and the surrounding free flow. For instance, increasing the pore temperature increases the vapor pressure, which raises the vapor concentration in the air at the surface of the droplet.

The variation of the evaporation rate versus time is shown in Fig. 6.17b for a case where the free-flow relative humidity is 16%. According to this figure, for all three humidity values, evaporation rate decreases with time, which is a result of the droplet shrinkage and less surface area available for the evaporation. Looking at the graph for each humidity, at least two main trends with different slopes are evident. Each graph is composed of a period of constant decrease in the evaporation rate followed by a change in the slope and a steeper reduction of the evaporation rate. This behavior could be related to the switch in the evaporation mode from constant contact angel to constant contact radius mode. Figure 6.17c shows the shrinkage of the droplet with time for different pore temperatures.

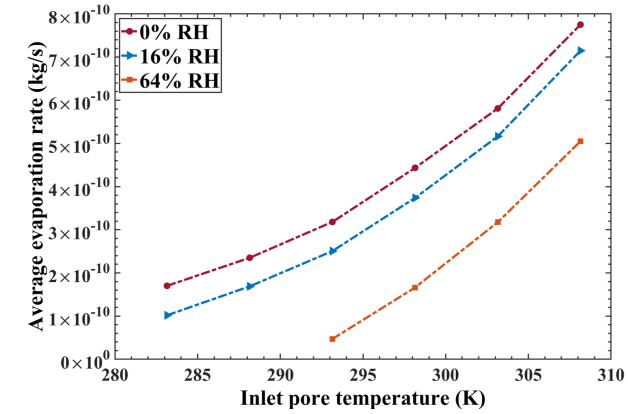

(a)

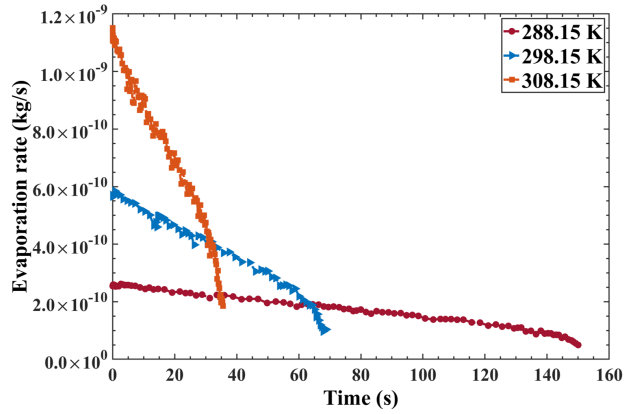

(b)

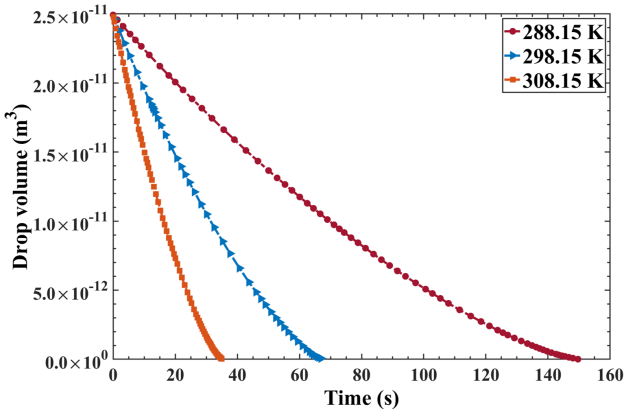

(c)

Figure 6.17: a) Variation of droplet average evaporation rate with inlet pore temperature and free-flow relative humidity, b) droplet evaporation rate over time for three inlet pore temperatures for a case where the free-flow relative humidity is 16%, and c) droplet volume variation during evaporation for three inlet pore temperatures for a case where the free-flow relative humidity is 16%.

6.3.8 Impact of contact angle

To analyze the impact of the contact angle on the droplet evaporation, we use three different contact angles. Figure 6.18a shows the variation of the droplet volume with time. According to the results, a droplet on a surface with higher contact angle evaporates faster. Figure 6.18b shows that by increasing the contact angle, the droplet surface area also increases, which could be a reason for the faster evaporation of a droplet on a surface with higher contact angle shown in Fig. 6.18a.

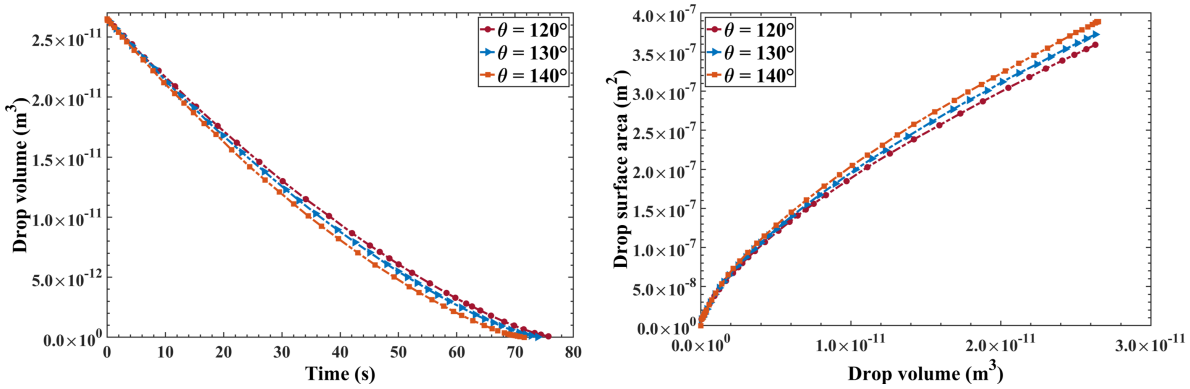

(a) (b)

Figure 6.18: Impact of surface contact angle on a) droplet volume over time and b) droplet surface area versus droplet volume during evaporation.

6.4 Impact of evaporation on droplet detachment

We have analyzed droplet dynamics and evaporation so far. In this section, we examine how droplet evaporation affects droplet detachment.

6.4.1 Simulation setup

The simulation setup used here is similar to the setup described in Section 6.3.1 with different boundary conditions applied to the inlet pore body. Unlike the droplet evaporation analysis in the previous section, the droplet forms and grows continuously at the interface as a result of water injection to the inlet pore body with a fixed injection

rate, q_{inlet}. At the same time, evaporation occurs at the surface of the droplet. Such a process continues until the free flow detaches the growing droplet.

6.4.2 Results

To examine the impact of the droplet evaporation on the droplet detachment, we applied different injection rates to the inlet pore, which results in droplets with different growth rates. We used three free-flow relative humidities (RH) in the channel. To compare the simulation results obtained for the droplet detachment under the impact of evaporation with cases without evaporation, we use a dimensionless parameter, $t^*_{\text{detachment}}$, which is the ratio of the detachment time predicted with evaporation to that without evaporation. Figure 6.19 shows the variation of $t^*_{\text{detachment}}$ with the injection rate and the free-flow relative humidity. As can be seen, $t^*_{\text{detachment}}$ is equal to one for the injection rate of 10^{-7}kg/s, no matter which free-flow relative humidity is applied, which means that the droplet evaporation has no impact on the droplet detachment in this case. In fact, in this case the evaporation rate is so small in comparison with the injection rate, that the change in the droplet growth due to the evaporation is not noticeable. By decreasing the injection rate, $t^*_{\text{detachment}}$ steadily increases, indicating the growing impact of the evaporation on delaying the droplet detachment. The degree of the evaporation influence is related to the relative humidity in the channel. For instance, for the injection rate of 10^{-9} kg/s and RH = 64 %, $t^*_{\text{detachment}}$ is 1.30 and for the same injection rate but RH = 16 %, $t^*_{\text{detachment}}$ is 2.45, while with the same injection rate and RH = 0 %, $t^*_{\text{detachment}}$ is ∞. The latter one indicates that the droplet will never be detached by the free flow due to the impact of the evaporation. In this case, the evaporation rate compensates the injection rate at a certain time point, i.e., the amount of water leaving the droplet surface due to the evaporation becomes equal to the amount coming to the droplet from the pore. Consequently, the droplet growth stops and the droplet volume remains constant. Such a behavior can also be observed when the injection rate is 5×10^{-10} kg/s and relative humidity is 0 % or 16 %.

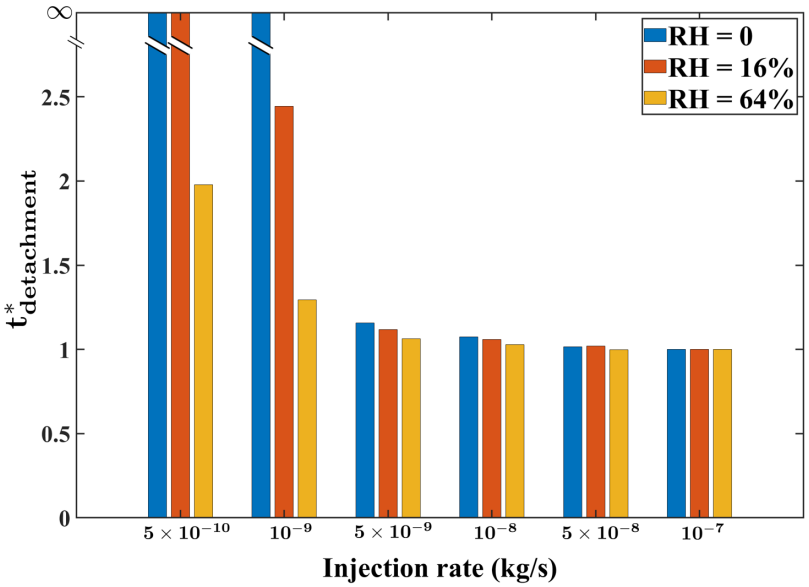

Figure 6.19: Impact of droplet evaporation on the change in the dimensionless detachment time, $t^*_{\text{detachment}}$ with injection rate to the throat.

Figure 6.20 shows the change in the detachment time with injection rate into the throat with and without droplet evaporation for free-flow relative humidities of 0% and 64%. This figure also shows that the droplet evaporation impacts the detachment only when the rate of liquid (water) from the pore coming to the droplet is small.

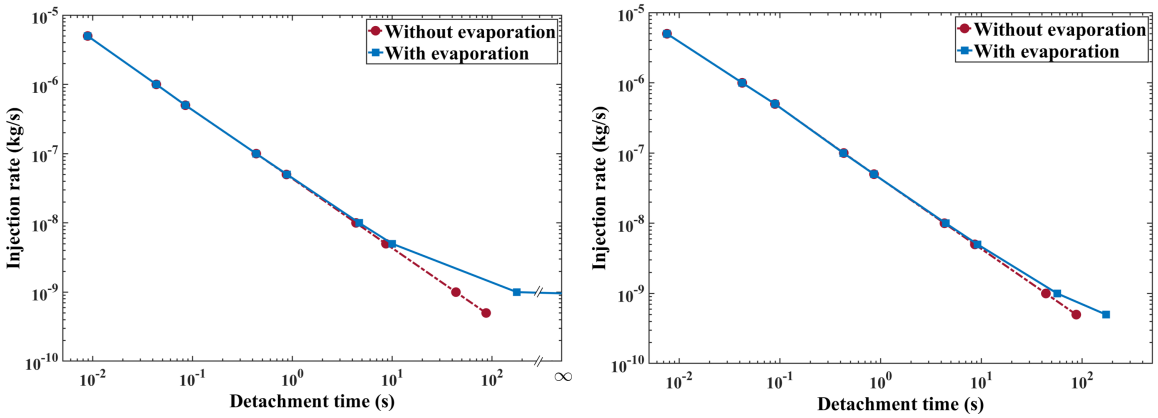

(a) (b)

Figure 6.20: Injection rate to the throat versus the detachment time with and without droplet evaporation.

6.5 Multiple droplets formation and evaporation at the interface of a free-flow–pore-network system

We use a setup shown in Fig. 6.21 to show the application of the model in describing formation and evaporation of multiple droplets at the interface of a non-isothermal compositional system. In this setup, the free-flow domain is a two-dimensional channel with dimensions of 2×10^{-2} m $\times$ 1×10^{-3} m (length $\times$ height). The porous medium is a pore network, which consists of 113 pore bodies connected by 154 pore throats. The radii of the pore bodies vary between 4×10^{-5} m and 8×10^{-5} m. The pore throats have radii from 2×10^{-5} m to 4×10^{-5} m and lengths from 9×10^{-6} m to 8×10^{-4} m. The free flow and the porous medium are coupled at the bottom wall of the channel. The free-flow channel is initially filled with air and the pore network is initially fully saturated with water.

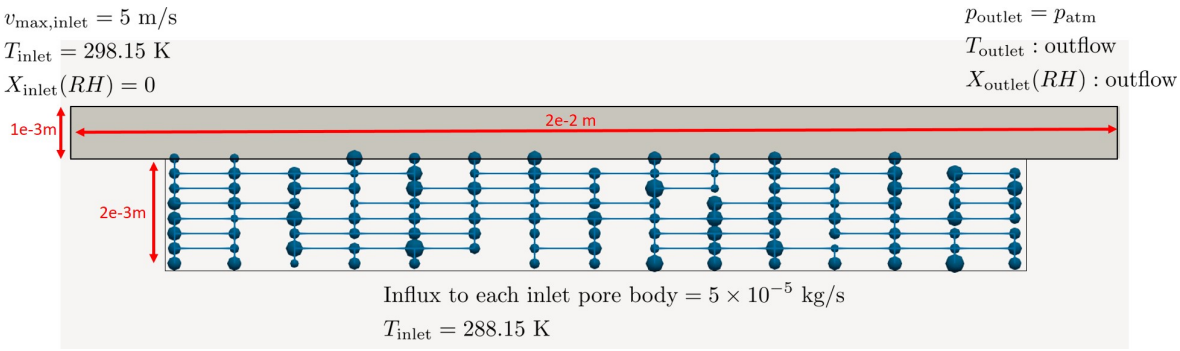

Figure 6.21: The setup used to simulate formation and evaporation of multiple droplets at the interface of a coupled free-flow–pore-network system.

Air flows into the channel with maximum velocity of 5 m/s in a fully developed laminar profile and the temperature of 298.15 K and the outlet of the channel is exposed to atmospheric pressure. Water is injected into the inlet pores of the network with a rate of 5×10^{-7} kg/s for a short time. The droplets form and grow onto pore bodies with various sizes at the interface. Then, the injection is stopped and we let the droplets evaporate. Figure 6.22 shows how formation and evaporation of multiple droplets affect the temperature and vapor mass fraction (concentration) distribution in the free flow.

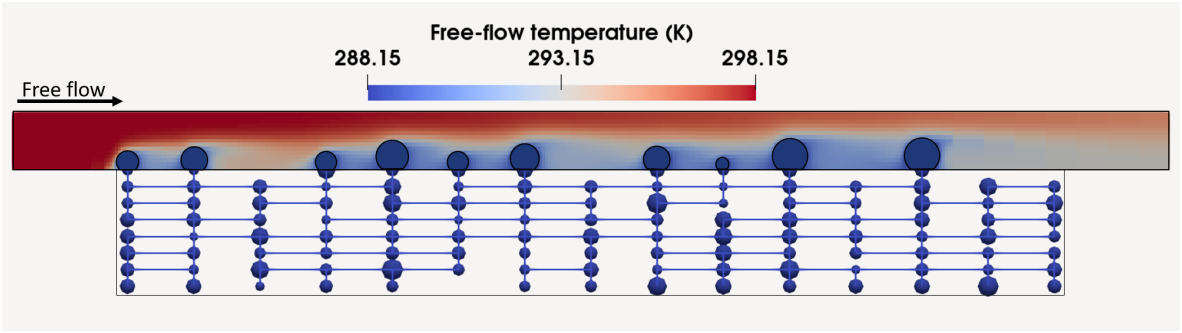

(a)

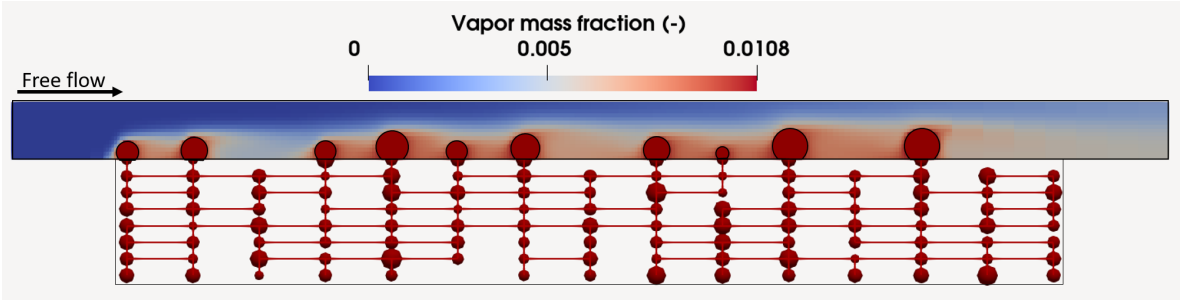

(b)

Figure 6.22: Simulation of formation and evaporation of multiple droplets at the interface: a) impact on the temperature field and b) impact on the vapor mass fraction.

7 Summary and outlook

7.1 Summary

The key element of this work is the development of a novel model to describe the formation, growth and detachment as well as evaporation of droplets at the interface between a coupled free-flow–porous medium system. Pore-network modeling is used as a tool to capture pore-scale phenomena occurring in porous media. New coupling concepts between the free flow and the porous medium are developed, which include storing mass, momentum and energy in the droplet. The formation and growth of a droplet is described and a new approach is developed to include the impact of the growing droplet on the free-flow field. Description of the forces acting in the system is given and accordingly the droplet detachment is predicted. A clear description of the droplet evaporation is provided and the impact of free-flow and porous medium properties on the droplet evaporation have been analyzed.

We implemented all the models developed in this work in DuMu^{x}, an open-source simulator for flow and transport in porous media.

Coupling concept for free flow and porous medium with droplets at the interface
We extended the coupling concept for a coupled free-flow–porous medium system without droplets at the interface to include the droplet impact on the mass, momentum, and energy exchange between the two domains. The new coupling concept not only describes the interaction between a droplet formed at the interface with the free flow and porous medium, but also accounts for storing mass and energy by the droplet.

In this work, we used pore-network modeling for the porous medium, which enables us to describe pore-scale phenomena in more detail. Furthermore, multiple emerging

droplets at the interface and their interactions with the porous medium could be well described.

In the coupling concept, interactions between the droplet and the porous medium occurs at the droplet–pore interface, where the droplet and the connected pore exchange mass, momentum, and energy. Assuming no gradient inside the droplet due to its small size, we use the thermodynamic properties at the droplet–pore interface for the whole droplet, i.e., the droplet and the connected pore have the same thermodynamic properties, e.g., pressure and temperature.

A droplet interacts with the surrounding free flow through its surface. Free-flow forces (i.e., pressure, shear and inertial forces) acts on the droplet surface. Due to the surface curvature, the capillary force acts on the droplet surface toward the droplet center. Ignoring the shear forces inside the droplet, the force acting on the droplet surface from inside is the droplet pressure force. Evaporation at the surface of the droplet transfers mass from the droplet into the free flow. The droplet exchanges energy with the free flow in the form of heat conduction and diffusive energy exchange due to the evaporation. In the concept presented in this work, the energy exchanged between the droplet and the free flow is distributed between the droplet and the connected pore.

A growing droplet impacts the free-flow field, which influences the whole interaction process between the droplet and the flow domains. To capture such an impact, we used an approach to recognize the grid cells/faces in a discretized free-flow domain, which are occupied by the droplet. The droplet related properties are applied to such grid cells (e.g., zero velocity is applied to the grid faces and droplet temperature to the grid cells occupied by the droplet).

Droplet dynamics: droplet formation, growth, and detachment Having developed the proper coupling conditions to include droplet effect on the free-flow–porous medium interactions, the droplet formation and growth is predicted by summing up the total mass exchanged at the droplet–pore interface and at the droplet–free-flow interface (i.e., droplet surface). A droplet grows if the net amount of mass exchanged between the droplet and the other domains is positive. Droplet shrinkage occurs if the mass leaving the droplet is greater than the mass coming to the droplet. The expansion/reduction of the droplet contact area at the interface follows a constant contact angle mode with a changing contact radius as long as the contact radius is greater than the connected pore

radius. A constant contact radius mode with a changing contact angle describes the droplet growth/shrinkage, when the droplet contact radius is equal to the pore radius.

We developed a concept for droplet detachment by identifying the forces involved, i.e., free-flow forces and the adhesion force acting on the triple contact line. The free-flow drag force, known as the main driving force of droplet detachment, is estimated by integrating the free-flow pressure, shear and inertial forces in the flow direction over the droplet surface and summing them up to obtain the total drag force affecting the droplet as a whole. On the other side, the net adhesion force, stemming from the contact angle hysteresis at the triple contact line and surface tension, works to keep the droplet at the interface. Comparing the free-flow drag force and the adhesion force provides a criterion to predict the droplet detachment.

Droplet evaporation In this work, droplet evaporation into the free flow is described as a diffusion-driven phenomenon. That means that evaporation occurs due to diffusive transport of vapor from the droplet surface to the surrounding free flow, driven by the vapor concentration gradient. To estimate the evaporation rate, we assume local thermodynamic equilibrium at the droplet surface. Using Raoult's law and Dalton's law for ideal solutions, we then compute the vapor concentration at the droplet surface as a function of pressure and temperature. We employ the Fick's law of diffusion to calculate the evaporative flux at each point of the droplet surface. Integrating the evaporative mass flux over the droplet surface gives the total mass flux leaving the droplet due to the evaporation.

7.2 Conclusions

Coupling concept for free flow and porous medium with droplets at the interface The new coupling concept developed in this work to include droplet impact at the interface was implemented and used in simulations of droplet dynamics and droplet evaporation.

Droplet dynamics: droplet formation, growth, and detachment We compared the simulations results with experimental data for a single droplet forming and growing

on a hydrophobic porous medium. This comparison showed that our model is able to accurately describe such a process. It was shown that the description of the growing mode, i.e., variation of contact angle and radius of curvature, is in a good agreement with the experiment.

We used our model to predict the droplet detachment from the interface and compared the results with experimental data provided by Theodorakakos et al. [2006a]. In this comparison, a droplet forms at the interface with a specific volume. Then, the free-flow velocity increases until it detaches the droplet. We obtained a good match between the simulation results and the experimental data for prediction of droplet detachment volume.

Comparing the simulation results using our model with ANSYS Fluent simulations for a growing droplet at the interface showed that while the predictions for droplet detachment height are in a close agreement, there are differences in predictions of droplet detachment volume, especially in low free-flow velocities. Such a behavior stems from the impact of droplet deformation, which is not included in our model.

We used different description of the adhesion (hysteresis) force and analyzed the impact of droplet contact angle hysteresis on the detachment predictions.

How a neighboring growing droplet affects the droplet detachment is examined. The results show that a neighboring droplet located upstream might significantly delay the droplet detachment. However, when the upstream droplet detaches at an earlier time, it could advance the droplet detachment.

Benefiting from the low computational cost of simulations using the new developed model, we presented a show test case in which multiple droplets form and grow at the interface between a free flow and a porous medium and finally are detached by the free flow.

Droplet evaporation Using the developed model for droplet evaporation to simulate evaporation of a confined single droplet in a channel with different lengths and comparing the results with the experimental data provided by Bansal et al. [2017] showed that our model is able to provide a proper description of the evaporation process and the impact of confinement on the evaporation rate.

We carried out an analysis to examine how free-flow properties (e.g., free-flow velocity, relative humidity and temperature) and porous medium properties (e.g., pore size and temperature) affect the droplet evaporation. The results show that increasing free-flow velocity and decreasing relative humidity increases the evaporation rate. Our conceptual model underestimates the impact of free-flow temperature. That occurs because the energy exchanged between the droplet and the free flow distributes to the droplet and the connected pore. The connected pore size affects the evaporation rate by impacting the evaporation mode. Increasing the pore temperature boosts the droplet evaporation by increasing the vapor pressure.

Through examining the impact of droplet evaporation on detachment predictions, we found that the droplet evaporation could delay the droplet detachment by decreasing the droplet growing rate depending on the rate of fluid fed to the droplet by the connected pore. Such an impact could be so significant that prevents the droplet detachment.

7.3 Outlook

The modeling concepts introduced in this work help us to gain a better understanding about the impact of multiple droplets formation at the interface between a free flow and a porous medium on the exchange of mass, energy, and momentum between these two flow domains. They could be used as a tool to analyze interactions of a droplet at the interface with the free flow and the porous medium and examine the influence of the free-flow and porous medium properties. Being able to predict the droplet detachment and describing the droplet evaporation, the model developed here could be used in technical applications (e.g., water management in fuel cells and cooling systems) for optimization purposes.

Our model could serve as a basis for further developments, e.g., describing film flow at the interface. It also could be used as an input provider for homogenization and upscaling of transport in coupled free-flow–porous medium systems, including droplets.

Coupling concept for free flow and porous medium with droplets at the interface
The modeling concepts presented in this study has been developed for formation of

droplets at hydrophobic interfaces. Thus, to be relevant for hydrophilic interfaces, small modifications are required.

In this work, we assume there is no gradient of pressure, temperature, and concentration inside the droplet. However, flow circulation inside the droplet and higher change in the surface temperature of an evaporating droplet have been observed [e.g., Hu and Larson, 2002, 2005, Prakash et al., 2021]. Further analysis is needed to examine the influence of no-gradient assumptions made in the development of our concepts.

The assumption of local thermodynamic equilibrium has been made on droplet–free-flow and droplet–pore interface, as well as in the pore-network model. Such assumptions in the porous medium results in equality of the solid and fluid temperatures. Employing the concept introduced by Koch et al. [2021b] to capture the local thermal non-equilibrium effects in the porous medium, the solid and fluid could have different temperatures. At the interface, the local thermal non-equilibrium concept leads to difference between the temperature of the droplet–pore interface and the temperature of the droplet–solid contact area. Thus, in such a configuration, the coupling concepts should be modified to include the conductive heat transfer between the droplet and the solid surface.

Droplet dynamics: droplet formation, growth, and detachment We described a droplet at the interface as a part of a sphere and did not include the effect of droplet deformation due to the free flow in our model. Development of a concept to describe the impact of the droplet deformation is desirable. A possible idea could be describing a droplet using two hemispheres with different surface curvatures.

In the present model, coalescence of two or more neighboring droplets at the interface, which could appear when the distance between the pores at the interface is short, is not included. However, development of a simplified concept to describe such a phenomenon has been started.

To capture the impact of a growing/shrinking droplet at the interface on the free-flow field, we introduced an approach in which the droplet properties are applied to the free-flow cells which are occupied by the droplet. This simplified approach enables us to take the impact of multiple droplets at the interface into account without needing to solve the flow inside each droplet and to consider two-phase flow in the free-flow

domain. This approach could be improved by accounting for the mass being suddenly captured/released during droplet growth/shrinkage through assigning the droplet properties to the occupied free-flow grid cells. One idea could be to impose corresponding mass source/sink terms to the free-flow cells, which are beside the droplet surface and not invaded by the droplet.

Droplet evaporation We introduced a concept to describe the mode of droplet growth and shrinkage, i.e., constant contact angle and constant contact radius mode. This concept could be easily extended to include the pinning and depinning behavior of a growing/shrinking droplet observed in, e.g., Pittoni et al. [2013], Wang and Wu [2013], in more details.

Bibliography

S. Ackermann, C. Bringedal, and R. Helmig. Multi-scale three-domain approach for coupling free flow and flow in porous media including droplet-related interface processes. *Journal of Computational Physics*, 429:109993, 2021.

S. Ackermann, S. Fest-Santini, M. Veyskarami, R. Helmig, and M. Santini. Experimental validation of a coupling concept for drop formation and growth onto porous materials by high-resolution x-ray imaging technique. *International Journal of Multiphase Flow*, 160:104371, 2023.

M. E. A. B. Amara and S. B. Nasrallah. Numerical simulation of droplet dynamics in a proton exchange membrane (pemfc) fuel cell micro-channel. *International journal of hydrogen energy*, 40(2):1333–1342, 2015.

C. Antonini, F. Carmona, E. Pierce, M. Marengo, and A. Amirfazli. General methodology for evaluating the adhesion force of drops and bubbles on solid surfaces. *Langmuir*, 25(11):6143–6154, 2009.

M. Arai and T. Suidzu. Porous ceramic coating for transpiration cooling of gas turbine blade. *Journal of Thermal Spray Technology*, 22(5):690–698, 2013.

K. Baber. *Coupling free flow and flow in porous media in biological and technical applications: From a simple to a complex interface description*. Stuttgart: Eigenverlag des Instituts für Wasser-und Umweltsystemmodellierung, 2014.

K. Baber, K. Mosthaf, B. Flemisch, R. Helmig, S. Müthing, and B. Wohlmuth. Numerical scheme for coupling two-phase compositional porous-media flow and one-phase compositional free flow. *The IMA Journal of Applied Mathematics*, 77(6):887–909, 2012.

K. Baber, B. Flemisch, and R. Helmig. Modeling drop dynamics at the interface between free and porous-medium flow using the mortar method. *International Journal of Heat and Mass Transfer*, 99:660–671, 2016.

M. T. Balhoff, K. E. Thompson, and M. Hjortsø. Coupling pore-scale networks to continuum-scale models of porous media. *Computers & Geosciences*, 33(3):393–410, 2007.

L. Bansal, S. Chakraborty, and S. Basu. Confinement-induced alterations in the evaporation dynamics of sessile droplets. *Soft Matter*, 13(5):969–977, 2017.

S. Basu, K. Nandakumar, and J. H. Masliyah. A model for detachment of a partially wetting drop from a solid surface by shear flow. *Journal of colloid and interface science*, 190(1):253–257, 1997.

M. J. Blunt. *Multiphase flow in permeable media: A pore-scale perspective*. Cambridge university press, 2017.

E. Bormashenko, A. Musin, and M. Zinigrad. Evaporation of droplets on strongly and weakly pinning surfaces and dynamics of the triple line. *Colloids and Surfaces A: Physicochemical and Engineering Aspects*, 385(1-3):235–240, 2011.

C. Bourges-Monnier and M. Shanahan. Influence of evaporation on contact angle. *Langmuir*, 11(7):2820–2829, 1995.

H. C. Brinkman. A calculation of the viscous force exerted by a flowing fluid on a dense swarm of particles. *Flow, Turbulence and Combustion*, 1(1):27–34, 1949.

D. Brutin. *Droplet wetting and evaporation: from pure to complex fluids*. Academic Press, 2015.

Y. A. Cengel, M. A. Boles, and M. Kanoğlu. *Thermodynamics: an engineering approach*, volume 5. McGraw-hill New York, 2011.

C. Charcosset. Preparation of emulsions and particles by membrane emulsification for the food processing industry. *Journal of Food Engineering*, 92(3):241–249, 2009.

K. S. Chen, M. A. Hickner, and D. R. Noble. Simplified models for predicting the onset of liquid water droplet instability at the gas diffusion layer/gas flow channel interface. *International Journal of Energy Research*, 29(12):1113–1132, 2005.

S. C. Cho, Y. Wang, and K. S. Chen. Droplet dynamics in a polymer electrolyte fuel cell gas flow channel: Forces, deformation, and detachment. i: Theoretical and numerical analyses. *Journal of power sources*, 206:119–128, 2012.

H. Class, R. Helmig, and P. Bastian. Numerical simulation of non-isothermal multiphase multicomponent processes in porous media.: 1. an efficient solution technique. *Advances in water resources*, 25(5):533–550, 2002.

S. Dash and S. V. Garimella. Droplet evaporation dynamics on a superhydrophobic surface with negligible hysteresis. *Langmuir*, 29(34):10785–10795, 2013.

H. Y. Erbil. Evaporation of pure liquid sessile and spherical suspended drops: A review. *Advances in colloid and interface science*, 170(1-2):67–86, 2012.

C. Fang, C. Hidrovo, F.-m. Wang, J. Eaton, and K. Goodson. 3-d numerical simulation of contact angle hysteresis for microscale two phase flow. *International Journal of Multiphase Flow*, 34(7):690–705, 2008.

X. Fang, B. Li, E. Petersen, Y. Ji, J. C. Sokolov, and M. H. Rafailovich. Factors controlling the drop evaporation constant. *The Journal of Physical Chemistry B*, 109(43):20554–20557, 2005.

N. A. Fuchs. *Evaporation and droplet growth in gaseous media*. Elsevier, 2013.

D. E. Glass, A. D. Dilley, and H. N. Kelly. Numerical analysis of convection/transpiration cooling. *Journal of Spacecraft and Rockets*, 38(1):15–20, 2001.

M. Guilizzoni. Drop shape visualization and contact angle measurement on curved surfaces. *Journal of Colloid and Interface Science*, 364(1):230–236, 2011. doi: 10.1016/j.jcis.2011.08.019.

L. Hao and P. Cheng. An analytical model for micro-droplet steady movement on the hydrophobic wall of a micro-channel. *International Journal of Heat and Mass Transfer*, 53(5-6):1243–1246, 2010.

J. P. Hartnett and M. M. Kostic. Heat transfer to newtonian and non-newtonian fluids in rectangular ducts. *Advances in heat transfer*, 19:247–356, 1989.

S. M. Hassanizadeh and W. G. Gray. Thermodynamic basis of capillary pressure in porous media. *Water resources research*, 29(10):3389–3405, 1993.

S. Hatte, K. Pandey, K. Pandey, S. Chakraborty, and S. Basu. Universal evaporation dynamics of ordered arrays of sessile droplets. *Journal of Fluid Mechanics*, 866:61–81, 2019.

R. Helmig et al. *Multiphase flow and transport processes in the subsurface: a contribution to the modeling of hydrosystems*, volume 1. Springer, 1997.

H. Hu and R. G. Larson. Evaporation of a sessile droplet on a substrate. *The Journal of Physical Chemistry B*, 106(6):1334–1344, 2002.

H. Hu and R. G. Larson. Analysis of the microfluid flow in an evaporating sessile droplet. *Langmuir*, 21(9):3963–3971, 2005.

R. Huber and R. Helmig. Node-centered finite volume discretizations for the numerical simulation of multiphase flow in heterogeneous porous media. *Computational Geosciences*, 4(2):141–164, 2000.

D. Jamet, M. Chandesris, and B. Goyeau. On the equivalence of the discontinuous one-and two-domain approaches for the modeling of transport phenomena at a fluid/porous interface. *Transport in porous media*, 78(3):403–418, 2009.

A. Jodat and M. Moghiman. An experimental assessment of the evaporation correlations for natural, forced and combined convection regimes. *Proceedings of the Institution of Mechanical Engineers, Part C: Journal of Mechanical Engineering Science*, 226(1):145–153, 2012.

V. Joekar-Niasar. *The immiscibles: Capillarity effects in porous media-pore-network modelling*. Universiteit Utrecht, Departement Aardwetenschappen, 2010.

V. Joekar-Niasar and S. Hassanizadeh. Analysis of fundamentals of two-phase flow in porous media using dynamic pore-network models: A review. *Critical reviews in environmental science and technology*, 42(18):1895–1976, 2012.

V. Joekar-Niasar and S. M. Hassanizadeh. Effect of fluids properties on non-equilibrium capillarity effects: Dynamic pore-network modeling. *International Journal of Multiphase Flow*, 37(2):198–214, 2011.

T. Koch, D. Gläser, K. Weishaupt, S. Ackermann, M. Beck, B. Becker, S. Burbulla, H. Class, E. Coltman, S. Emmert, et al. Dumux 3–an open-source simulator for

solving flow and transport problems in porous media with a focus on model coupling. *Computers & Mathematics with Applications*, 81:423–443, 2021a.

T. Koch, K. Weishaupt, J. Müller, B. Weigand, and R. Helmig. A (dual) network model for heat transfer in porous media: Toward efficient model concepts for coupled systems from fuel cells to heat exchangers. *Transport in Porous Media*, 140(1):107–141, 2021b.

S. Kulinich and M. Farzaneh. Effect of contact angle hysteresis on water droplet evaporation from super-hydrophobic surfaces. *Applied Surface Science*, 255(7):4056–4060, 2009.

E. Kumbur, K. Sharp, and M. Mench. Liquid droplet behavior and instability in a polymer electrolyte fuel cell flow channel. *Journal of Power Sources*, 161(1):333–345, 2006.

G. Lamanna, S. Tonini, G. E. Cossali, B. Weigand, et al. *Droplet Interactions and Spray Processes*. Springer, 2020.

X.-B. Li, F.-C. Li, J.-C. Yang, H. Kinoshita, M. Oishi, and M. Oshima. Study on the mechanism of droplet formation in t-junction microchannel. *Chemical engineering science*, 69(1):340–351, 2012.

X.-M. Li, D. Reinhoudt, and M. Crego-Calama. What do we need for a superhydrophobic surface? a review on the recent progress in the preparation of superhydrophobic surfaces. *Chemical Society Reviews*, 36(8):1350–1368, 2007.

G. Mason and N. R. Morrow. Capillary behavior of a perfectly wetting liquid in irregular triangular tubes. *Journal of Colloid and Interface Science*, 141(1):262–274, 1991.

J. C. Maxwell. *Collected Scientific Papers. Vol. 2*. CUP, 1890.

C. Michalkowski, M. Veyskarami, C. Bringedal, R. Helmig, and V. Schleper. Two-phase flow dynamics at the interface between gdl and gas distributor channel using a pore-network model. *Transport in Porous Media*, 144(2):429–458, Sep 2022. ISSN 1573-1634. doi: 10.1007/s11242-022-01813-4.

K. Mosthaf, K. Baber, B. Flemisch, R. Helmig, A. Leijnse, I. Rybak, and B. Wohlmuth. A coupling concept for two-phase compositional porous-medium and single-phase compositional free flow. *Water Resources Research*, 47(10), 2011.

D. Niblett, A. Mularczyk, V. Niasar, J. Eller, and S. Holmes. Two-phase flow dynamics in a gas diffusion layer-gas channel-microporous layer system. *Journal of Power Sources*, 471:228427, 2020.

D. Orejon, K. Sefiane, and M. E. Shanahan. Stick–slip of evaporating droplets: substrate hydrophobicity and nanoparticle concentration. *Langmuir*, 27(21):12834–12843, 2011.

P.-E. Øren, S. Bakke, and O. J. Arntzen. Extending predictive capabilities to network models. *SPE journal*, 3(04):324–336, 1998.

R. Picknett and R. Bexon. The evaporation of sessile or pendant drops in still air. *Journal of colloid and Interface Science*, 61(2):336–350, 1977.

P. G. Pittoni, C.-C. Chang, T.-S. Yu, and S.-Y. Lin. Evaporation of water drops on polymer surfaces: Pinning, depinning and dynamics of the triple line. *Colloids and Surfaces A: Physicochemical and Engineering Aspects*, 432:89–98, 2013.

J. Prakash, B. S. Sikarwar, and B. K. Agarwal. Flow and thermal field in sessile droplet evaporation at various environmental conditions. *Heat Transfer*, 50(5):4535–4551, 2021.

C. Qin, D. Rensink, S. Fell, and S. M. Hassanizadeh. Two-phase flow modeling for the cathode side of a polymer electrolyte fuel cell. *Journal of power sources*, 197: 136–144, 2012.

C. Quesnel, R. Cao, J. Lehr, A.-M. Kietzig, A. Z. Weber, and J. T. Gostick. Dynamic percolation and droplet growth behavior in porous electrodes of polymer electrolyte fuel cells. *The Journal of Physical Chemistry C*, 119(40):22934–22944, 2015.

S. Rashidi, J. A. Esfahani, and N. Karimi. Porous materials in building energy technologies—a review of the applications, modelling and experiments. *Renewable and Sustainable Energy Reviews*, 91:229–247, 2018.

M. Santini, M. Guilizzoni, and S. Fest-Santini. X-ray computed microtomography for drop shape analysis and contact angle measurements. *Journal of Colloid Interface Science*, 409:204–210, 2013. doi: 10.1016/j.jcis.2013.06.036.

M. Santini, S. Fest-Santini, and P. Foltyn. On the local mass transfer rates around arbitrary shaped particles calculated by x-ray computed microtomography: prospective for a novel experimental technique. *International Communication in Heat and Mass Transfer*, 79:135–139, 2016. doi: 10.1016/j.icheatmasstransfer.2016.11.001.

M. Schneider, K. Weishaupt, D. Gläser, W. M. Boon, and R. Helmig. Coupling staggered-grid and mpfa finite volume methods for free flow/porous-medium flow problems. *Journal of Computational Physics*, 401:109012, 2020.

A. J. D. Shaikeea and S. Basu. Insight into the evaporation dynamics of a pair of sessile droplets on a hydrophobic substrate. *Langmuir*, 32(5):1309–1318, 2016.

D. H. Shin, S. H. Lee, J.-Y. Jung, and J. Y. Yoo. Evaporating characteristics of sessile droplet on hydrophobic and hydrophilic surfaces. *Microelectronic Engineering*, 86 (4-6):1350–1353, 2009.

B. Sobac and D. Brutin. Triple-line behavior and wettability controlled by nanocoated substrates: influence on sessile drop evaporation. *Langmuir*, 27(24):14999–15007, 2011.

H. Song, Y. Lee, S. Jin, H.-Y. Kim, and J. Y. Yoo. Prediction of sessile drop evaporation considering surface wettability. *Microelectronic Engineering*, 88(11):3249–3255, 2011.

T. Sweijen, S. M. Hassanizadeh, B. Chareyre, and L. Zhuang. Dynamic pore-scale model of drainage in granular porous media: The pore-unit assembly method. *Water resources research*, 54(6):4193–4213, 2018.

A. Theodorakakos, T. Ous, M. Gavaises, J. Nouri, N. Nikolopoulos, and H. Yanagihara. Dynamics of water droplets detached from porous surfaces of relevance to pem fuel cells. *Journal of Colloid Interface Science*, 300:673–687, 2006a. doi: 10.1016/j.jcis.2006.04.021.

A. Theodorakakos, T. Ous, M. Gavaises, J. Nouri, N. Nikolopoulos, and H. Yanagihara. Dynamics of water droplets detached from porous surfaces of relevance to pem fuel cells. *Journal of colloid and interface science*, 300(2):673–687, 2006b.

W. Thomson. 4. on the equilibrium of vapour at a curved surface of liquid. *Proceedings of the Royal Society of Edinburgh*, 7:63–68, 1872.

I. TIMELAPSE VISION. Perspiration on a human fingertip. `https://timelapsevision.com/en`, 2017. Accessed: 2023-11-09.

M. Veyskarami, C. Michalkowski, C. Bringedal, and R. Helmig. Droplet formation, growth and detachment at the interface of a coupled free-flow–porous medium system: A new model development and comparison. *Transport in Porous Media*, 149(2):389–419, Sep 2023. ISSN 1573-1634. doi: 10.1007/s11242-023-01944-2.

H.-J. Vogel and K. Roth. Quantitative morphology and network representation of soil pore structure. *Advances in water resources*, 24(3-4):233–242, 2001.

D. Wang, Y. Jiang, Z. Zhu, W. Yin, K. Asawa, C.-H. Choi, and J. W. Drelich. Contact line and adhesion force of droplets on concentric ring-textured hydrophobic surfaces. *Langmuir*, 36(10):2622–2628, 2020.

F.-C. Wang and H.-A. Wu. Pinning and depinning mechanism of the contact line during evaporation of nano-droplets sessile on textured surfaces. *Soft Matter*, 9(24): 5703–5709, 2013.

W. Wang, Z. Liu, Y. Jin, and Y. Cheng. Lbm simulation of droplet formation in micro-channels. *Chemical engineering journal*, 173(3):828–836, 2011.

K. Weishaupt. *Model concepts for coupling free flow with porous medium flow at the pore-network scale: from single-phase flow to compositional non-isothermal two-phase flow*. Stuttgart: Eigenverlag des Instituts für Wasser-und Umweltsystemmodellierung, 2020.

K. Weishaupt, V. Joekar-Niasar, and R. Helmig. An efficient coupling of free flow and porous media flow using the pore-network modeling approach. *Journal of Computational Physics: X*, 1:100011, 2019a.

K. Weishaupt, A. Terzis, I. Zarikos, G. Yang, M. de Winter, and R. Helmig. Model reduction for coupled free flow over porous media: a hybrid dimensional pore network model approach. *arXiv preprint arXiv:1908.01771*, 2019b.

J. Xie, J. Xu, W. Shang, and K. Zhang. Mode selection between sliding and rolling for droplet on inclined surface: Effect of surface wettability. *International Journal of Heat and Mass Transfer*, 122:45–58, 2018.

T. Young. An essay on the cohesion of fluids. In *Abstracts of the Papers Printed in the Philosophical Transactions of the Royal Society of London*, number 1, pages 171–172. The Royal Society London, 1832.

D. Zhang, R. Zhang, S. Chen, and W. E. Soll. Pore scale study of flow in porous media: Scale dependency, rev, and statistical rev. *Geophysical research letters*, 27 (8):1195–1198, 2000.

X. Zhu, P. Sui, and N. Djilali. Dynamic behaviour of liquid water emerging from a gdl pore into a pemfc gas flow channel. *Journal of Power Sources*, 172(1):287–295, 2007.

Institut für Wasser- und Umweltsystemmodellierung
Universität Stuttgart

Pfaffenwaldring 61
70569 Stuttgart (Vaihingen)
Telefon (0711) 685 - 60156
Telefax (0711) 685 - 51073
E-Mail: iws@iws.uni-stuttgart.de
http://www.iws.uni-stuttgart.de

Direktoren
Prof. Dr.-Ing. Rainer Helmig
Prof. Dr.-Ing. Wolfgang Nowak
Prof. Dr.-Ing. Silke Wieprecht

Emeriti
Prof. Dr.-Ing. habil. Dr.-Ing. E.h. Jürgen Giesecke
Prof. Dr.h.c. Dr.-Ing. E.h. Helmut Kobus, PhD

Lehrstuhl für Wasserbau und Wassermengenwirtschaft
Leiterin: Prof. Dr.-Ing. Silke Wieprecht
Stellv.: Dr.-Ing. Kristina Terheiden
Versuchsanstalt für Wasserbau
Leiter: Stefan Haun, PhD

Lehrstuhl für Hydromechanik und Hydrosystemmodellierung
Leiter: Prof. Dr.-Ing. Rainer Helmig
Stellv.: apl. Prof. Dr.-Ing. Holger Class

Lehrstuhl für Stochastische Simulation und Sicherheitsforschung für Hydrosysteme
Leiter: Prof. Dr.-Ing. Wolfgang Nowak
Stellv.: apl. Prof. Dr.-Ing. Sergey Oladyshkin
Hydrogeophysik der Vadosen Zone
(mit Forschungszentrum Jülich)
Leiter: Prof. Dr. J.A. Sander Huisman

***VEGAS,* Versuchseinrichtung zur Grundwasser- und Altlastensanierung**
Leiter: Dr.-Ing. Simon Kleinknecht
PD Dr.-Ing. Claus Haslauer

Verzeichnis der Mitteilungshefte

7 *Sonderheft anläßlich des 65. Geburtstages von Prof. Arthur Röhnisch mit Beiträgen von* Benk, Dieter; Breitling, J.; Gurr, Siegfried; Haberhauer, Robert; Honekamp, Hermann; Kuz, Klaus Dieter; Marotz, Günter; Mayer-Vorfelder, Hans-Jörg; Miller, Rudolf; Plate, Erich J.; Radomski, Helge; Schwarz, Helmut; Vollmer, Ernst; Wildenhahn, Eberhard; 1967

8 Jumikis, Alfred: *Beitrag zur experimentellen Untersuchung des Wassernachschubs in einem gefrierenden Boden und die Beurteilung der Ergebnisse*, 1968

9 Marotz, Günter: *Technische Grundlagen einer Wasserspeicherung im natürlichen Untergrund*, 1968

10 Radomski, Helge: *Untersuchungen über den Einfluß der Querschnittsform wellenförmiger Spundwände auf die statischen und rammtechnischen Eigenschaften*, 1968

11 Schwarz, Helmut: *Die Grenztragfähigkeit des Baugrundes bei Einwirkung vertikal gezogener Ankerplatten als zweidimensionales Bruchproblem*, 1969

12 Erbel, Klaus: *Ein Beitrag zur Untersuchung der Metamorphose von Mittelgebirgsschneedecken unter besonderer Berücksichtigung eines Verfahrens zur Bestimmung der thermischen Schneequalität*, 1969

13 Westhaus, Karl-Heinz: *Der Strukturwandel in der Binnenschiffahrt und sein Einfluß auf den Ausbau der Binnenschiffskanäle*, 1969

14 Mayer-Vorfelder, Hans-Jörg: *Ein Beitrag zur Berechnung des Erdwiderstandes unter Ansatz der logarithmischen Spirale als Gleitflächenfunktion*, 1970

15 Schulz, Manfred: *Berechnung des räumlichen Erddruckes auf die Wandung kreiszylindrischer Körper*, 1970

16 Mobasseri, Manoutschehr: *Die Rippenstützmauer. Konstruktion und Grenzen ihrer Standsicherheit*, 1970

17 Benk, Dieter: *Ein Beitrag zum Betrieb und zur Bemessung von Hochwasserrückhaltebecken*, 1970

18 Gàl, Attila: *Bestimmung der mitschwingenden Wassermasse bei überströmten Fischbauchklappen mit kreiszylindrischem Staublech*, 1971, *vergriffen*

19 Kuz, Klaus Dieter: *Ein Beitrag zur Frage des Einsetzens von Kavitationserscheinungen in einer Düsenströmung bei Berücksichtigung der im Wasser gelösten Gase*, 1971, *vergriffen*

20 Schaak, Hartmut: *Verteilleitungen von Wasserkraftanlagen*, 1971

21 *Sonderheft zur Eröffnung der neuen Versuchsanstalt des Instituts für Wasserbau der Universität Stuttgart mit Beiträgen von* Brombach, Hansjörg; Dirksen, Wolfram; Gàl, Attila; Gerlach, Reinhard; Giesecke, Jürgen; Holthoff, Franz-Josef; Kuz, Klaus Dieter; Marotz, Günter; Minor, Hans-Erwin; Petrikat, Kurt; Röhnisch, Arthur; Rueff, Helge; Schwarz, Helmut; Vollmer, Ernst; Wildenhahn, Eberhard; 1972

22 Wang, Chung-su: *Ein Beitrag zur Berechnung der Schwingungen an Kegelstrahlschiebern*, 1972

23 Mayer-Vorfelder, Hans-Jörg: *Erdwiderstandsbeiwerte nach dem Ohde-Variationsverfahren*, 1972

24 Minor, Hans-Erwin: *Beitrag zur Bestimmung der Schwingungsanfachungsfunktionen überströmter Stauklappen*, 1972, *vergriffen*

25 Brombach, Hansjörg: *Untersuchung strömungsmechanischer Elemente (Fluidik) und die Möglichkeit der Anwendung von Wirbelkammerelementen im Wasserbau*, 1972, *vergriffen*

26 Wildenhahn, Eberhard: *Beitrag zur Berechnung von Horizontalfilterbrunnen*, 1972

27 Steinlein, Helmut: *Die Eliminierung der Schwebstoffe aus Flußwasser zum Zweck der unterirdischen Wasserspeicherung, gezeigt am Beispiel der Iller*, 1972

28 Holthoff, Franz Josef: *Die Überwindung großer Hubhöhen in der Binnenschiffahrt durch Schwimmerhebewerke*, 1973

29 Röder, Karl: *Einwirkungen aus Baugrundbewegungen auf trog- und kastenförmige Konstruktionen des Wasser- und Tunnelbaues*, 1973

30 Kretschmer, Heinz: *Die Bemessung von Bogenstaumauern in Abhängigkeit von der Talform*, 1973

31 Honekamp, Hermann: *Beitrag zur Berechnung der Montage von Unterwasserpipelines*, 1973

32 Giesecke, Jürgen: *Die Wirbelkammertriode als neuartiges Steuerorgan im Wasserbau*, und Brombach, Hansjörg: *Entwicklung, Bauformen, Wirkungsweise und Steuereigenschaften von Wirbelkammerverstärkern*, 1974

33 Rueff, Helge: *Untersuchung der schwingungserregenden Kräfte an zwei hintereinander angeordneten Tiefschützen unter besonderer Berücksichtigung von Kavitation*, 1974

34 Röhnisch, Arthur: *Einpreßversuche mit Zementmörtel für Spannbeton - Vergleich der Ergebnisse von Modellversuchen mit Ausführungen in Hüllwellrohren*, 1975

35 *Sonderheft anläßlich des 65. Geburtstages von Prof. Dr.-Ing. Kurt Petrikat mit Beiträgen von*: Brombach, Hansjörg; Erbel, Klaus; Flinspach, Dieter; Fischer jr., Richard; Gàl, Attila; Gerlach, Reinhard; Giesecke, Jürgen; Haberhauer, Robert; Hafner Edzard; Hausenblas, Bernhard; Horlacher, Hans-Burkhard; Hutarew, Andreas; Knoll, Manfred; Krummet, Ralph; Marotz, Günter; Merkle, Theodor; Miller, Christoph; Minor, Hans-Erwin; Neumayer, Hans; Rao, Syamala; Rath, Paul; Rueff, Helge; Ruppert, Jürgen; Schwarz, Wolfgang; Topal-Gökceli, Mehmet; Vollmer, Ernst; Wang, Chung-su; Weber, Hans-Georg; 1975

36 Berger, Jochum: *Beitrag zur Berechnung des Spannungszustandes in rotationssymmetrisch belasteten Kugelschalen veränderlicher Wandstärke unter Gas- und Flüssigkeitsdruck durch Integration schwach singulärer Differentialgleichungen*, 1975

37 Dirksen, Wolfram: *Berechnung instationärer Abflußvorgänge in gestauten Gerinnen mittels Differenzenverfahren und die Anwendung auf Hochwasserrückhaltebecken*, 1976

38 Horlacher, Hans-Burkhard: *Berechnung instationärer Temperatur- und Wärmespannungsfelder in langen mehrschichtigen Hohlzylindern*, 1976

39 Hafner, Edzard: *Untersuchung der hydrodynamischen Kräfte auf Baukörper im Tiefwasserbereich des Meeres*, 1977, ISBN 3-921694-39-6

40 Ruppert, Jürgen: *Über den Axialwirbelkammerverstärker für den Einsatz im Wasserbau*, 1977, ISBN 3-921694-40-X

41 Hutarew, Andreas: *Beitrag zur Beeinflußbarkeit des Sauerstoffgehalts in Fließgewässern an Abstürzen und Wehren*, 1977, ISBN 3-921694-41-8, *vergriffen*

42 Miller, Christoph: *Ein Beitrag zur Bestimmung der schwingungserregenden Kräfte an unterströmten Wehren*, 1977, ISBN 3-921694-42-6

43 Schwarz, Wolfgang: *Druckstoßberechnung unter Berücksichtigung der Radial- und Längsverschiebungen der Rohrwandung*, 1978, ISBN 3-921694-43-4

44 Kinzelbach, Wolfgang: *Numerische Untersuchungen über den optimalen Einsatz variabler Kühlsysteme einer Kraftwerkskette am Beispiel Oberrhein*, 1978, ISBN 3-921694-44-2

45 Barczewski, Baldur: *Neue Meßmethoden für Wasser-Luftgemische und deren Anwendung auf zweiphasige Auftriebsstrahlen*, 1979, ISBN 3-921694-45-0

46 Neumayer, Hans: *Untersuchung der Strömungsvorgänge in radialen Wirbelkammerverstärkern*, 1979, ISBN 3-921694-46-9

47 Elalfy, Youssef-Elhassan: *Untersuchung der Strömungsvorgänge in Wirbelkammerdioden und -drosseln*, 1979, ISBN 3-921694-47-7

48 Brombach, Hansjörg: *Automatisierung der Bewirtschaftung von Wasserspeichern*, 1981, ISBN 3-921694-48-5

49 Geldner, Peter: *Deterministische und stochastische Methoden zur Bestimmung der Selbstdichtung von Gewässern*, 1981, ISBN 3-921694-49-3, *vergriffen*

50 Mehlhorn, Hans: *Temperaturveränderungen im Grundwasser durch Brauchwassereinleitungen*, 1982, ISBN 3-921694-50-7, *vergriffen*

51 Hafner, Edzard: *Rohrleitungen und Behälter im Meer*, 1983, ISBN 3-921694-51-5

52 Rinnert, Bernd: *Hydrodynamische Dispersion in porösen Medien: Einfluß von Dichteunterschieden auf die Vertikalvermischung in horizontaler Strömung*, 1983, ISBN 3-921694-52-3, *vergriffen*

53 Lindner, Wulf: *Steuerung von Grundwasserentnahmen unter Einhaltung ökologischer Kriterien*, 1983, ISBN 3-921694-53-1, *vergriffen*

54 Herr, Michael; Herzer, Jörg; Kinzelbach, Wolfgang; Kobus, Helmut; Rinnert, Bernd: *Methoden zur rechnerischen Erfassung und hydraulischen Sanierung von Grundwasserkontaminationen*, 1983, ISBN 3-921694-54-X

55 Schmitt, Paul: *Wege zur Automatisierung der Niederschlagsermittlung*, 1984, ISBN 3-921694-55-8, *vergriffen*

56 Müller, Peter: *Transport und selektive Sedimentation von Schwebstoffen bei gestautem Abfluß*, 1985, ISBN 3-921694-56-6

57 El-Qawasmeh, Fuad: *Möglichkeiten und Grenzen der Tropfbewässerung unter besonderer Berücksichtigung der Verstopfungsanfälligkeit der Tropfelemente*, 1985, ISBN 3-921694-57-4, *vergriffen*

58 Kirchenbaur, Klaus: *Mikroprozessorgesteuerte Erfassung instationärer Druckfelder am Beispiel seegangsbelasteter Baukörper*, 1985, ISBN 3-921694-58-2

59 Kobus, Helmut (Hrsg.): *Modellierung des großräumigen Wärme- und Schadstofftransports im Grundwasser*, Tätigkeitsbericht 1984/85 (DFG-Forschergruppe an den Universitäten Hohenheim, Karlsruhe und Stuttgart), 1985, ISBN 3-921694-59-0, *vergriffen*

60 Spitz, Karlheinz: *Dispersion in porösen Medien: Einfluß von Inhomogenitäten und Dichteunterschieden*, 1985, ISBN 3-921694-60-4, *vergriffen*

61 Kobus, Helmut: *An Introduction to Air-Water Flows in Hydraulics*, 1985, ISBN 3-921694-61-2

62 Kaleris, Vassilios: *Erfassung des Austausches von Oberflächen- und Grundwasser in horizontalebenen Grundwassermodellen*, 1986, ISBN 3-921694-62-0

63 Herr, Michael: *Grundlagen der hydraulischen Sanierung verunreinigter Porengrundwasserleiter*, 1987, ISBN 3-921694-63-9

64 Marx, Walter: *Berechnung von Temperatur und Spannung in Massenbeton infolge Hydratation*, 1987, ISBN 3-921694-64-7

65 Koschitzky, Hans-Peter: *Dimensionierungskonzept für Sohlbelüfter in Schußrinnen zur Vermeidung von Kavitationsschäden*, 1987, ISBN 3-921694-65-5

66 Kobus, Helmut (Hrsg.): *Modellierung des großräumigen Wärme- und Schadstofftransports im Grundwasser*, Tätigkeitsbericht 1986/87 (DFG-Forschergruppe an den Universitäten Hohenheim, Karlsruhe und Stuttgart) 1987, ISBN 3-921694-66-3

67 Söll, Thomas: *Berechnungsverfahren zur Abschätzung anthropogener Temperaturanomalien im Grundwasser*, 1988, ISBN 3-921694-67-1

68 Dittrich, Andreas; Westrich, Bernd: *Bodenseeufererosion, Bestandsaufnahme und Bewertung*, 1988, ISBN 3-921694-68-X, *vergriffen*

69 Huwe, Bernd; van der Ploeg, Rienk R.: *Modelle zur Simulation des Stickstoffhaushaltes von Standorten mit unterschiedlicher landwirtschaftlicher Nutzung*, 1988, ISBN 3-921694-69-8, *vergriffen*

70 Stephan, Karl: *Integration elliptischer Funktionen*, 1988, ISBN 3-921694-70-1

71 Kobus, Helmut; Zilliox, Lothaire (Hrsg.): *Nitratbelastung des Grundwassers, Auswirkungen der Landwirtschaft auf die Grundwasser- und Rohwasserbeschaffenheit und Maßnahmen zum Schutz des Grundwassers*. Vorträge des deutsch-französischen

Kolloquiums am 6. Oktober 1988, Universitäten Stuttgart und Louis Pasteur Strasbourg (Vorträge in deutsch oder französisch, Kurzfassungen zweisprachig), 1988, ISBN 3-921694-71-X

72 Soyeaux, Renald: *Unterströmung von Stauanlagen auf klüftigem Untergrund unter Berücksichtigung laminarer und turbulenter Fließzustände*,1991, ISBN 3-921694-72-8

73 Kohane, Roberto: *Berechnungsmethoden für Hochwasserabfluß in Fließgewässern mit überströmten Vorländern*, 1991, ISBN 3-921694-73-6

74 Hassinger, Reinhard: *Beitrag zur Hydraulik und Bemessung von Blocksteinrampen in flexibler Bauweise*, 1991, ISBN 3-921694-74-4, *vergriffen*

75 Schäfer, Gerhard: *Einfluß von Schichtenstrukturen und lokalen Einlagerungen auf die Längsdispersion in Porengrundwasserleitern*, 1991, ISBN 3-921694-75-2

76 Giesecke, Jürgen: *Vorträge, Wasserwirtschaft in stark besiedelten Regionen; Umweltforschung mit Schwerpunkt Wasserwirtschaft*, 1991, ISBN 3-921694-76-0

77 Huwe, Bernd: *Deterministische und stochastische Ansätze zur Modellierung des Stickstoffhaushalts landwirtschaftlich genutzter Flächen auf unterschiedlichem Skalenniveau*, 1992, ISBN 3-921694-77-9, *vergriffen*

78 Rommel, Michael: *Verwendung von Kluftdaten zur realitätsnahen Generierung von Kluftnetzen mit anschließender laminar-turbulenter Strömungsberechnung*, 1993, ISBN 3-92 1694-78-7

79 Marschall, Paul: *Die Ermittlung lokaler Stofffrachten im Grundwasser mit Hilfe von Einbohrloch-Meßverfahren*, 1993, ISBN 3-921694-79-5, *vergriffen*

80 Ptak, Thomas: *Stofftransport in heterogenen Porenaquiferen: Felduntersuchungen und stochastische Modellierung*, 1993, ISBN 3-921694-80-9, *vergriffen*

81 Haakh, Frieder: *Transientes Strömungsverhalten in Wirbelkammern,* 1993, ISBN 3-921694-81-7

82 Kobus, Helmut; Cirpka, Olaf; Barczewski, Baldur; Koschitzky, Hans-Peter: *Versuchseinrichtung zur Grundwasser- und Altlastensanierung VEGAS, Konzeption und Programmrahmen*, 1993, ISBN 3-921694-82-5

83 Zang, Weidong: *Optimaler Echtzeit-Betrieb eines Speichers mit aktueller Abflußregenerierung*, 1994, ISBN 3-921694-83-3, *vergriffen*

84 Franke, Hans-Jörg: *Stochastische Modellierung eines flächenhaften Stoffeintrages und Transports in Grundwasser am Beispiel der Pflanzenschutzmittelproblematik*, 1995, ISBN 3-921694-84-1

85 Lang, Ulrich: *Simulation regionaler Strömungs- und Transportvorgänge in Karstaquiferen mit Hilfe des Doppelkontinuum-Ansatzes: Methodenentwicklung und Parameteridenti-fikation*, 1995, ISBN 3-921694-85-X, *vergriffen*

86 Helmig, Rainer: *Einführung in die Numerischen Methoden der Hydromechanik*, 1996, ISBN 3-921694-86-8, *vergriffen*

87 Cirpka, Olaf: *CONTRACT: A Numerical Tool for Contaminant Transport and Chemical Transformations - Theory and Program Documentation* -, 1996, ISBN 3-921694-87-6

88 Haberlandt, Uwe: *Stochastische Synthese und Regionalisierung des Niederschlages für Schmutzfrachtberechnungen*, 1996, ISBN 3-921694-88-4

89 Croisé, Jean: *Extraktion von flüchtigen Chemikalien aus natürlichen Lockergesteinen mittels erzwungener Luftströmung*, 1996, ISBN 3-921694-89-2, *vergriffen*

90 Jorde, Klaus: *Ökologisch begründete, dynamische Mindestwasserregelungen bei Ausleitungskraftwerken*, 1997, ISBN 3-921694-90-6, *vergriffen*

91 Helmig, Rainer: *Gekoppelte Strömungs- und Transportprozesse im Untergrund - Ein Beitrag zur Hydrosystemmodellierung*-, 1998, ISBN 3-921694-91-4, *vergriffen*

92 Emmert, Martin: *Numerische Modellierung nichtisothermer Gas-Wasser Systeme in porösen Medien,* 1997, ISBN 3-921694-92-2

93 Kern, Ulrich: *Transport von Schweb- und Schadstoffen in staugeregelten*

Fließgewässern am Beispiel des Neckars, 1997, ISBN 3-921694-93-0, vergriffen

94 Förster, Georg: *Druckstoßdämpfung durch große Luftblasen in Hochpunkten von Rohrleitungen 1997*, ISBN 3-921694-94-9

95 Cirpka, Olaf: *Numerische Methoden zur Simulation des reaktiven Mehrkomponententransports im Grundwasser*, 1997, ISBN 3-921694-95-7, vergriffen

96 Färber, Arne: *Wärmetransport in der ungesättigten Bodenzone: Entwicklung einer thermischen In-situ-Sanierungstechnologie*, 1997, ISBN 3-921694-96-5

97 Betz, Christoph: *Wasserdampfdestillation von Schadstoffen im porösen Medium: Entwicklung einer thermischen In-situ-Sanierungstechnologie*, 1998, SBN 3-921694-97-3

98 Xu, Yichun: *Numerical Modeling of Suspended Sediment Transport in Rivers*, 1998, ISBN 3-921694-98-1, vergriffen

99 Wüst, Wolfgang: *Geochemische Untersuchungen zur Sanierung CKW-kontaminierter Aquifere mit Fe(0)-Reaktionswänden,* 2000, ISBN 3-933761-02-2

100 Sheta, Hussam: *Simulation von Mehrphasenvorgängen in porösen Medien unter Einbeziehung von Hysterese-Effekten*, 2000, ISBN 3-933761-03-4

101 Ayros, Edwin: *Regionalisierung extremer Abflüsse auf der Grundlage statistischer Verfahren*, 2000, ISBN 3-933761-04-2, vergriffen

102 Huber, Ralf: *Compositional Multiphase Flow and Transport in Heterogeneous Porous Media*, 2000, ISBN 3-933761-05-0

103 Braun, Christopherus: *Ein Upscaling-Verfahren für Mehrphasenströmungen in porösen Medien*, 2000, ISBN 3-933761-06-9

104 Hofmann, Bernd: *Entwicklung eines rechnergestützten Managementsystems zur Beurteilung von Grundwasserschadensfällen*, 2000, ISBN 3-933761-07-7

105 Class, Holger: *Theorie und numerische Modellierung nichtisothermer Mehrphasenprozesse in NAPL-kontaminierten porösen Medien,* 2001, ISBN 3-933761-08-5

106 Schmidt, Reinhard: *Wasserdampf- und Heißluftinjektion zur thermischen Sanierung kontaminierter Standorte*, 2001, ISBN 3-933761-09-3

107 Josef, Reinhold: *Schadstoffextraktion mit hydraulischen Sanierungsverfahren unter Anwendung von grenzflächenaktiven Stoffen*, 2001, ISBN 3-933761-10-7

108 Schneider, Matthias: *Habitat- und Abflussmodellierung für Fließgewässer mit unscharfen Berechnungsansätzen*, 2001, ISBN 3-933761-11-5

109 Rathgeb, Andreas: *Hydrodynamische Bemessungsgrundlagen für Lockerdeckwerke an überströmbaren Erddämmen*, 2001, ISBN 3-933761-12-3

110 Lang, Stefan: *Parallele numerische Simulation instätionärer Probleme mit adaptiven Methoden auf unstrukturierten Gittern*, 2001, ISBN 3-933761-13-1

111 Appt, Jochen; Stumpp Simone: *Die Bodensee-Messkampagne 2001, IWS/CWR Lake Constance Measurement Program 2001*, 2002, ISBN 3-933761-14-X

112 Heimerl, Stephan: *Systematische Beurteilung von Wasserkraftprojekten,* 2002, ISBN 3-933761-15-8, vergriffen

113 Iqbal, Amin: *On the Management and Salinity Control of Drip Irrigation,* 2002, ISBN 3-933761-16-6

114 Silberhorn-Hemminger, Annette: *Modellierung von Kluftaquifersystemen: Geostatistische Analyse und deterministisch-stochastische Kluftgenerierung,* 2002, ISBN 3-933761-17-4

115 Winkler, Angela: *Prozesse des Wärme- und Stofftransports bei der In-situ-Sanierung mit festen Wärmequellen,* 2003, ISBN 3-933761-18-2

116 Marx, Walter: *Wasserkraft, Bewässerung, Umwelt - Planungs- und Bewertungsschwerpunkte der Wasserbewirtschaftung,* 2003, ISBN 3-933761-19-0

117 Hinkelmann, Reinhard: *Efficient Numerical Methods and Information-Processing Techniques in Environment Water,* 2003, ISBN 3-933761-20-4

118 Samaniego-Eguiguren, Luis Eduardo: *Hydrological Consequences of Land Use / Land Cover and Climatic Changes in Mesoscale Catchments*, 2003, ISBN 3-933761-21-2

119 Neunhäuserer, Lina: *Diskretisierungsansätze zur Modellierung von Strömungs- und Transportprozessen in geklüftet-porösen Medien*, 2003, ISBN 3-933761-22-0

120 Paul, Maren: *Simulation of Two-Phase Flow in Heterogeneous Poros Media with Adaptive Methods*, 2003, ISBN 3-933761-23-9

121 Ehret, Uwe: *Rainfall and Flood Nowcasting in Small Catchments using Weather Radar*, 2003, ISBN 3-933761-24-7

122 Haag, Ingo: *Der Sauerstoffhaushalt staugeregelter Flüsse am Beispiel des Neckars - Analysen, Experimente, Simulationen -,* 2003, ISBN 3-933761-25-5

123 Appt, Jochen: *Analysis of Basin-Scale Internal Waves in Upper Lake Constance,* 2003, ISBN 3-933761-26-3

124 Hrsg.: Schrenk, Volker; Batereau, Katrin; Barczewski, Baldur; Weber, Karolin und Koschitzky, Hans-Peter: *Symposium Ressource Fläche und VEGAS - Statuskolloquium 2003, 30. September und 1. Oktober 2003,* 2003, ISBN 3-933761-27-1

125 Omar Khalil Ouda: *Optimisation of Agricultural Water Use: A Decision Support System for the Gaza Strip,* 2003, ISBN 3-933761-28-0

126 Batereau, Katrin: *Sensorbasierte Bodenluftmessung zur Vor-Ort-Erkundung von Schadensherden im Untergrund*, 2004, ISBN 3-933761-29-8

127 Witt, Oliver: *Erosionsstabilität von Gewässersedimenten mit Auswirkung auf den Stofftransport bei Hochwasser am Beispiel ausgewählter Stauhaltungen des Oberrheins*, 2004, ISBN 3-933761-30-1

128 Jakobs, Hartmut: *Simulation nicht-isothermer Gas-Wasser-Prozesse in komplexen Kluft-Matrix-Systemen*, 2004, ISBN 3-933761-31-X

129 Li, Chen-Chien: *Deterministisch-stochastisches Berechnungskonzept zur Beurteilung der Auswirkungen erosiver Hochwasserereignisse in Flussstauhaltungen,* 2004, ISBN 3-933761-32-8

130 Reichenberger, Volker; Helmig, Rainer; Jakobs, Hartmut; Bastian, Peter; Niessner, Jennifer: *Complex Gas-Water Processes in Discrete Fracture-Matrix Systems: Up-scaling, Mass-Conservative Discretization and Efficient Multilevel Solution,* 2004, ISBN 3-933761-33-6

131 Hrsg.: Barczewski, Baldur; Koschitzky, Hans-Peter; Weber, Karolin; Wege, Ralf: *VEGAS - Statuskolloquium 2004,* Tagungsband zur Veranstaltung am 05. Oktober 2004 an der Universität Stuttgart, Campus Stuttgart-Vaihingen, 2004, ISBN 3-933761-34-4

132 Asie, Kemal Jabir: *Finite Volume Models for Multiphase Multicomponent Flow through Porous Media*. 2005, ISBN 3-933761-35-2

133 Jacoub, George: *Development of a 2-D Numerical Module for Particulate Contaminant Transport in Flood Retention Reservoirs and Impounded Rivers,* 2004, ISBN 3-933761-36-0

134 Nowak, Wolfgang: *Geostatistical Methods for the Identification of Flow and Transport Parameters in the Subsurface,* 2005, ISBN 3-933761-37-9

135 Süß, Mia: *Analysis of the influence of structures and boundaries on flow and transport processes in fractured porous media*, 2005, ISBN 3-933761-38-7

136 Jose, Surabhin Chackiath: *Experimental Investigations on Longitudinal Dispersive Mixing in Heterogeneous Aquifers,* 2005, ISBN: 3-933761-39-5

137 Filiz, Fulya: *Linking Large-Scale Meteorological Conditions to Floods in Mesoscale Catchments,* 2005, ISBN 3-933761-40-9

138 Qin, Minghao: *Wirklichkeitsnahe und recheneffiziente Ermittlung von Temperatur und Spannungen bei großen RCC-Staumauern*, 2005, ISBN 3-933761-41-7

139 Kobayashi, Kenichiro: *Optimization Methods for Multiphase Systems in the Subsurface - Application to Methane Migration in Coal Mining Areas*, 2005, ISBN 3-933761-42-5

140 Rahman, Md. Arifur: *Experimental Investigations on Transverse Dispersive Mixing in*

Heterogeneous Porous Media, 2005, ISBN 3-933761-43-3

141 Schrenk, Volker: *Ökobilanzen zur Bewertung von Altlastensanierungsmaßnahmen,* 2005, ISBN 3-933761-44-1

142 Hundecha, Hirpa Yeshewatesfa: *Regionalization of Parameters of a Conceptual Rainfall-Runoff Model*, 2005, ISBN: 3-933761-45-X

143 Wege, Ralf: *Untersuchungs- und Überwachungsmethoden für die Beurteilung natürlicher Selbstreinigungsprozesse im Grundwasser,* 2005, ISBN 3-933761-46-8

144 Breiting, Thomas: *Techniken und Methoden der Hydroinformatik - Modellierung von komplexen Hydrosystemen im Untergrund*, 2006, ISBN 3-933761-47-6

145 Hrsg.: Braun, Jürgen; Koschitzky, Hans-Peter; Müller, Martin: *Ressource Untergrund: 10 Jahre VEGAS: Forschung und Technologieentwicklung zum Schutz von Grundwasser und Boden,* Tagungsband zur Veranstaltung am 28. und 29. September 2005 an der Universität Stuttgart, Campus Stuttgart-Vaihingen, 2005, ISBN 3-933761-48-4

146 Rojanschi, Vlad: *Abflusskonzentration in mesoskaligen Einzugsgebieten unter Berücksichtigung des Sickerraumes,* 2006, ISBN 3-933761-49-2

147 Winkler, Nina Simone: *Optimierung der Steuerung von Hochwasserrückhaltebeckensystemen,* 2006, ISBN 3-933761-50-6

148 Wolf, Jens: *Räumlich differenzierte Modellierung der Grundwasserströmung alluvialer Aquifere für mesoskalige Einzugsgebiete*, 2006, ISBN: 3-933761-51-4

149 Kohler, Beate: *Externe Effekte der Laufwasserkraftnutzung*, 2006, ISBN 3-933761-52-2

150 Hrsg.: Braun, Jürgen; Koschitzky, Hans-Peter; Stuhrmann, Matthias: *VEGAS-Statuskolloquium 2006,* Tagungsband zur Veranstaltung am 28. September 2006 an der Universität Stuttgart, Campus Stuttgart-Vaihingen, 2006, ISBN 3-933761-53-0

151 Niessner, Jennifer: *Multi-Scale Modeling of Multi-Phase - Multi-Component Processes in Heterogeneous Porous Media*, 2006, ISBN 3-933761-54-9

152 Fischer, Markus: *Beanspruchung eingeerdeter Rohrleitungen infolge Austrocknung bindiger Böden,* 2006, ISBN 3-933761-55-7

153 Schneck, Alexander: *Optimierung der Grundwasserbewirtschaftung unter Berücksichtigung der Belange der Wasserversorgung, der Landwirtschaft und des Naturschutzes*, 2006, ISBN 3-933761-56-5

154 Das, Tapash: *The Impact of Spatial Variability of Precipitation on the Predictive Uncertainty of Hydrological Models,* 2006, ISBN 3-33761-57-3

155 Bielinski, Andreas: *Numerical Simulation of CO_2 sequestration in geological formations*, 2007, ISBN 3-933761-58-1

156 Mödinger, Jens: *Entwicklung eines Bewertungs- und Entscheidungsunterstützungssystems für eine nachhaltige regionale Grundwasserbewirtschaftung*, 2006, ISBN 3-933761-60-3

157 Manthey, Sabine: *Two-phase flow processes with dynamic effects in porous media - parameter estimation and simulation,* 2007, ISBN 3-933761-61-1

158 Pozos Estrada, Oscar: *Investigation on the Effects of Entrained Air in Pipelines,* 2007, ISBN 3-933761-62-X

159 Ochs, Steffen Oliver: *Steam injection into saturated porous media – process analysis including experimental and numerical investigations*, 2007, ISBN 3-933761-63-8

160 Marx, Andreas: *Einsatz gekoppelter Modelle und Wetterradar zur Abschätzung von Niederschlagsintensitäten und zur Abflussvorhersage, 2007,* ISBN 3-933761-64-6

161 Hartmann, Gabriele Maria: *Investigation of Evapotranspiration Concepts in Hydrological Modelling for Climate Change Impact Assessment*, 2007, ISBN 3-933761-65-4

162 Kebede Gurmessa, Tesfaye: *Numerical Investigation on Flow and Transport Characteristics to Improve Long-Term Simulation of Reservoir Sedimentation*, 2007, ISBN 3-933761-66-2

163 Trifković, Aleksandar: *Multi-objective and Risk-based Modelling Methodology for Planning, Design and Operation of Water Supply Systems*, 2007, ISBN 3-933761-67-0

164 Götzinger, Jens: *Distributed Conceptual Hydrological Modelling - Simulation of Climate, Land Use Change Impact and Uncertainty Analysis*, 2007, ISBN 3-933761-68-9

165 Hrsg.: Braun, Jürgen; Koschitzky, Hans-Peter; Stuhrmann, Matthias: *VEGAS – Kolloquium 2007,* Tagungsband zur Veranstaltung am 26. September 2007 an der Universität Stuttgart, Campus Stuttgart-Vaihingen, 2007, ISBN 3-933761-69-7

166 Freeman, Beau: *Modernization Criteria Assessment for Water Resources Planning; Klamath Irrigation Project, U.S.*, 2008, ISBN 3-933761-70-0

167 Dreher, Thomas: *Selektive Sedimentation von Feinstschwebstoffen in Wechselwirkung mit wandnahen turbulenten Strömungsbedingungen*, 2008, ISBN 3-933761-71-9

168 Yang, Wei: *Discrete-Continuous Downscaling Model for Generating Daily Precipitation Time Series*, 2008, ISBN 3-933761-72-7

169 Kopecki, Ianina: *Calculational Approach to FST-Hemispheres for Multiparametrical Benthos Habitat Modelling,* 2008*,* ISBN 3-933761-73-5

170 Brommundt, Jürgen: *Stochastische Generierung räumlich zusammenhängender Niederschlagszeitreihen*, 2008, ISBN 3-933761-74-3

171 Papafotiou, *Alexandros: Numerical Investigations of the Role of Hysteresis in Heterogeneous Two-Phase Flow Systems*, 2008, ISBN 3-933761-75-1

172 He, Yi: *Application of a Non-Parametric Classification Scheme to Catchment Hydrology*, 2008, ISBN 978-3-933761-76-7

173 Wagner, Sven: *Water Balance in a Poorly Gauged Basin in West Africa Using Atmospheric Modelling and Remote Sensing Information*, 2008, ISBN 978-3-933761-77-4

174 Hrsg.: Braun, Jürgen; Koschitzky, Hans-Peter; Stuhrmann, Matthias; Schrenk, Volker: *VEGAS-Kolloquium 2008 Ressource Fläche III*, Tagungsband zur Veranstaltung am 01. Oktober 2008 an der Universität Stuttgart, Campus Stuttgart-Vaihingen, 2008, ISBN 978-3-933761-78-1

175 Patil, Sachin: *Regionalization of an Event Based Nash Cascade Model for Flood Predictions in Ungauged Basins*, 2008, ISBN 978-3-933761-79-8

176 Assteerawatt, Anongnart: *Flow and Transport Modelling of Fractured Aquifers based on a Geostatistical Approach,* 2008, ISBN 978-3-933761-80-4

177 Karnahl, Joachim Alexander: *2D numerische Modellierung von multifraktionalem Schwebstoff- und Schadstofftransport in Flüssen*, 2008, ISBN 978-3-933761-81-1

178 Hiester, Uwe: *Technologieentwicklung zur In-situ-Sanierung der ungesättigten Bodenzone mit festen Wärmequellen,* 2009, ISBN 978-3-933761-82-8

179 Laux, Patrick: *Statistical Modeling of Precipitation for Agricultural Planning in the Volta Basin of West Africa,* 2009, ISBN 978-3-933761-83-5

180 Ehsan, Saqib: *Evaluation of Life Safety Risks Related to Severe Flooding,* 2009, ISBN 978-3-933761-84-2

181 Prohaska, Sandra: *Development and Application of a 1D Multi-Strip Fine Sediment Transport Model for Regulated Rivers,* 2009, ISBN 978-3-933761-85-9

182 Kopp, Andreas: *Evaluation of CO_2 Injection Processes in Geological Formations for Site Screening,* 2009, ISBN 978-3-933761-86-6

183 Ebigbo, Anozie: *Modelling of biofilm growth and its influence on CO_2 and water (two-phase) flow in porous media,* 2009, ISBN 978-3-933761-87-3

184 Freiboth, Sandra: *A phenomenological model for the numerical simulation of multiphase multicomponent processes considering structural alterations of porous media*, 2009, ISBN 978-3-933761-88-0

185 Zöllner, Frank: *Implementierung und Anwendung netzfreier Methoden im Konstruktiven Wasserbau und in der Hydromechanik*, 2009, ISBN 978-3-933761-89-7

186 Vasin, Milos: *Influence of the soil structure and property contrast on flow and transport in the unsaturated zone*, 2010, ISBN 978-3-933761-90-3

187 Li, Jing: *Application of Copulas as a New Geostatistical Tool*, 2010, ISBN 978-3-933761-91-0

188 AghaKouchak, Amir: *Simulation of Remotely Sensed Rainfall Fields Using Copulas*, 2010, ISBN 978-3-933761-92-7

189 Thapa, Pawan Kumar: *Physically-based spatially distributed rainfall runoff modelling for soil erosion estimation*, 2010, ISBN 978-3-933761-93-4

190 Wurms, Sven: *Numerische Modellierung der Sedimentationsprozesse in Retentionsanlagen zur Steuerung von Stoffströmen bei extremen Hochwasserabflussereignissen*, 2011, ISBN 978-3-933761-94-1

191 Merkel, Uwe: *Unsicherheitsanalyse hydraulischer Einwirkungen auf Hochwasserschutzdeiche und Steigerung der Leistungsfähigkeit durch adaptive Strömungsmodellierung*, 2011, ISBN 978-3-933761-95-8

192 Fritz, Jochen: *A Decoupled Model for Compositional Non-Isothermal Multiphase Flow in Porous Media and Multiphysics Approaches for Two-Phase Flow*, 2010, ISBN 978-3-933761-96-5

193 Weber, Karolin (Hrsg.): *12. Treffen junger WissenschaftlerInnen an Wasserbauinstituten*, 2010, ISBN 978-3-933761-97-2

194 Bliefernicht, Jan-Geert: *Probability Forecasts of Daily Areal Precipitation for Small River Basins,* 2011, ISBN 978-3-933761-98-9

195 Hrsg.: Koschitzky, Hans-Peter; Braun, Jürgen: *VEGAS-Kolloquium 2010 In-situ-Sanierung - Stand und Entwicklung Nano und ISCO -,* Tagungsband zur Veranstaltung am 07. Oktober 2010 an der Universität Stuttgart, Campus Stuttgart-Vaihingen*,* 2010*,* ISBN 978-3-933761-99-6

196 Gafurov, Abror: *Water Balance Modeling Using Remote Sensing Information - Focus on Central Asia,* 2010, ISBN 978-3-942036-00-9

197 Mackenberg, Sylvia: *Die Quellstärke in der Sickerwasserprognose: Möglichkeiten und Grenzen von Labor- und Freilanduntersuchungen,* 2010, ISBN 978-3-942036-01-6

198 Singh, Shailesh Kumar: *Robust Parameter Estimation in Gauged and Ungauged Basins,* 2010, ISBN 978-3-942036-02-3

199 Doğan, Mehmet Onur: *Coupling of porous media flow with pipe flow,* 2011, ISBN 978-3-942036-03-0

200 Liu, Min: *Study of Topographic Effects on Hydrological Patterns and the Implication on Hydrological Modeling and Data Interpolation,* 2011, ISBN 978-3-942036-04-7

201 Geleta, Habtamu Itefa: *Watershed Sediment Yield Modeling for Data Scarce Areas,* 2011, ISBN 978-3-942036-05-4

202 Franke, Jörg: *Einfluss der Überwachung auf die Versagenswahrscheinlichkeit von Staustufen,* 2011, ISBN 978-3-942036-06-1

203 Bakimchandra, Oinam: *Integrated Fuzzy-GIS approach for assessing regional soil erosion risks,* 2011, ISBN 978-3-942036-07-8

204 Alam, Muhammad Mahboob: *Statistical Downscaling of Extremes of Precipitation in Mesoscale Catchments from Different RCMs and Their Effects on Local Hydrology,* 2011, ISBN 978-3-942036-08-5

205 Hrsg.: Koschitzky, Hans-Peter; Braun, Jürgen: *VEGAS-Kolloquium 2011 Flache Geothermie - Perspektiven und Risiken,* Tagungsband zur Veranstaltung am 06. Oktober 2011 an der Universität Stuttgart, Campus Stuttgart-Vaihingen*,* 2011*,* ISBN 978-3-933761-09-2

206 Haslauer, Claus: *Analysis of Real-World Spatial Dependence of Subsurface Hydraulic Properties Using Copulas with a Focus on Solute Transport Behaviour,* 2011, ISBN 978-3-942036-10-8

207 Dung, Nguyen Viet: *Multi-objective automatic calibration of hydrodynamic models – development of the concept and an application in the Mekong Delta,* 2011, ISBN 978-3-942036-11-5

208 Hung, Nguyen Nghia: *Sediment dynamics in the floodplain of the Mekong Delta, Vietnam,* 2011, ISBN 978-3-942036-12-2

209 Kuhlmann, Anna: *Influence of soil structure and root water uptake on flow in the unsaturated zone,* 2012, ISBN 978-3-942036-13-9

210 Tuhtan, Jeffrey Andrew: *Including the Second Law Inequality in Aquatic Ecodynamics: A Modeling Approach for Alpine Rivers Impacted by Hydropeaking,* 2012, ISBN 978-3-942036-14-6

211 Tolossa, Habtamu: *Sediment Transport Computation Using a Data-Driven Adaptive Neuro-Fuzzy Modelling Approach,* 2012, ISBN 978-3-942036-15-3

212 Tatomir, Alexandru-Bodgan: *From Discrete to Continuum Concepts of Flow in Fractured Porous Media,* 2012, ISBN 978-3-942036-16-0

213 Erbertseder, Karin: *A Multi-Scale Model for Describing Cancer-Therapeutic Transport in the Human Lung,* 2012, ISBN 978-3-942036-17-7

214 Noack, Markus: *Modelling Approach for Interstitial Sediment Dynamics and Reproduction of Gravel Spawning Fish,* 2012, ISBN 978-3-942036-18-4

215 De Boer, Cjestmir Volkert: *Transport of Nano Sized Zero Valent Iron Colloids during Injection into the Subsurface*, 2012, ISBN 978-3-942036-19-1

216 Pfaff, Thomas: *Processing and Analysis of Weather Radar Data for Use in Hydrology*, 2013, ISBN 978-3-942036-20-7

217 Lebrenz, Hans-Henning: *Addressing the Input Uncertainty for Hydrological Modeling by a New Geostatistical Method*, 2013, ISBN 978-3-942036-21-4

218 Darcis, Melanie Yvonne: *Coupling Models of Different Complexity for the Simulation of CO_2 Storage in Deep Saline Aquifers*, 2013, ISBN 978-3-942036-22-1

219 Beck, Ferdinand: *Generation of Spatially Correlated Synthetic Rainfall Time Series in High Temporal Resolution - A Data Driven Approach*, 2013, ISBN 978-3-942036-23-8

220 Guthke, Philipp: *Non-multi-Gaussian spatial structures: Process-driven natural genesis, manifestation, modeling approaches, and influences on dependent processes*, 2013, ISBN 978-3-942036-24-5

221 Walter, Lena: *Uncertainty studies and risk assessment for CO_2 storage in geological formations*, 2013, ISBN 978-3-942036-25-2

222 Wolff, Markus: *Multi-scale modeling of two-phase flow in porous media including capillary pressure effects,* 2013, ISBN 978-3-942036-26-9

223 Mosthaf, Klaus Roland: *Modeling and analysis of coupled porous-medium and free flow with application to evaporation processes,* 2014, ISBN 978-3-942036-27-6

224 Leube, Philipp Christoph: *Methods for Physically-Based Model Reduction in Time: Analysis, Comparison of Methods and Application*, 2013, ISBN 978-3-942036-28-3

225 Rodríguez Fernández, Jhan Ignacio: *High Order Interactions among environmental variables: Diagnostics and initial steps towards modeling*, 2013, ISBN 978-3-942036-29-0

226 Eder, Maria Magdalena: *Climate Sensitivity of a Large Lake*, 2013, ISBN 978-3-942036-30-6

227 Greiner, Philipp: *Alkoholinjektion zur In-situ-Sanierung von CKW Schadensherden in Grundwasserleitern: Charakterisierung der relevanten Prozesse auf unterschiedlichen Skalen*, 2014, ISBN 978-3-942036-31-3

228 Lauser, Andreas: *Theory and Numerical Applications of Compositional Multi-Phase Flow in Porous Media*, 2014, ISBN 978-3-942036-32-0

229 Enzenhöfer, Rainer: *Risk Quantification and Management in Water Production and Supply Systems*, 2014, ISBN 978-3-942036-33-7

230 Faigle, Benjamin: *Adaptive modelling of compositional multi-phase flow with capillary pressure*, 2014, ISBN 978-3-942036-34-4

231 Oladyshkin, Sergey: *Efficient modeling of environmental systems in the face of complexity and uncertainty*, 2014, ISBN 978-3-942036-35-1

232 Sugimoto, Takayuki: *Copula based Stochastic Analysis of Discharge Time Series*, 2014,

ISBN 978-3-942036-36-8

233 Koch, Jonas: *Simulation, Identification and Characterization of Contaminant Source Architectures in the Subsurface*, 2014, ISBN 978-3-942036-37-5

234 Zhang, Jin: *Investigations on Urban River Regulation and Ecological Rehabilitation Measures, Case of Shenzhen in China*, 2014, ISBN 978-3-942036-38-2

235 Siebel, Rüdiger: *Experimentelle Untersuchungen zur hydrodynamischen Belastung und Standsicherheit von Deckwerken an überströmbaren Erddämmen,* 2014, ISBN 978-3-942036-39-9

236 Baber, Katherina: *Coupling free flow and flow in porous media in biological and technical applications: From a simple to a complex interface description,* 2014, ISBN 978-3-942036-40-5

237 Nuske, Klaus Philipp: *Beyond Local Equilibrium — Relaxing local equilibrium assumptions in multiphase flow in porous media,* 2014, ISBN 978-3-942036-41-2

238 Geiges, Andreas: *Efficient concepts for optimal experimental design in nonlinear environmental systems*, 2014, ISBN 978-3-942036-42-9

239 Schwenck, Nicolas: *An XFEM-Based Model for Fluid Flow in Fractured Porous Media*, 2014, ISBN 978-3-942036-43-6

240 Chamorro Chávez, Alejandro: *Stochastic and hydrological modelling for climate change prediction in the Lima region, Peru*, 2015, ISBN 978-3-942036-44-3

241 Yulizar: *Investigation of Changes in Hydro-Meteorological Time Series Using a Depth-Based Approach*, 2015, ISBN 978-3-942036-45-0

242 Kretschmer, Nicole: *Impacts of the existing water allocation scheme on the Limarí watershed – Chile, an integrative approach*, 2015, ISBN 978-3-942036-46-7

243 Kramer, Matthias: *Luftbedarf von Freistrahlturbinen im Gegendruckbetrieb*, 2015, ISBN 978-3-942036-47-4

244 Hommel, Johannes: *Modeling biogeochemical and mass transport processes in the subsurface: Investigation of microbially induced calcite precipitation*, 2016, ISBN 978-3-942036-48-1

245 Germer, Kai: *Wasserinfiltration in die ungesättigte Zone eines makroporösen Hanges und deren Einfluss auf die Hangstabilität*, 2016, ISBN 978-3-942036-49-8

246 Hörning, Sebastian: *Process-oriented modeling of spatial random fields using copulas*, 2016, ISBN 978-3-942036-50-4

247 Jambhekar, Vishal: *Numerical modeling and analysis of evaporative salinization in a coupled free-flow porous-media system,* 2016, ISBN 978-3-942036-51-1

248 Huang, Yingchun: *Study on the spatial and temporal transferability of conceptual hydrological models*, 2016, ISBN 978-3-942036-52-8

249 Kleinknecht, Simon Matthias: *Migration and retention of a heavy NAPL vapor and remediation of the unsaturated zone*, 2016, ISBN 978-3-942036-53-5

250 Kwakye, Stephen Oppong: *Study on the effects of climate change on the hydrology of the West African sub-region*, 2016, ISBN 978-3-942036-54-2

251 Kissinger, Alexander: *Basin-Scale Site Screening and Investigation of Possible Impacts of CO_2 Storage on Subsurface Hydrosystems*, 2016, ISBN 978-3-942036-55-9

252 Müller, Thomas: *Generation of a Realistic Temporal Structure of Synthetic Precipitation Time Series for Sewer Applications*, 2017, ISBN 978-3-942036-56-6

253 Grüninger, Christoph: *Numerical Coupling of Navier-Stokes and Darcy Flow for Soil-Water Evaporation*, 2017, ISBN 978-3-942036-57-3

254 Suroso: *Asymmetric Dependence Based Spatial Copula Models: Empirical Investigations and Consequences on Precipitation Fields*, 2017, ISBN 978-3-942036-58-0

255 Müller, Thomas; Mosthaf, Tobias; Gunzenhauser, Sarah; Seidel, Jochen; Bárdossy, András: *Grundlagenbericht Niederschlags-Simulator (NiedSim3)*, 2017, ISBN 978-3-942036-59-7

256 Mosthaf, Tobias: *New Concepts for Regionalizing Temporal Distributions of Precipitation and for its Application in Spatial Rainfall Simulation,* 2017, ISBN 978-3-942036-60-3

257 Fenrich, Eva Katrin: *Entwicklung eines ökologisch-ökonomischen Vernetzungsmodells für Wasserkraftanlagen und Mehrzweckspeicher,* 2018, ISBN 978-3-942036-61-0

258 Schmidt, Holger: *Microbial stabilization of lotic fine sediments*, 2018, ISBN 978-3-942036-62-7

259 Fetzer, Thomas: *Coupled Free and Porous-Medium Flow Processes Affected by Turbulence and Roughness–Models, Concepts and Analysis*, 2018, ISBN 978-3-942036-63-4

260 Schröder, Hans Christoph: *Large-scale High Head Pico Hydropower Potential Assessment*, 2018, ISBN 978-3-942036-64-1

261 Bode, Felix: *Early-Warning Monitoring Systems for Improved Drinking Water Resource Protection*, 2018, ISBN 978-3-942036-65-8

262 Gebler, Tobias: *Statistische Auswertung von simulierten Talsperrenüberwachungsdaten zur Identifikation von Schadensprozessen an Gewichtsstaumauern*, 2018, ISBN 978-3-942036-66-5

263 Harten, Matthias von: *Analyse des Zuppinger-Wasserrades – Hydraulische Optimierungen unter Berücksichtigung ökologischer Aspekte*, 2018, ISBN 978-3-942036-67-2

264 Yan, Jieru: *Nonlinear estimation of short time precipitation using weather radar and surface observations*, 2018, ISBN 978-3-942036-68-9

265 Beck, Martin: *Conceptual approaches for the analysis of coupled hydraulic and geomechanical processes*, 2019, ISBN 978-3-942036-69-6

266 Haas, Jannik: *Optimal planning of hydropower and energy storage technologies for fully renewable power systems*, 2019, ISBN 978-3-942036-70-2

267 Schneider, Martin: *Nonlinear Finite Volume Schemes for Complex Flow Processes and Challenging Grids*, 2019, ISBN 978-3-942036-71-9

268 Most, Sebastian Christopher: *Analysis and Simulation of Anomalous Transport in Porous Media*, 2019, ISBN 978-3-942036-72-6

269 Buchta, Rocco: *Entwicklung eines Ziel- und Bewertungssystems zur Schaffung nachhaltiger naturnaher Strukturen in großen sandgeprägten Flüssen des norddeutschen Tieflandes*, 2019, ISBN 978-3-942036-73-3

270 Thom, Moritz: *Towards a Better Understanding of the Biostabilization Mechanisms of Sediment Beds*, 2019, ISBN 978-3-942036-74-0

271 Stolz, Daniel: *Die Nullspannungstemperatur in Gewichtsstaumauern unter Berücksichtigung der Festigkeitsentwicklung des Betons*, 2019, ISBN 978-3-942036-75-7

272 Rodriguez Pretelin, Abelardo: *Integrating transient flow conditions into groundwater well protection*, 2020, ISBN: 978-3-942036-76-4

273 Weishaupt, Kilian: *Model Concepts for Coupling Free Flow with Porous Medium Flow at the Pore-Network Scale: From Single-Phase Flow to Compositional Non-Isothermal Two-Phase Flow*, 2020, ISBN: 978-3-942036-77-1

274 Koch, Timo: *Mixed-dimension models for flow and transport processes in porous media with embedded tubular network systems*, 2020, ISBN: 978-3-942036-78-8

275 Gläser, Dennis: *Discrete fracture modeling of multi-phase flow and deformation in fractured poroelastic media*, 2020, ISBN: 978-3-942036-79-5

276 Seitz, Lydia: *Development of new methods to apply a multi-parameter approach – A first step towards the determination of colmation*, 2020, ISBN: 978-3-942036-80-1

277 Ebrahim Bakhshipour, Amin: *Optimizing hybrid decentralized systems for sustainable urban drainage infrastructures planning*, 2021, ISBN: 978-3-942036-81-8

278 Seitz, Gabriele: *Modeling Fixed-Bed Reactors for Thermochemical Heat Storage with the Reaction System CaO/Ca(OH)$_2$*, 2021, ISBN: 978-3-942036-82-5

279 Emmert, Simon: *Developing and Calibrating a Numerical Model for Microbially Enhanced Coal-Bed Methane Production*, 2021, ISBN: 978-3-942036-83-2

280 Heck, Katharina Klara: Modelling and analysis of multicomponent transport at the interface between free- and porous-medium flow - influenced by radiation and roughness, 2021, ISBN: 978-3-942036-84-9

281 Ackermann, Sina: *A multi-scale approach for drop/porous-medium interaction*, 2021, ISBN: 978-3-942036-85-6

282 Beckers, Felix: *Investigations on Functional Relationships between Cohesive Sediment Erosion and Sediment Characteristics*, 2021, ISBN: 978-3-942036-86-3

283 Schlabing, Dirk: *Generating Weather for Climate Impact Assessment on Lakes*, 2021, ISBN: 978-3-942036-87-0

284 Becker, Beatrix: *Efficient multiscale multiphysics models accounting for reversible flow at various subsurface energy storage sites*, 2021, ISBN: 978-3-942036-88-7

285 Reuschen, Sebastian: *Bayesian Inversion and Model Selection of Heterogeneities in Geo-statistical Subsurface Modeling*, 2021, ISBN: 978-3-942036-89-4

286 Michalkowski, Cynthia: *Modeling water transport at the interface between porous GDL and gas distributor of a PEM fuel cell cathode*, 2022, ISBN: 978-3-942036-90-0

287 Koca, Kaan: *Advanced experimental methods for investigating flow-biofilm-sediment interactions*, 2022, ISBN: 978-3-942036-91-7

288 Modiri, Ehsan: *Clustering simultaneous occurrences of extreme floods in the Neckar catchment*, 2022, ISBN: 978-3-942036-92-4

289 Mayar, Mohammad Assem: *High-resolution spatio-temporal measurements of the colmation phenomenon under laboratory conditions*, 2022, ISBN: 978-3-942036-93-1

290 Schäfer Rodrigues Silva, Aline: *Quantifying and Visualizing Model Similarities for Multi-Model Methods*, 2022, ISBN: 978-3-942036-94-8

291 Moreno Leiva, Simón: *Optimal planning of water and renewable energy systems for copper production processes with sector coupling and demand flexibility*, 2022, ISBN 978-3-942036-95-5

292 Schönau, Steffen: *Modellierung von Bodenerosion und Sedimentaustrag bei Hochwasserereignissen am Beispiel des Einzugsgebiets der Rems*, 2022, ISBN 978-3-942036-96-2

293 Glatz, Kumiko: *Upscaling of Nanoparticle Transport in Porous Media,* 2022, ISBN 978-3-942036-97-9

294 Pavía Santolamazza, Daniela: *Event-based flood estimation using a random forest algorithm for the regionalization in small catchments*, 2022, ISBN 978-3-942036-98-6

295 Haun, Stefan: *Advanced Methods for a Sustainable Sediment Management of Reservoirs*, 2022, ISBN 978-3-942036-99-3

296 Herma, Felix: *Data Processing and Model Choice for Flood Prediction*, 2022, ISBN 978-3-910293-00-7

297 Weinhardt, Felix: *Porosity and permeability alterations in processes of biomineralization in porous media - microfluidic investigations and their interpretation*, 2022, ISBN 978-3-910293-01-4

298 Sadid, Najibullah: *Bedload Transport Estimation in Mountainous Intermittent Rivers and Streams*, 2023, ISBN 978-3-910293-02-1

299 Mohammadi, Farid: *A Surrogate-Assisted Bayesian Framework for Uncertainty-Aware Validation Benchmarks*, 2023, ISBN 978-3-910293-03-8

300 Praditia, Timothy: *Physics-informed Neural Networks for Learning Dynamic, Distributed and Uncertain Systems*, 2023, ISBN 978-3-910293-04-5

301 Gyawali, Dhiraj Raj: *Development and parameter estimation of conceptual snow-melt models using MODIS snow-cover distribution*, 2023, ISBN 978-3-910293-05-2

302 Görtz, Jan: *Coupled modeling approach for physico-chemical processes during the deterioration of cement-based structures*, 2023, ISBN 978-3-910293-06-9

303 Veyskarami, Maziar: *Coupled free-flow–porous media flow processes including drop formation*, 2023, ISBN 978-3-910293-07-6

Die Mitteilungshefte ab der Nr. 134 (Jg. 2005) stehen als pdf-Datei über die Homepage des Instituts: www.iws.uni-stuttgart.de zur Verfügung.